NOVA SCHOOL OF SCIENCE & TECHNOLOGY

DEPARTAMENT OF CHEMISTRY

Juliana Esteves Martins

BSc in Chemistry

Novel Protein Conjugates for Targeted Delivery of Cytotoxic Metal Complexes for Cancer Theranostics

MASTER IN BIOORGANIC CHEMISTRY

NOVA University Lisbon

september, 2024

DEPARTAMENT OF CHEMISTRY

Novel Protein Conjugates for Targeted Delivery of Cytotoxic Metal Complexes for Cancer Theranostics

Juliana Esteves Martins

BSc in Chemistry

Adviser: João Domingos Galamba Correia
Coordinator Researcher, Departamento de Engenharia e Ciências Nucleares, Instituto Superior Técnico, Universidade de Lisboa

Co-advisers: Bruno Luís Jesus Pinto de Oliveira
Assistant Researcher, *Center for Nuclear Sciences and Technology, Instituto Superior Técnico, Universidade de Lisboa*

Examination Committee:

Chair: Luísa Maria da Silva Pinto Ferreira,
Associate Professor with Aggregation, Nova School of Science and Technology, NOVA University Lisbon

Rapporteurs: Pedro Miguel Pimenta Góis,
Assistant Professor with Habilitation, Bioorganic Group, Research Institute for Medicines, Faculty of Pharmacy, University of Lisbon

Adviser: João Domingos Galamba Correia
Coordinator Researcher, Departamento de Engenharia e Ciências Nucleares, Instituto Superior Técnico, Universidade de Lisboa

MASTER IN BIOORGANIC CHEMISTRY

NOVA University Lisbon
September, 2024

Novel Protein Conjugates for Targeted Delivery of Cytotoxic Metal Complexes for Cancer Theranostics

ACKNOWLEDGMENTS

A thesis is not built alone, and so I am deeply grateful to all the people who have played an essential role in its realization and who have made this journey so much better.

First, I would like to express my sincere gratitude to my supervisors. To Dr. Bruno Oliveira, for everything he taught me, for his constant availability and support throughout these months, as well as for the opportunities and trust he placed in me to expand my knowledge. To Dr. João Galamba Correia, I would like to thank his valuable advice, teachings and support, which were fundamental to my growth and to the development of this study.

I am deeply grateful for the trust and encouragement to never give up, even when the challenges seemed overwhelming. It was a pleasure to work with you, as well as with all the members of the Center for Nuclear Sciences and technology of Instituto Superior Técnico and the Institute of Molecular Medicine, to whom I owe special thanks for their unconditional support. In particular, I would like to mention Rúben Silva, Dr. Lurdes Gano, Elizabete Correia, Dr. Filipa Mendes, Dr. Célia Fernandes, Catarina Pinto and Ana Raquel Coelho.

I would also like to express my gratitude to João Catarino, Maria Santos, Carolina Azenha, Margarida Carreira and Catarina Silva

To my friends, both those I've had in my heart since Porto, who, even when I was away, never abandoned me and always encouraged me, and those I met in Lisbon, especially Alexandra and Johander, thank you for the conversations and motivational support, for understanding the difficulties and for your patience over these two years.

To Diogo Dias, my housemate, thank you for the constant “torture” and “bullying”, the late-night chats and the support in difficult times, all of which gave me the strength I needed to overcome the obstacles.

Special thanks to my love Miguel for being my pillar of strength during this journey and for being my constant source of motivation. Your words of encouragement and your confidence in me were fundamental in getting me this far.

Last but not least, a big thank you to my family for all their support throughout this thesis, even from miles away. To my parents, for their efforts over the last two years and for always encouraging me to achieve this goal. To my grandparents, who, even though they didn't understand anything about my field, supported me unconditionally. And to my brother, for being there when I needed him most and for helping me even though he didn't know it.

Finally, I would like to thank everyone who, directly or indirectly, contributed to the completion of this work and to my personal and professional growth. Every gesture, word and presence has made these two years an incredible experience. This achievement is also yours.

ABSTRACT

This thesis focused on evaluating novel theranostic agents combining Gold-based cytotoxic complexes with imaging tags attached to targeting biomolecules, such as antibodies or miniproteins, for a theranostic approach. A miniprotein and antibody targeting PD-L1 were conjugated with a maleimide reagent containing a DBCO group. The “alkyne-proteins” reacted with a symmetric Au(I) complex functionalized with two azides. This resulted in the formation of bioconjugates featuring a Gold complex with a terminal N_3, which was explored to conjugate additional vectors such as a radiochelator or fluorophore. Protein conjugation with excess of reagents (5-20 eq.) for 1-2 h at 25 ºC was confirmed by ESI-MS analysis or fluorescence SDS-PAGE.

Cytotoxicity assays with the miniprotein bearing the “clicked-Gold-N_3” complex showed an IC_{50} of 0.35 µM in A20 cells and 0.33 µM in MC38 cells, which is comparable to the activity of the original complex (0.78 µM in A20 and 0.35 µM in MC38).

The “clicked-Gold-N_3” miniprotein was further reacted with BCN-NODAGA, and the resulting bioconjugate radiolabeled with Gallium-67, with high radiochemical purity (95%) using relatively low protein concentration and mild conditions (30 µM, 30 min reaction at 37 °C). Cell studies demonstrated a significant uptake in PD-L1-expressing cells (~10% uptake/mg of protein), with higher uptake observed at 37 °C compared to 25 °C, suggesting an active binding. Blocking experiments with the unmodified protein (10 µM) resulted in a minimal decrease in uptake, which does not strongly support receptor-mediated binding. Biodistribution revealed selective accumulation of the ^{67}Ga-miniprotein in “A20 PD-L1-tumors” (2.71 ± 0.64 Injected Activity/g of tissue, 4h p.i.), with some off-target uptake in organs like liver (29.79 I.A./g), blood (7.49 I.A./g), lungs (4.17 I.A./g), and spleen (5.12 I.A./g).

A similar strategy was employed to conjugate a fluorophore to Atezolizumab. In-gel fluorescence confirmed successful labeling of the antibody. *In vivo* fluorescent imaging showed an increasing tumor accumulation from 1h to 24h post-injection in mice bearing A20 tumors.

Keywords: ADCs, SPDCs, Gold complex, target drug delivery, theranostic

RESUMO

Esta tese centra-se na avaliação de novos agentes teranósticos que combinam complexos citotóxicos à base de ouro com sondas para imagem ligados a biomoléculas alvo, tais como anticorpos ou miniproteínas, para uma abordagem teranóstica.Uma miniproteína e anticorpo específicos para o PD-L1 foram conjugados com um reagente de maleimida que contém um grupo DBCO rígido. As proteínas contendo alcinos reagiram com um complexo de Au(I) simétrico contendo dois grupos azida. Isto resultou na formação de bioconjugados com um complexo de ouro com um grupo N_3 terminal para incorporar vetores adicionais nas proteínas, tais como um agente quelante ou um fluoróforo. A modificação das proteínas após reação com excesso de reagentes (5-20 eq.) durante 1-2h a 25 °C foi confirmada por análise ESI-MS ou SDS-PAGE de fluorescência.

Os ensaios de citotoxicidade com a miniproteína que contém o complexo Gold-N_3 para "click chemistry" mostraram que a proteína apresentava um IC_{50} de 0.35 µM em células A20 e 0.33 µM em células MC38, o que é comparável à atividade do complexo original não conjugado (0.78 µM em A20 e 0.35 µM em MC38).

A miniproteína Gold-N_3 para "click chemistry" reagiu com o agente quelante BCN-NODAGA, e o bioconjugado resultante foi radiomarcado com Gálio-67 com elevada pureza radioquímica (95%) utilizando-se concentrações relativamente baixas da proteína em condições suaves (30 µM, 30 min de reação a 37 °C). Os estudos em células demonstraram uma acumulação significativa nas células que expressam PD-L1 (~10% de absorção/mg de proteína), com valores mais elevados a 37 °C em comparação com 25 °C, sugerindo um mecanismo ativo de ligação. Experiências de bloqueio com proteína não modificada (10 µM) resultaram apenas numa diminuição mínima da captação, o que não apoia o mecanismo de ligação mediado pelo recetor. Os estudos de biodistribuição revelaram uma acumulação seletiva da ^{67}Ga-miniproteína em tumores que expressam PD-L1 (2.71 ± 0.64 Atividade injetada/g de tecido, 4h p.i.), com alguma captação fora do alvo em órgãos como o fígado (29.79 A.I./g), sangue (7.49 A.I./g), pulmões (4.17 A.I./g) e baço (5.12 A.I./g) às 4h p.i..

Foi utilizada uma estratégia semelhante para conjugar um fluoróforo com o Atezolizumab. A SDS-PAGE confirmou a marcação bem-sucedida do anticorpo. A imagiologia de fluorescência *in vivo* mostrou uma acumulação tumoral crescente entre a 1h e as 24h após a injeção em ratinhos inoculados com tumores A20.

Palavras chave: ADCs, PDCs, Complexo de ouro, Entrega direcionada de drogas, Teranóstica

CONTENTS

List of Figures

List of Tables

List of Equations

Acronyms

TACN	1,4,7-Triazacyclononane
NODAGA	1,4,7-Triazacyclononane-1-glutaric acid-4,7-acetic acid
NOTA	1,4,7-Triazacyclononanetriacetic acid
DOTA	1,4,7,10-Tetraazacyclododecane-1,4,7,10-tetraacetic acid
DOTAGA	1,4,7,10-Tetraazacyclododececane,1-(glutaric acid)-4,7,10-triacetic acid
TETA	1,4,8,11-Tetraazacyclotetradecane-1,4,8,11-tetraacetate
BCN-NODAGA	5-[2-[[(1R,8S)-9-bicyclo[6.1.0]non-4-ynyl]methoxycarbonylamino]ethylamino]-2-[4,7-bis(carboxymethyl)-1,4,7-triazonan-1-yl]-5-oxopentanoic acid
ACN	Acetonitrile
AA	Amino acid
ADCs	Antibody Drug Conjugates
ADDC	Antibody-dependent cellular cytotoxicity
Asp	Aspartic acid
Atezo	Atezolizumab
Beva	Bevacizumab
BFCs	Bifunctional chelators
C^2TN	Centro Ciências e Tecnologias Nucleares
CAR-T	Chimeric Antigen Receptor T-cell Therapy
CHO	Chinese hamster ovary
CT	Computed Tomography
CI	Confidence Interval
CuAAC	Copper-Catalyzed Azide-Alkyne Cycloaddition
Cys	Cysteine
DNA	Deoxyribonucleic Acid
DBCO	Dibenzocyclooctyne
DTPA	Diethylentriamine pentaacetic acid
DTT	DL-Dithiothreitol
DDSs	Drug Delivery Systems
DMEM	Dulbecco's Modified Eagle Medium
Eqs	Equivalents
E. coli	Escherichia coli
EDTA	Ethylenediaminetetraacetic acid
EMA	European Medicines Agency
FDG	^{18}F-fluorodeoxyglucose
FBS	Fetal bovine serum

FDA	Food and Drug Administration
Glu	Glutamic acid
HC	Heavy chain
QTOF	High-resolution ESI-Quadrupole Time-of-Flight mass spectrometry
His	Histidine
HSA	Human serum albumin
HCl	Hydrochloric acid
HEPES	4-(2-Hydroxyethyl)-1-piperazineethanesulfonic acid
NHS	Hydroxysuccinimide bases esters
IA	Injected activity
ICP	Inductively Coupled Plasma
IEDDA	Inverse Electron Demand Diels–Alder
iMM	Instituto de Medicina Molecular
IPD	Institute for Protein Design
iTLC-SG	Instant Thin Layer Chromatography with a Silica Gel
NCS	Isothiocyanates
kDa	Kilodalton
LC	Light chain
LC-MS	Liquid Chromatography - Mass Spectrometry
Lysine	Lys
mAbs	Monoclonal antibodies
Mal DBCO	Maleimide-DBCO
Mal PEG DBCO	Maleimide-PEG-DBCO
MRI	Magnetic Resonance Imaging
MeOH	Methanol
Me	Methionine
MWCO	Molecular Weight Cut-Off
NHC	N-heterocyclic carbene
TEMED	N,N,N',N'-Tetramethylethylenediamine
NSCLC	Non-small cell lung cancer
Cys-S$^-$	Nucleophilic Thiolate ion
COTs	Organic cation transporters
PDCs	Peptide Drug Conjugates
PRRT	Peptide Receptor Radionuclide Therapy
PBS	Phosphate-buffered saline
PET	Positron Emission Tomography
PI	Post Injection
PTMs	Post-Translational Modifications

PD-L1	Programmed Cell Death Ligand 1
PD-1	Programmed Cell Death Protein 1
QDa	Quadrupole mass detector
RP-HPLC	Reversed-Phase High-Performance Liquid Chromatography
rpm	Revolutions per minute
RPMI	Roswell Park Memorial Institute
SDS-PAGE	SDS-Polyacrylamide Gel Electrophoresis
SPECT	Single Photon Emission Computed Tomography
SPDCs	Small Protein-Drugs Conjugates
SPAAC	Strain-Promoted Azide-Alkyne Cycloaddition
TFA	Trifluoroacetic acid
TCEP	Tris(2-carboxyethyl) phosphine
Trp	Tryptophan
Tyr	Tyrosine
UV/Vis	Ultraviolet/Visible
VEGF	Vascular Endothelial Growth Factor

Symbols

α	Alpha particles
NH_2	Amine groups
Å	Angstrom
e^-	Auger electrons
β^-	Beta particles (electrons)
C	Carbon
COOH	Carboxylate groups
Da	Dalton
ddH_2O	Deionized distilled water
^{18}F	Fluorine-18
^{67}Ga	Gallium-67
$^{67}GaCl_3$	Gallium-67 chloride
^{68}Ga	Gallium-68
^{68}Ge	Germanium-68
Au	Gold
g	Gram / Centrifugal force
h	Hour
^{111}In	Indium-111
IC_{50}	Inhibitory Concentration 50%
kDa	KiloDalton
keV	Kilo-electron volt
kV	Kilovolt
^{177}Lu	Luthetium
MBq	Megabecquerel
µL	Microliter
µm	Micrometer
µM	Micromolar
mg	Milligram
mL	Milliliter
mM	Millimolar
min	Minute
M	Molar
nm	Nanometer
nM/kg	Nanomolar per kilogram
%	Percent
β^+	Positron

Rf	Retention factor
RT	Room temperature
$C_2H_3NaO_2$	Sodium acetate
^{99m}Tc	Technecium-99
SH	Thiol groups
UV	Ultraviolet
V	Volume
v/v	Volume/Volume
H_2O	Water
^{68}Zn	Zinc-68

1

INTRODUCTION

1.1 Background – from traditional cancer drugs to targeted therapies

Cancer continues to be one of the biggest threats to human health, taking millions of lives every year. The rising cancer prevalence, the shortcomings of existing treatments, and the issue of drug resistance reinforces the need for innovative medicines [1], [2].

Due to the systemic toxicity and non-specific targeting of traditional treatments with chemotherapeutic agents/drugs [3], it is necessary to develop medicines that can target cancer cells specifically while sparing healthy organs [4], [5].

Current developments in targeted therapies focus on the molecular causes of cancer to increase specificity and decrease side effects [6], [7].

Combining cytotoxic agents with biological carriers, such as target-specific proteins, is one appealing strategy for taking advantage of specific receptors overexpressed on cancer cells. Among these strategies, antibody-drug conjugates (ADCs) and peptide-drug conjugates (PDCs) emerge as effective solutions for delivering therapeutic agents directly to tumors [8]. Other promising strategies for targeted therapy are summarized in recent reviews (e.g. Chimeric Antigen Receptor T-Cell Therapy (CAR-T) and gene therapy, among others) [9], [10]. Even with these developments, there is still a critical need for more effective and selective therapies, particularly for hard-to-treat tumors [7].

1.2 Chemical methods for modification of proteins: a brief introduction to bioconjugation

Protein modification is a crucial step in the development of these targeted therapies creating complex bioconjugates [11]. Targeting specific protein sites without changing the protein´s structure, function, or activity is necessary for precise modifications. To prevent destabilization of the protein, this procedure carefully considers the chemo-selectivity of reagents and reactions under mild conditions.

These conditions encompass several factors, including the type of bioconjugation reagent and stoichiometric ratios to prevent protein denaturation and aggregation, temperature, pH, amount of organic solvent used, reaction time, etc.

Optimization of such parameters aims at the preservation of the protein's native structure and function while allowing for the selective modification of specific sites to create complex bioconjugates [12].

Over the years, advancements in protein modification have resulted in the development of a vast array of bioconjugation technologies, providing a comprehensive toolkit for creating almost unlimited protein constructs with either naturally or synthetically modified residues. The chemical incorporation of artificial functionalities, such as radioisotopes, fluorophores, drugs, PEG units, and other active molecules, into peptides and proteins has proven valuable for a wide range of applications. These include *in vivo* and *in vitro* imaging studies, biophysical and biochemical research, as well as therapeutic and diagnostic purposes [12]. For example, PEGylation of proteins significantly enhance their stability by preventing interactions with degrading enzymes, making them promising candidates for drug development [13]. On the other hand, ADCs, designed through the covalent attachment of cytotoxic payloads to antibodies, have demonstrated success in the treatment of various cancers [14]. Additionally, incorporation of biophysical tags on biomolecules for near-infrared imaging, single-photon emission computed tomography (SPECT) and positron emission tomography (PET), have tremendous potential to improve the diagnosis and management of cancer in oncology [15]. Indeed, bioconjugation chemistry has made significant progress by developing effective synthetic methods to introduce post-translational modifications (PTMs) in peptides and proteins at lysine (Lys), cysteine (Cys) and other less commonly targeted amino acid residues (AA). The effectiveness of these modifications relies on the amino acids' natural abundance and reactivity profile, as well as the microenvironment in which they are incorporated.

1.2.1 Approaches for protein modification

In the past decade, numerous protein modification strategies have been developed (**Figure 1**). Some of these approaches explore novel reactions designed to target natural amino acid residues on proteins with high specificity [16]. Others involve the introduction of non-canonical amino acids through genetic engineering to enable chemical modifications [17]. Additionally, synthetic chemistry methods, as for example metal-catalysed reactions, have also been applied to modify biomolecules [18].

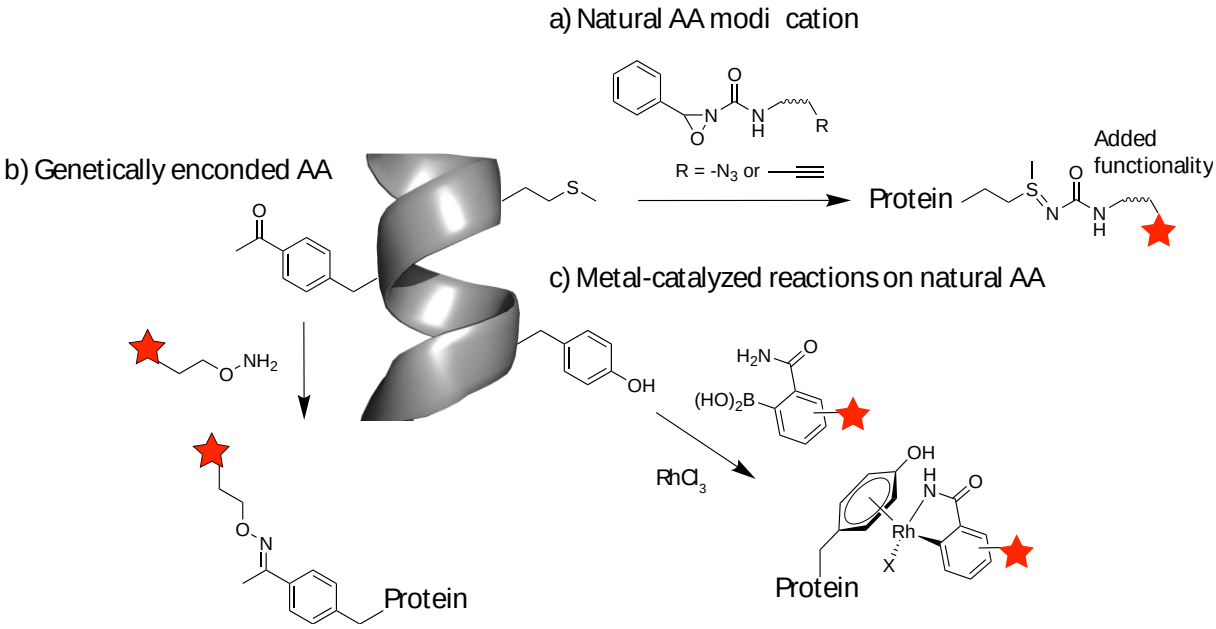

Figure 1 – Representative examples of methods for protein modification

To achieve homogeneous products (i.e. conjugates that are uniform in structure and composition), genetic engineering might be the most reliable approach. However, there is a preference to bypass genetic manipulation due to associated challenges [19] and focus on direct modification of native proteins.

1.2.1.1 Natural amino acid modification

Chemical modification methods have been reported for several of the 20 natural amino acids, including lysine (Lys), cysteine (Cys), tyrosine (Tyr), glutamic acid (Glu), aspartic acid (Asp), tryptophan (Trp), histidine (His), and methionine (Met) [11], [12]. However, Lys and Cys, being the most nucleophilic residues at neutral pH, are the most extensively studied and serve as key targets for protein modification.

Traditionally, hydroxysuccinimide based esters (NHS) were used to modify Lys residues at pH 8 – 9 (**Figure 2a**). However, this AA tends to appear in abundance on proteins which can lead to heterogeneous products when performing uncontrolled bioconjugation. Similarly, Lys residues react quantitatively with isothiocyanates (NCS) forming thioureas (**Figure 2b**). However, the optimal pH for this reaction is between 9 - 9.5, restricting this reagent to non-alkaline sensitive proteins. These reactions have inspired the development and commercialization of many NHS and NCS derivatives for the preparation of fluorescent/radioactive probes and affinity reagents, among others. Aldehyde reagents have been also explored for protein modification via reductive alkylation (**Figure 2c**). While aldehyde-based modifications allow for attachment of various functional molecules on proteins they have a limitation as they also result in heterogeneous products [11]. Recently, Bernardes and colleagues used computational analysis to develop sulfonyl acrylate reagents that can selectively target the most reactive Lys residue in the presence of other nucleophilic amino acids at pH 8.0 (**Figure 2d**). Although this approach results

in the formation of homogeneous constructs it has the limitation that a second reaction is needed for functionalization of the biomolecule of interest [20].

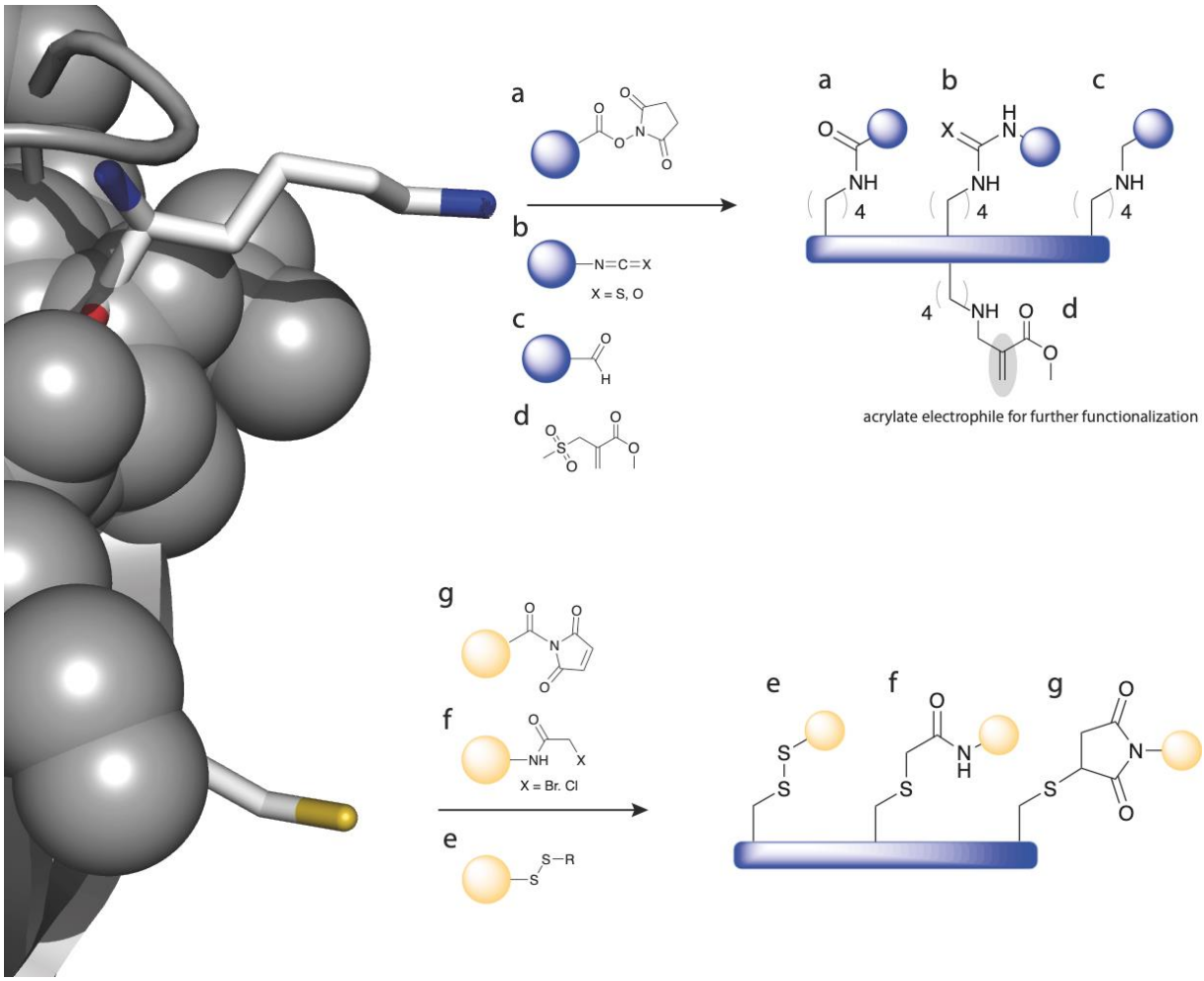

Figure 2 – Classical methods focused on the modification of Cys and Lys side chains. The reactions most commonly used include N-hydroxysuccinimide (NHS)-ester amidation (a), isothiocyanate or isocyanate addition (b), and reductive amination (c) for lysine. Recent methods using sulfonyl acrylates allow the modification of most reactive lysine (d). Methods for cysteine modification include thiol exchange (e), alkylation of α-halocarbonyl electrophiles (f), and maleimide Michael addition (g).

The low natural abundance of free Cys paired with its distinctive nucleophilicity, make this residue very attractive for site-selective protein modification. Under physiological conditions, Cys readily forms a nucleophilic thiolate ion (Cys-S^-) with a general pKa of 8.2. Several strategies for the functionalization of cysteines have been developed and these include disulfide bond formation (**Figure 2e**), alkylating reagents (e.g. α-halocarbonyls; **Figure 2f**) or Michael acceptors (**Figure 2g**) [21].

One factor to consider in bioconjugation reactions with Cys is the use of reducing agents, as Cys can convert between multiple oxidation states and are often naturally present in the oxidized form as disulfide bridges. Some of the most common reducing reagents used are dithiothreitol, β-mercaptoethanol and tris(2-carboxyethyl)phosphine (TCEP). However, caution is required when using TCEP, as

some studies indicate that it may react with certain electrophiles, such as α-halocarbonyls or maleimides, which could interfere with the bioconjugation process [21].

1.2.1.1.1 Cys bioconjugation with Michael acceptors

A reliable method for the selective functionalization of Cys residues is through conjugation with Michael acceptors at neutral pH [21]. Maleimides remain one of the most common α,β-unsaturated carbonyls used to label Cys residues. This reagent reacts quickly and specifically with thiol groups, forming stable thioether bonds with fast kinetics ($k_2 = 10^3 - 10^4\ M^{-1}\ s^{-1}$) under biocompatible conditions. Maleimide reactions do not generate by-products and are typically carried out without the need for catalysts or heating. Moreover, maleimides can be modified via the nitrogen atom to attach a variety of conjugation partners, including chelators, fluorophores, polymer groups, drugs, etc.

Protein conjugation via Cysteine residues has been improved even further by genetic engineering, which makes it possible to build proteins with a single cysteine residue for precise bioconjugation [22].

Despite these developments, one problem associated with maleimide-thiol conjugates is instability due to the reversible bond formation caused by the retro-Michael reaction (**Figure 3**). In thiol-free environments, thiosuccinimide ethers are stable, however in physiological conditions it can occur thiol exchange with GSH or albumin, present in blood plasma.

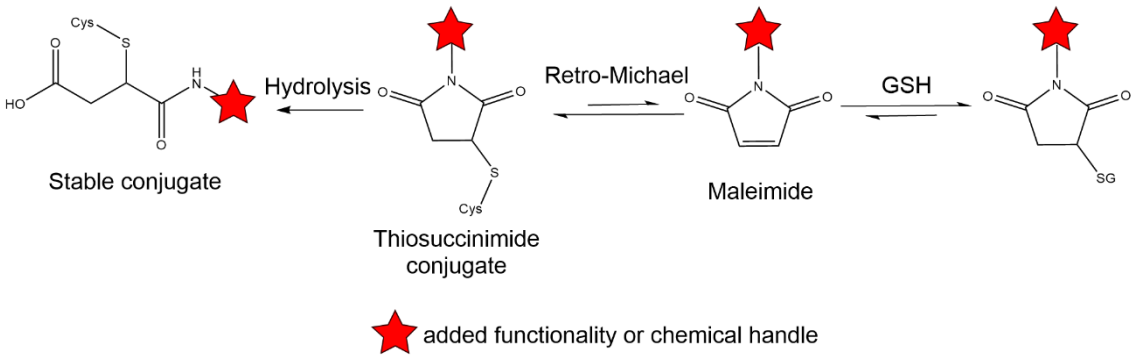

Figure 3 – Michael addition and retro-Michael reactions

To address these challenges, researchers developed the next-generation of maleimides featuring various maleimide-based scaffolds. These strategies focused either on reducing thiol exchange and stabilizing the bioconjugate by promoting thiosuccinimide hydrolysis or on creating alternative chemotypes to achieve more stable bioconjugates.

The stabilization of the thiosuccinimide linkage to avoid bond cleavage and improve stability of the conjugates can be done for example with the modification of the maleimide structure. On this regard, Dimasi and co-workers anticipated that replacing a N-alkyl maleimide substituent with an aromatic ring would increase the imide electrophilicity and, consequently, accelerate thiosuccinimide hydrolysis (**Figure 3**) [23].

Alternatively, a study performed by Genentech reported the influence of protein microenvironment in thiosuccinimide hydrolysis and bioconjugate plasma stability. The study shows that neutrally charged,

buried binding site is prone to retro-Michael thiol exchange from the antibody to thiol-containing nucleophiles. In contrast, a conjugation site with a positive charge can promote rapid thiosuccinimide ring opening, which helps stabilize the conjugate and prevent drug release [24]. Other strategies rely on the intramolecular basic or acid catalysis to promote thiosuccinimide hydrolysis [25]. Nevertheless, antibody-containing therapeutics based on conjugates formed by maleimide-thiol coupling are already commercialized, exemplifying the applicability of this concept. For instance, Brentuximab vedotin and Sacituzumab govitecan, are examples of Food and Drug Administration (FDA) and European Medicines Agency (EMA) approved ADCs whose construction rely on maleimide chemistry [26].

From a pharmacological viewpoint retro-Michael hydrolysis can lead to potential off-target toxicity, decreased therapeutic index and reduced efficacy of the therapies with ADCs. As mentioned, to enhance stability of Cys conjugation, alternative chemotypes to maleimide have been investigated [21], [27]. For example, in 2016, Bernardes and co-workers reported α,β-unsaturated carbonylacrylamide reagents for selective and irreversible cysteine bioconjugation occurring under biocompatible conditions (10 mM, Tris HCl 20 mM, pH 8.0, room temperature, open air) [28]. Recently, Góis and colleagues developed NHS-activated acrylamides for site-selective N-terminal Cysteine functionalization but also for amino-sulfhydryl stapling in peptides and proteins [29], [30]. An additional class of thiol-Michael acceptors are vinylsulfonamides [31].

This introduction is not meant to provide a comprehensive literature review but rather a concise overview of the methodologies currently available for Cys functionalization. Other class of reagents with high chemoselectivity towards in-chain or N-terminal Cys on peptides and proteins have been reported and summarized in literature reviews [21], [27]. These include cyclopropenylketones, chloromethyl acrylates, cyclooctynes, heteroaromatic sulfones, ethynylphosphonamidates, quaternized vinyl- and alkynylpyridine reagents, cyclopropenones, cyanobenzothiazoles, among others. Similarly, recent methods developed for functionalization of other endogenous AAs have been summarized [11], [12].

1.2.1.1.1 Protein modification using bioorthogonal partners

As the area of protein modification evolves, the requirement for highly selective and biocompatible procedures in complex biological environments has prompted the creation of bioorthogonal chemistry [32], [33]. Introduced by Bertozzi and co-workers, the concept of a bioorthogonal reaction referred to reactions that do not interfere with biological processes. These reactions exhibit such high selectivity that they can be performed even in complex biological environments [34], [35]. The principles of bioorthogonal chemistry are closely aligned with those of click chemistry. Click chemistry encompasses a group of highly specific bioorthogonal reactions that "click" two organic compounds together rapidly and with high yield, are easy to perform and purify, and can be carried out in aqueous solvents [36].

Bioorthogonal reactions must meet several strict criteria to ensure high modification efficiency: they must be (1) selective over other potential reactive functional groups present on biomolecules, (2) proceed in aqueous media at (3) near physiological pH, and (4) have fast reaction rates at room temperature (or up to 37°C) using low reactant concentrations. These conditions are crucial to ensuring that the

reactions may efficiently modify proteins while not damaging the complex environment of living systems [32], [37].

In 2002, Sharpless and Meldal independently introduced the copper(I)-catalysed [3+2] azide-alkyne cycloaddition (CuAAC) between an azide and an alkyne (**Figure 4**) [38], [39]. However, the use of copper as a catalyst posed a limitation for protein labelling in living systems, as the concentration required for rapid CuAAC reactions was found to induce cytotoxicity both *in vitro* and *in vivo* [35]. To address this, Bertozzi and colleagues later developed a "copper-free" click reaction, known as strain-promoted [3+2] azide-alkyne cycloaddition (SPAAC) (**Figure 4**) [40]. This copper-free method has lower toxicity risks and operates under physiological circumstances, making it useful for biological applications. Indeed, incorporating SPAAC into protein modification strategies allows researchers to make precise and targeted changes that preserve protein functions while minimizing off-target effects. For example, SPAAC enables the exact labelling or modification of biomolecules found in living organisms, which is essential for developing complex bioconjugates with applications in targeted drug delivery and enhanced imaging, among others [41]. Although SPAAC reactions proceed approximately 100-fold slower compared to CuAAC reactions their reactivity is still suitable for applications in protein modification. For "*in vivo* reactions" the SPAAC handles, in particular the alkyne partner, may have reactivity with biological thiols [42].

In response, Fox and co-workers introduced a new click reaction as an alternative to SPAAC: the inverse electron-demand [4+2] Diels-Alder (IEDDA) cycloaddition between a 1,2,4,5-tetrazine and a strained alkene dienophile [37], [43].

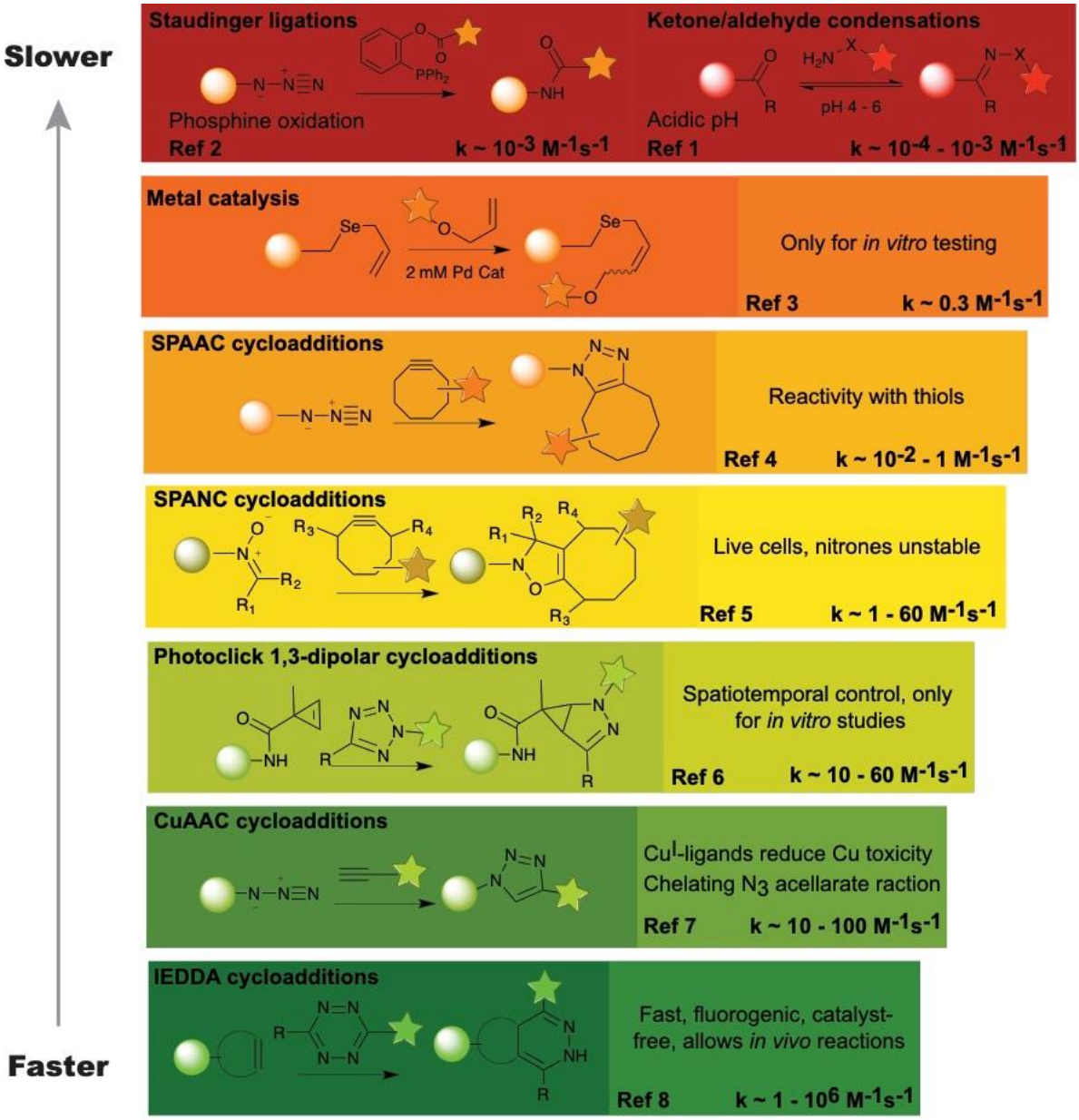

Figure 4 – Examples of bioorthogonal reactions useful for bioconjugation and general comments about their utility and challenges. Adapted from Ref. [37]

1.3 Targeted drug delivery systems

Targeted therapy intends, through the targeting of specific molecules, to block cancer growth and spread [8]. Inspired by the “magic bullet” concept introduced by Paul Ehrlich [44], this approach targets unique genetic mutations and modified proteins that drive cancer cell survival and proliferation. Targeted therapy aims at reducing side effects and enhancing treatment efficacy by selectively attacking cancer cells while sparing normal cells (**Figure 5**).

Drug delivery systems (DDSs) is one of the most successful ways to achieve this selective targeting [45]. These systems are crucial for advancing cancer treatment by ensuring the precise release, timing, and distribution of therapeutic agents within the body. The treatment effectiveness is enhanced by DDSs through the delivery of drugs directly to target cells (**Figure 5 B**). Improvements in drug stability, bioavailability, and concentration at the target site maximize therapeutic outcomes and reduce side effects. Additionally, DDSs extend a drug´s half-life, ensuring prolonged effectiveness while minimizing toxic effects on healthy cells and preventing degradation.

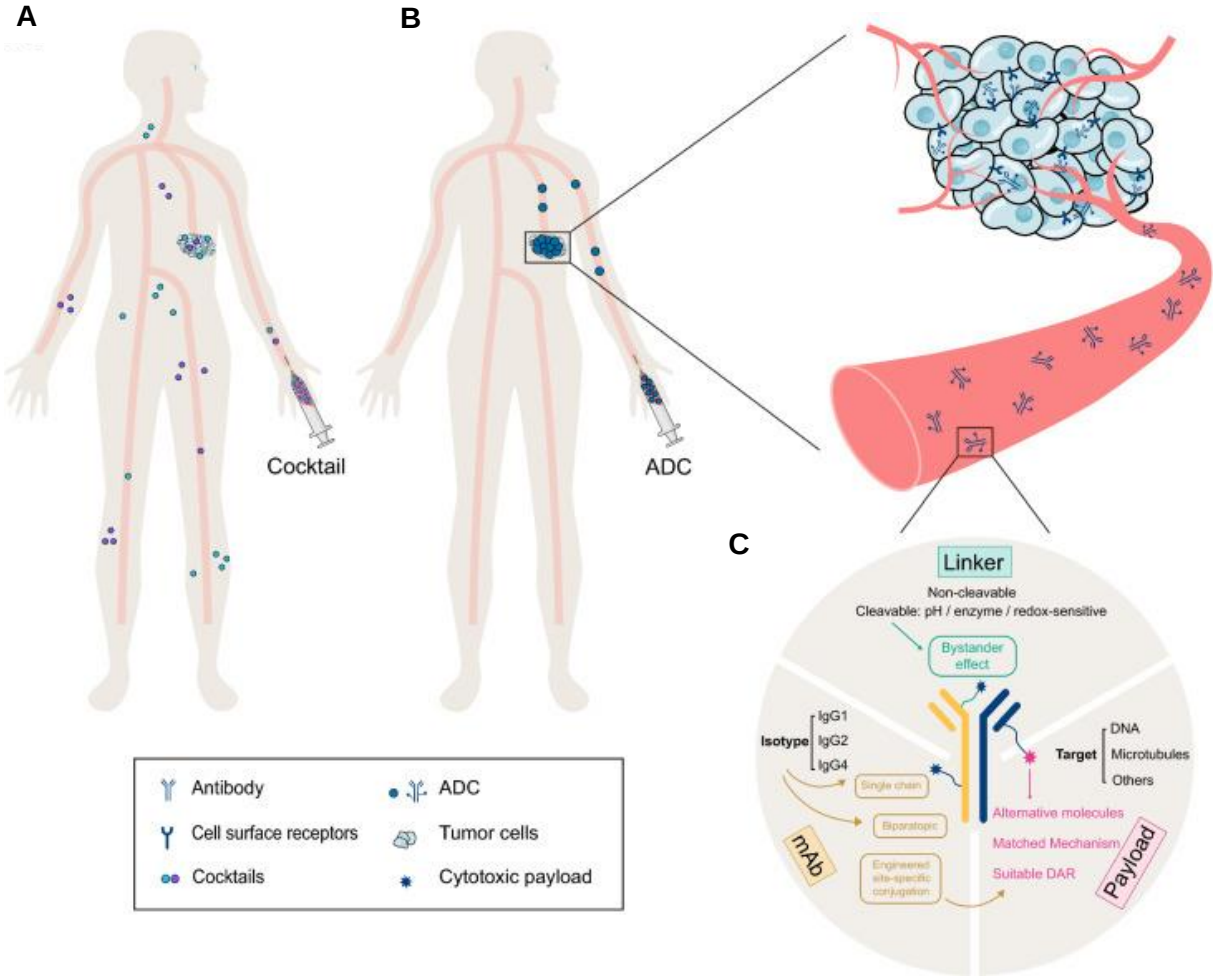

Figure 5 – The difference between conventional (A) and targeted therapy (B). For example, antibody drug conjugate strategy significantly improves antitumoral efficacy. An ADCs exhibit superior tumor targeting in the circulation (B) compared with cocktail therapy (A). Three main components of an ADC include antibody, linker and payload (C). Reprinted from Ref. [46]

However, DDSs face challenges, such as complex drug targets, difficulty in penetrating biological membranes, drug hydrolysis by enzymes, and the acidic tumor environment. Ongoing research is necessary to overcome these challenges and further refine the precision and safety of these systems [47].

ADCs and PDCs have emerged as promising DDSs that address some of these challenges. ADCs consist of a monoclonal antibody linked to a potent cytotoxic drug via a chemical linker (**Figure 5 C**), enabling precise delivery of the drug to cancer cells expressing specific antigens [46]. Similarly, PDCs

use peptides instead of antibodies to deliver drugs directly to cancer cells [48]. Both ADCs and PDCs leverage their targeting components to enhance therapeutic efficacy by ensuring that cytotoxic drugs are delivered specifically to tumors, reducing damage to healthy tissues.

ADCs and PDCs, as well as Small Protein-Drugs Conjugates (SPDC) like Nanobodies-Drug Conjugates, are currently undergoing extensive clinical trials to evaluate their effectiveness and safety across various cancers. ADCs are being evaluated for their good targeting capabilities, especially for blood tumors, while PDCs or SPDCs are being explored for their ability to deliver drugs with greater precision, especially in cases where monoclonal antibodies may face limitations due to their larger size [46], [48]. The smaller molecular size of PDCs/SPDCs may also offer better tumor penetration, making them potentially advantageous for treating solid tumors (**Figure 6**) [46]. Despite their promise, both ADCs and PDCs/SPDCs must overcome challenges to DDSs, such as ensuring stability, preventing premature degradation, and achieving efficient drug release within the tumor environment.

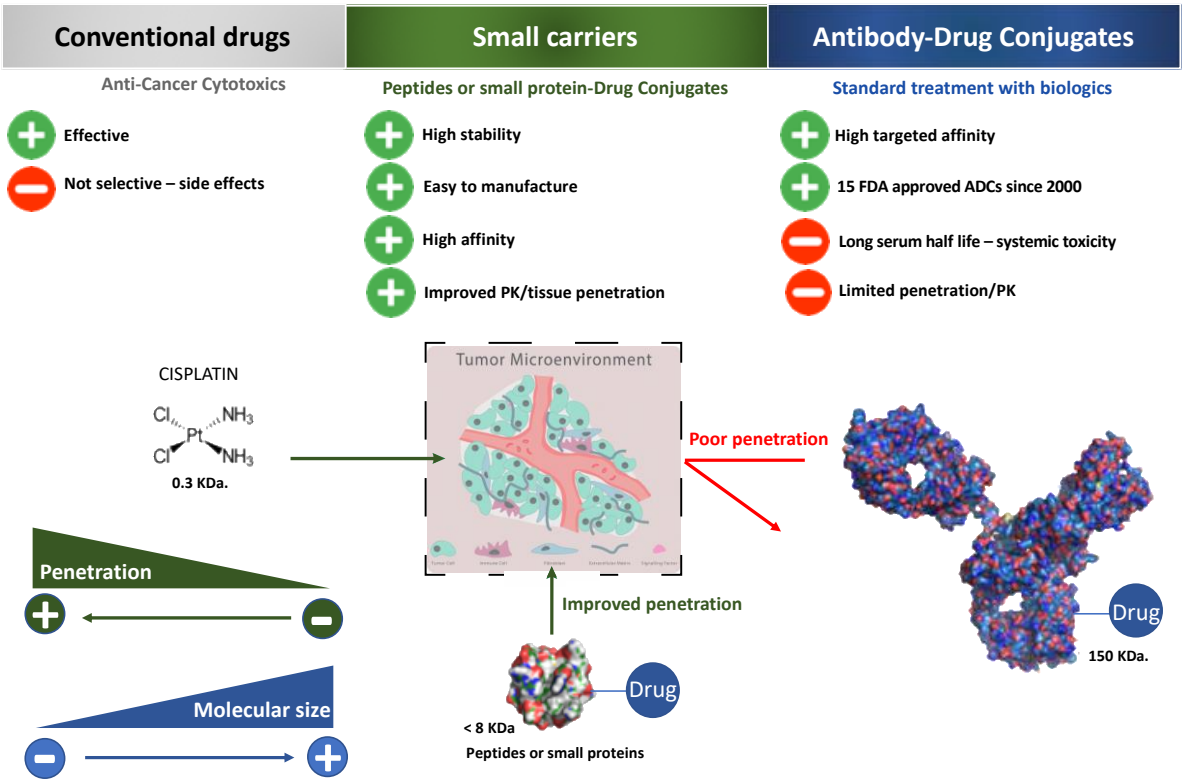

Figure 6 – Strategies for cancer treatment using conventional drugs or targeted therapies. Peptide- or small protein-drug conjugates (PDCs/SPDCs) may also offer better tumor penetration in solid tumors and ADCs excellent targeting properties for blood tumors.

A critical component of ADCs is the chemical linker used to attach the cytotoxic drug to the antibody. Linkers can be classified as either cleavable or non-cleavable, each affecting the mode of action of the ADC. Cleavable linkers release the drug at the tumor site in response to specific physiological triggers, such as high glutathione levels, low pH, or specific proteases (e.g. Cathepsin B) [49], [50]. In contrast,

non-cleavable linkers rely on the degradation of the antibody after internalization within lysosomes or endosomes to release the active drug [49], [50].

The selection of an appropriate linker is crucial, as it must be compatible with the biological environment to ensure efficient drug delivery while minimizing off-target effects. The choice of linker influences the stability, specificity, and potency of the ADC, making it a key factor in therapeutic design.

To date, the FDA has approved 12 ADCs. Seven of these utilize microtubule inhibitor payloads, three use DNA damaging payloads, and two carry payloads that inhibit topoisomerase I, as shown in **Table 1**, along with their respective linkers [51].

Table 1 – Attributes of FDA approved ADCs. From Ref [51]

ADC	Characteristics	FDA-approved indications[a]
Haematological cancers		
Gemtuzumab ozogamicin	Anti-CD33 antibody with an *N*-acetyl calicheamicin payload and a cleavable hydrazone and disulfide linker, conjugated using lysine–amide coupling with an average DAR of 2–3	$CD33^+$ AML (2000, withdrawn 2011, re-approved 2017)
Brentuximab vedotin	Anti-CD30 antibody with an MMAE payload and a cleavable valine–citrulline linker, conjugated using partial cysteine alkylation with an average DAR of 4	Hodgkin lymphoma, systemic ALCL (2011), mycosis fungoides (2017), CD30-expressing lymphomas in combination with chemotherapy (2018), Hodgkin lymphoma in combination with chemotherapy in children (2022)
Inotuzumab ozogamicin	Anti-CD22 antibody with an *N*-acetyl calicheamicin payload and a cleavable hydrazone and disulfide linker, conjugated using lysine–amide coupling with an average DAR of 6	B-ALL (2017)
Polatuzumab vedotin	Anti-CD79b antibody with an MMAE payload and a cleavable valine–citrulline linker conjugated using partial cysteine alkylation with an average DAR of 4	Diffuse large B cell lymphoma (2019)
Belantamab mafodotin	Anti-BCMA antibody with an MMAF payload and a non-cleavable linker conjugated using partial cysteine alkylation with an average DAR of 4	Multiple myeloma (2020, withdrawn 2023)
Loncastuximab tesirine	Anti-CD19 antibody with a PBD dimer payload and a cleavable valine–alanine linker conjugated using partial cysteine alkylation with an average DAR of 2.3	Large B cell lymphoma (2021)
Solid tumours		
Trastuzumab emtansine	Anti-HER2 antibody with a DM1 (maytansine derivative) payload and a non-cleavable linker conjugated using lysine–amide coupling with an average DAR of 3.5	$HER2^+$ breast cancer (2013)
Enfortumab vedotin	Anti-nectin-4 antibody with an MMAE payload and a cleavable valine–alanine linker conjugated using partial cysteine alkylation with an average DAR of 3.8	Urothelial carcinoma (2019), in combination with pembrolizumab (2023)
Trastuzumab deruxtecan	Anti-HER2 antibody with a DXd (exatecan derivative) payload and a cleavable glycine–glycine–phenylalanine–glycine linker conjugated using full homogeneous cysteine alkylation with an average DAR of 7.7	$HER2^+$ breast cancer (2019), $HER2^+$ gastric cancer (2021), $HER2^{low}$ breast cancer (2022)
Sacituzumab govitecan	Anti-TROP2 antibody with an SN-38 payload and a cleavable lysine–PAB and carbonate linker conjugated using full homogeneous cysteine alkylation with an average DAR of 7.6	TNBC (2020), urothelial carcinoma (2021), HR^+, $HER2^-$ breast cancer (2023)
Tisotumab vedotin	Anti-TF antibody with an MMAE payload and a cleavable valine–citrulline linker conjugated using cysteine alkylation (partial) with an average DAR of 4	Cervical cancer (2021)
Mirvetuximab soravtansine	Anti-FRα antibody with a DM4 (maytansine derivative) payload and a cleavable disulfide linker conjugated using lysine–amide coupling with an average DAR of 3.5	$FR\alpha^+$ ovarian, fallopian tube and peritoneal cancers (2022)

ALCL, anaplastic large-cell lymphoma; AML, acute myeloid lymphoma; B-ALL, B cell acute lymphoblastic leukaemia; DAR, drug to antibody ratio; HR, hormone receptor; FRα, folate receptor-α; MMAE, monomethyl auristatin E; MMAF, monomethyl auristatin F; PAB, p-aminobenzyl; PBD, pyrrolobenzodiazepine; TF, tissue factor; TNBC, triple-negative breast cancer.

1.4 The payload for Targeted therapy

For many years, microtubule-targeting and DNA-intercalating agents dominated ADC development. However, the recent approval and clinical success of trastuzumab deruxtecan (Enhertu®) and

sacituzumab govitecan (Trodelvy®), both of which utilize topoisomerase 1 inhibitors as payloads, have demonstrated the potential of conjugating novel payloads with distinct mechanisms of action [52].

Medicinal chemistry has traditionally focused on organic compounds, but recently, inorganic chemistry has gained prominence due to the unique therapeutic potential of metal-based compounds (**Figure 7**) [53].

Metal ions are essential to cellular processes due to their unique chemical properties. They are commonly found in enzyme catalytic sites, where they facilitate crucial biological functions like electron transfer, substrate binding and catalysis. Disruptions in metal ion homeostasis can lead to various health issues, including cancer [54].

Beyond their biological roles, metal ions have become attractive candidates for developing novel therapeutic agents. Although metal-based therapies have historical roots, recent advancements have significantly enhanced our understanding of these compounds and their mechanisms [55].

Metal complexes consist of a metal ion bound to various ligands, forming structures with diverse geometries not easily achieved by organic compounds [56]. Their unique ability to undergo ligand exchange, redox, and catalytic reactions allow for precise targeting of biomolecules. Notably, metal complexes can form stable covalent bonds with biological macromolecules, such as DNA. This targeted action induces apoptosis in cancer cells, making them potent cytotoxic agents [55].

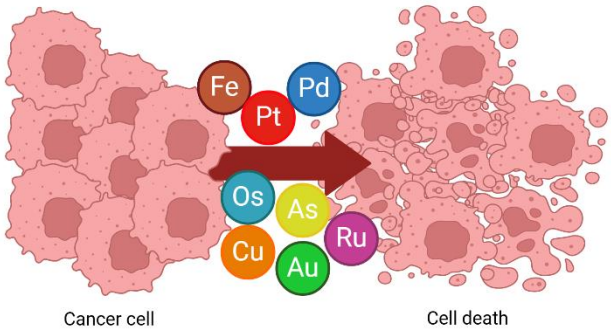

Figure 7 – Representation of cancer cells death by metal complexes. Created with BioRender.com.

1.4.1 Metal complexes in clinical use

Platinum complexes, particularly cisplatin, have significantly advanced the treatment of various cancers, including testicular, ovarian, cervical, head and neck, esophageal, and small-cell lung [57].

However, cisplatin´s non-specificity causes systemic toxicity, leading to serious side effects like nephrotoxicity and neurotoxicity [58]. Long-term use can also damage normal tissues. Additionally, some tumors, like colorectal and non-small lung cancers, are inherently resistant to cisplatin, while others, such as ovarian and small cell lung cancers, can quickly develop resistance [57].

To address these issues, analogues like carboplatin and oxaliplatin have been developed, but they often share similar mechanisms and resistance profiles, limiting their effectiveness [59].

The narrow spectrum of action and resistance in some cancers have driven the design of new metal complexes, including those based on platinum and other transition metals, to improve selectivity and

reduce side effects [60]. Bioinorganic and medicinal chemists are exploring strategies to overcome the limitations of platinum-based therapies. These include targeted drug delivery and designing novel platinum and non-platinum complexes with unique structures and mechanisms to bypass resistance [61].

1.4.2 Metal complexes in development: Gold complexes

The search for more selective, effective, and less toxic metal-based therapies has led researchers to explore various metallic complexes beyond platinum, focusing on their unique structures and mechanisms of action. Recently, ruthenium and gold-based compounds have gained attention due to their promising cytotoxic and potential anticancer properties [62], [63].

Gold, a transition metal, has played a significant role in human history, with medicinal uses dating back to ancient times. For example, China historically used gold as a therapeutic agent. Gold complexes were later found to have antibacterial and antitubercular properties [64].

The discovery of auranofin, a gold complex approved by the FDA for treating rheumatoid arthritis, marked a significant milestone. Recent studies have shown that auranofin also exhibits anticancer activity, inspiring the development of new gold complexes for cancer treatment [63].

A key difference between the antiproliferative activities of platinum and gold complexes lies in their mechanisms of action. While cisplatin interacts directly with DNA to induce apoptosis, gold complexes often inhibit thiol- or seleno-containing enzymes like thioredoxin reductase, which can reduce the side effects and drug resistance commonly associated with platinum-based drugs [65].

However, traditional gold complexes face challenges related to stability, as their ligands can be easily replaced under biological conditions, potentially limiting their effectiveness and specificity. Controlling metal speciation, processes like ligand exchange, hydrolysis, and redox reactions, is crucial to ensure that gold complexes reach their pharmacological targets intact [66].

Gold complexes are not particularly selective against cancer cells and can exhibit significant toxicity in healthy cells. To address these challenges, organometallic complexes, particularly those with N-heterocyclic carbene (NHC) ligands, have been proposed. NHC ligands offer high stability, consistent bioactivity, and ease of modification, making them promising candidates for new anticancer drugs [67], [68], [69].

Published studies have highlighted the significant antiproliferative activity of cationic mono- and binuclear Au(I) bis-NHC complexes, due to the overexpression of organic cation transporters (COTs) in the cell membrane. This selective accumulation in cancer cells underscores the importance of fine-tuning the steric and electronic properties of Au(I)-NHCs [70].

Recent efforts include exploring functional groups such as hydroxyl [71], activated ester [72], azide [73], and carboxylic acid to facilitate bioconjugation [65], thus enhancing the potential of these compounds as targeted anticancer agents [74].

For instance, a highly active azide-functionalized Au(I) bis-1,2,3-triazole-5-ylidene complex was synthesized in collaboration between the Radiopharmaceutical Sciences group of the Centro de Ciências e Tecnologias Nucleares at Instituto Superior Técnico of University of Lisbon and the department of chemistry and catalysis research center at Technical University of Munich (**Figure 8**) [75]. The azide

moiety in the complex was chosen for its bioorthogonality and stability, while a C6 hydrocarbon spacer was included to minimize steric hindrance during bioconjugation with large targeting moieties like peptides or antibodies.

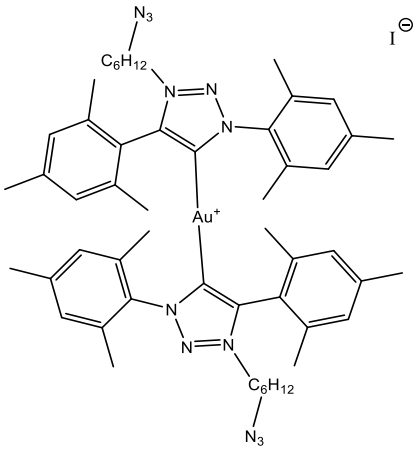

Figure 8 – Structure of Au(I) bis-1,2,3-triazole-5-ylidene complex. Created by ChemDraw.

The study investigates the cytotoxic effects of the Au(I) bis-1,2,3-triazole-5-ylidene complex (**Figure 8**) on human ovarian cancer (A2780) and breast cancer (MCF-7) cell lines, revealing that it surpasses the efficacy of cisplatin and auranofin by several orders of magnitude, as shown in **Table 2**. The IC_{50} values demonstrate significant potency, with 26.6 ± 1.3 nM in A2780 cells and 261 ± 75 nM in MCF-7 cells. When compared to the previously reported non-functionalized Au(I) bis-NHC_{trz} complex, the antiproliferative activity of the complex is higher for A2780 cells, though less active in the MCF-7 cell line. Notably, the high cytotoxic activity is preserved even after modification, which is crucial for enabling subsequent conjugation reactions. The backbone modification of the 1,2,3-triazolium ligand precursor featuring a terminal azide moiety provides a novel framework for further post-functionalization. This facilitates the use of common conjugation protocols, such as CuAAC and SPAAC reactions, allowing the incorporation of various targeting vectors (e.g., peptides, modified antibodies) and clickable radiochelators (e.g., NODAGA or DOTA derivatives) paving the way for the development of highly selective theranostic Au(I) complexes, with the potential for improved cancer treatment outcomes [75].

Table 2 – IC_{50} values ± SD (nM) for the tested compound at 48 h incubation in ovarian cancer (A2780) and breast cancer (MCF-7) cell lines. The values are given in nanomolar concentrations. Adapted from Ref. [75]

	A2780	**MCF-7**
Cisplatin	3600 ± 1300	21000 ± 6300
Auranofin	430 ± 230	280 ± 140
Au(I) bis NHC_{trz}	360 ± 90	84 ± 16
Au(I) bis-1,2,3-triazole-5-ylidene	26.6 ± 1.3	261 ± 75

Researchers are also exploring innovative delivery systems to enhance the targeting and bioavailability of these gold complexes. By using targeting vehicles such as antibodies, the goal is to create more selective chemotherapeutic treatments that minimize damage to healthy tissues.

1.5 Conjugation strategies for the preparation of protein-based gold complexes

Binding the chemical linker to the protein is an essential step in creating ADCs or PDCs. As previously discussed, thiol groups (-SH), due to their reactivity, are frequently used for conjugation. Since at biological conditions cysteine residues in proteins are often present in the form disulfide bridges, the use of agents like TCEP or DL-dithiothreitol (DTT) is key to reduce the disulfide bridge under controlled conditions to generate free thiol groups (**Figure 9**). In this way, the disulphide bridges on antibodies, linking the heavy and light chains, are explored as binding sites for conjugation with sulfhydryl-reactive linkers creating a strong, stable bond, that connects the antibody to the linker (**Figure 9**) [76].

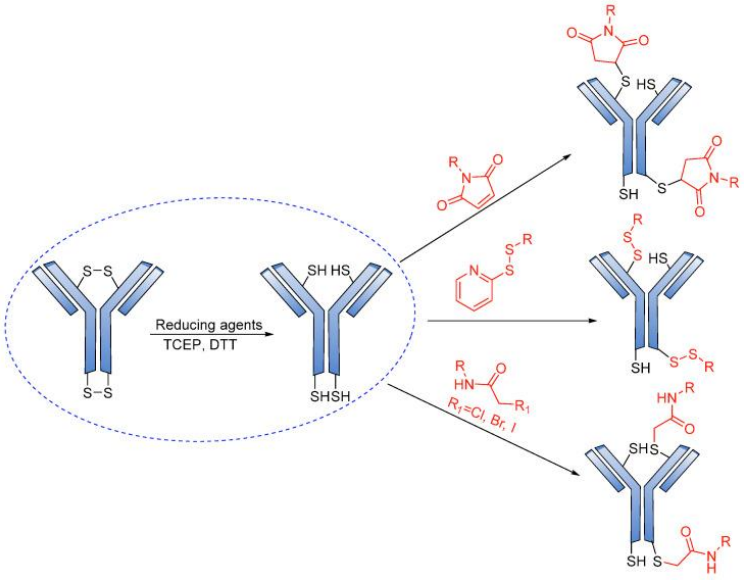

Figure 9 – Mechanism for the formation of the sulfyhydryl attachment site. From Ref. [76]

While the bioconjugation of organic drugs to protein-based carriers is emerging as a promising strategy to enhance the pharmacological properties of anticancer drugs, the use of ADCs with metal-based cytotoxic payloads is still relatively rare. A notable example involves the conjugation of gold(I) compounds to antibodies for targeted delivery. Gold has a strong affinity for cysteine residues in serum proteins like human serum albumin (HSA), which can sometimes lead to drug deactivation. However, by conjugating gold compounds to antibodies that specifically target cancer cells, it is possible to enhance efficacy and minimize side effects. A pioneering example is an ADC involving a N-heterocyclic carbene gold fragment conjugated to an engineered Trastuzumab antibody, Thiomab, recently reported by Bernardes et al (**Figure 10**) [77].

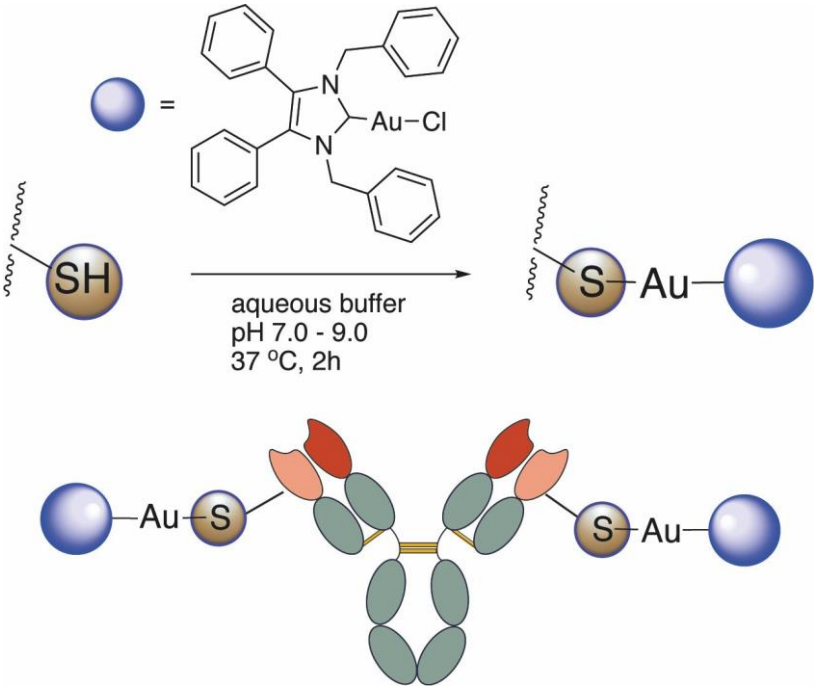

Figure 10 – Au(I) complexes conjugated to an antibody for enhanced selectivity towards cancer cells. From Ref. [77]

Ahad and Contel et al. conjugated an Au(I) phosphine complex to Trastuzumab with an additional linker at the lysine or cysteine side chains (**Figure 11**). These conjugates showed high efficacy against HER2-positive breast cancer mouse model [78].

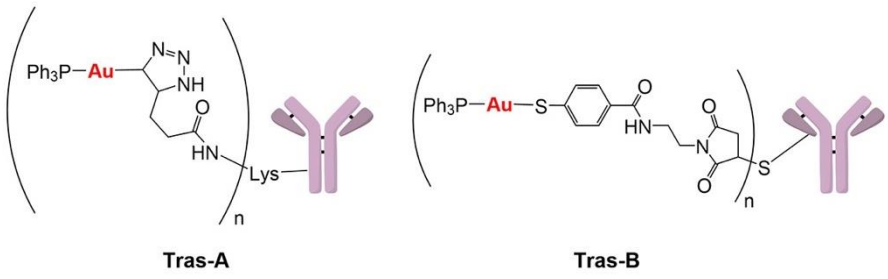

Figure 11 – Gold-containing ADCs studied by Ahad and Contel et al. From Ref. [78]

Although proteins incorporating gold complexes have not yet advanced to clinical trials, they hold promise due to the potential benefits of combining the unique properties of gold complexes with the enhanced tumor delivery of proteins. Additionally, gold nanoparticles have been shown to stabilize peptide-drug-conjugates, facilitating sustained targeted drug delivery to cancer cells [79]. Therefore, peptide and protein conjugates could represent a promising new avenue for the specific delivery of the cytotoxic gold complexes to cancer cells.

1.6 Nuclear Medicine in therapy and diagnosis

Nuclear medicine is a specialized area of medicine that uses radioactive substances, called radiopharmaceuticals, to diagnose and treat diseases. Generally, each radiopharmaceutical contains two key components, a radioactive part (radionuclide) and a carrier substance (pharmaceutical). The pharmaceutical component directs the isotope to specific organs or areas in the body, where it either targets a disease or participates in natural physiological processes. The radionuclide emits radiation that can be detected by imaging devices [80].

Traditional imaging techniques, such as Computed Tomography (CT) and Magnetic Resonance Imaging (MRI), primarily focus on providing detailed images of the body's structure and anatomy. These methods are excellent for detecting physical abnormalities but offer limited insight into the biological or molecular characteristics of the tissue [81].

In contrast, nuclear imaging techniques, such as SPECT, and PET, provide a deeper understanding by visualizing the molecular processes within the body. These techniques focus on the biological activity of tissues, such as tumor metabolic processes. For example, the elevated glucose metabolism in most types of malignancy is responsible for ^{18}F-fluorodeoxyglucose (FDG) accumulation into cancer cells [82]. Indeed, a FDG PET scan is one of the most powerful tools currently available to detect and monitor disease. This molecular imaging approach offers significant advantages for diagnosing and treating diseases, particularly cancers, by revealing detailed information about disease behaviour and helping to tailor more effective treatments [15].

1.7 Radioisotopes used in nuclear medicine

Nuclear medicine creates diagnostic images using various forms of radiation emitted by radioactive decay of radionuclides. Diagnostic radiotracers emit or indirectly create photons that are detected, allowing them to view drug distribution throughout the body. PET imaging uses positron-emitting radionuclides (β+), while gamma-emitters are for SPECT imaging (**Figure 12**) [83].

When positrons interact with neighbouring electrons (β-), they undergo "annihilation", leading in the generation of two gamma rays that travel in opposite directions. A PET scanner detects these gamma rays and creates an image from them. In SPECT, each decay produces a photon with enough energy to be detected outside the body with a gamma camera or SPECT scanner (**Figure 12**) [83].

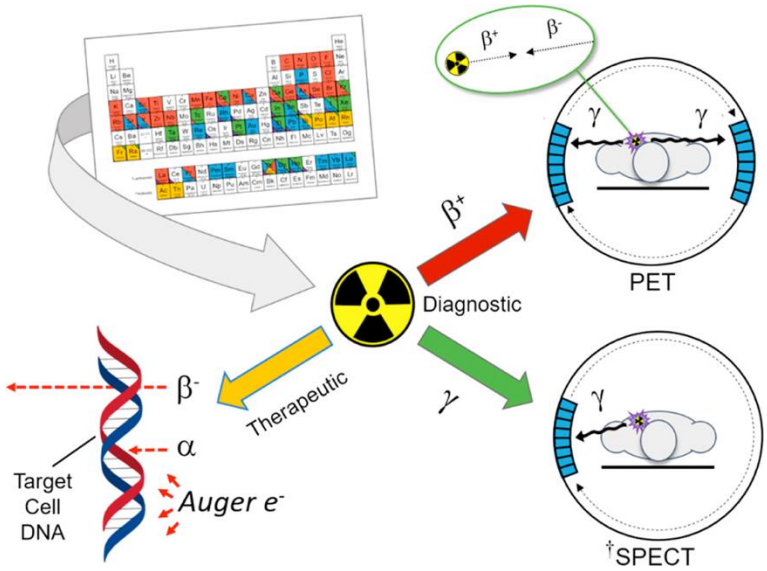

Figure 12 – Radiometal decay types and their corresponding application in nuclear medicine. From Ref. [84]

The radionuclides used to make a radiotracer are chosen based on availability, the energy of the emitted particles or radiation, physical half-life, intended application, and cost. PET provides greater resolution and sensitivity, whereas SPECT benefits from longer-lived radioisotopes that are more readily available and less expensive. Most radionuclides utilized in SPECT are metallic isotopes like ^{99m}Tc, ^{67}Ga and ^{111}In (**Table 3**).

Table 3 – Isotopes with clinical use or potential for application in image. Adapted from Ref.[85]

PET Imaging				SPECT Imaging			
Nuclide	**Half-life/min**	**Type of emission**	**Max. Energy/MeV**	**Nuclide**	**Half-life/h**	**Type of emission**	**Principal photon emission energies/MeV**
^{11}C	20.3	β^+	0.97	^{123}I	13.2	Electron capture	0.16
^{13}N	10	β^+	1.20	^{99m}Tc	6	Isomeric transition	0.14
^{15}O	2	β^+	1.74	^{111}In	67.9	Electron capture	0.17/0.25
^{18}F	110	β^+	0.64	^{67}Ga	78.3	Electron capture	0.09/0.19/0.30
^{64}Cu	762	β^+/electron capture	0.66	^{20}Tl	73.1	Electron capture	0.17
^{68}Ga	68.1	β^+/electron capture	1.90				
^{76}Br	972	β^+/electron capture	4.00				
^{124}I	60192	β^+/electron capture	2.14				

For therapeutic applications, ionizing radiation is employed to destroy tumor tissue through the emission of subatomic particles (**Figure 12**). Different particles, including alpha particles (α), beta particles (β^-), and Auger electrons (e^-), have varying ranges within cells based on their charge, mass, and energy. β^- have a longer range within cells, making them suitable for treating larger tumor masses. α and e^- are effective for targeting small clusters of tumor cells. α particles have a short range but high energy, while e^- are advantageous due to their high cytotoxicity and short-range biological efficacy. When the radiopharmaceutical is designed to position the radionuclide close to its therapeutic target, such as the nucleus of pathological cells, specifically the DNA strands, e^- can provide highly localized and effective treatment [83], [86].

1.8 General considerations about radiopharmaceuticals

As previously mentioned, nuclear medicine utilizes radiopharmaceuticals for both therapy and diagnosis. Radiopharmaceuticals are compounds that contain a radionuclide and are designed to deliver radioactivity to specific organs or tissues within the patient. Diagnostic radiopharmaceuticals can be categorized into two main types: perfusion and specific [84].

Perfusion radiopharmaceuticals are carried by the bloodstream to the target organ in proportion to the blood flow. They do not bind to specific sites and are distributed based on their size and charge [84].

[^{99m}Tc]Tc-Tetrofosmin is a commonly used perfusion radiopharmaceutical for myocardial perfusion imaging. It accumulates in healthy myocardial tissue in direct relation to blood flow, allowing clinicians to evaluate areas of reduced perfusion and aiding in the diagnosis of coronary artery disease. [^{99m}Tc]Tc-Tetrofosmin is favored for its rapid blood clearance, stable imaging properties, and optimal characteristics such as a short half-life, which help minimize patient radiation exposure while delivering high-quality diagnostic results. [^{99m}Tc]Tc-Tetrofosmin are passively distributed based on blood flow, making them particularly useful for evaluating overall myocardial perfusion [87].

In contrast, specific radiopharmaceuticals are guided by biologically active molecules, such as antibodies or peptides, which recognize and bind to a particular molecular target, such as receptors or enzymes (targeting vector) (**Figure 13**). The ability of these biomolecules to recognize and bind to their target determines the radiopharmaceutical's localization in the desired tissue, and this targeting capability must remain intact after the radionuclide is incorporated [84].

An example of such a specific radiopharmaceutical is Lutathera® ([^{177}Lu]Lu-DOTA-TATE), which is approved for peptide receptor radionuclide therapy (PRRT). Lutathera® targets somatostatin receptors, which are overexpressed in certain types of neuroendocrine tumors. By binding to these receptors, Lutathera® delivers targeted radiation directly to the tumor cells, minimizing damage to surrounding healthy tissue. Its approval by both the FDA and European Medicines Agency (EMA) represents a significant advancement in targeted cancer therapy, particularly for patients with inoperable or metastatic neuroendocrine tumors [88].

While most radiopharmaceuticals currently used in clinical practice are perfusion-based, the focus of ongoing research in radiopharmaceutical chemistry is increasingly on the development of specific radiopharmaceuticals [89].

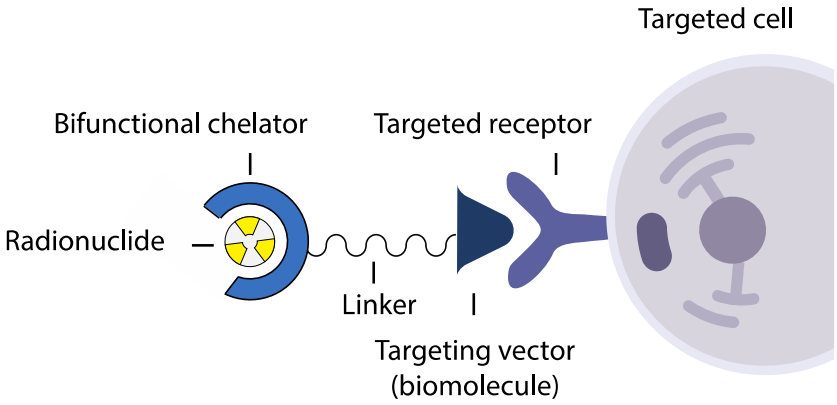

Figure 13 – Representation of the composition of a specific radiopharmaceutical. Created with BioRender.com

1.8.1 Bifunctional ligands to conjugation of radioisotopes to biomolecules

To produce specific radiopharmaceuticals using metal complexes, it is essential to link the biological and radioactive components with bifunctional chelators (BFCs) (**Figure 13**). The BFC has both a metal-binding moiety (i.e. the chelator) to strongly coordinate a radioactive metal ion and a chemically reactive functional group suitable for the covalent attachment of a targeting vector (**Figure 13**) [89], [90]. The primary goal of radiometal complexation is to create stable coordination complexes, which prevent the release of free metals *in vivo*. Achieving this stability requires selecting a chelator that is well-matched to the specific metal [89], [90]. Linkers are often used to separate the chelator from the bioconjugate, ensuring that the biological properties of the biomolecule remain intact. The properties of these linkers are crucial, as adding side groups can be a powerful strategy to optimize radiotracer´s pharmacokinetics and biodistribution [89], [90].

1.8.2 Chelator agent in a bifunctional ligand

Due to the diversity of metallic radionuclides, no single BFC can effectively chelate all radiometals. Therefore, various BFCs are employed based on the specific radionuclide chosen. The size, charge, oxidation state and electron configuration of the radiometals dictate the coordination number required of a BFC. A widespread practice in labeling biomolecules with metals involves the use of appropriate chelating agents that enable the formation of stable complexes. This is crucial because the undesired release of the radioisotope can lead to its binding with serum proteins, such as transferrin, or its accumulation in non-target, radiosensitive organs like bones, bone marrow, or kidneys [91].

Early chelating agents in nuclear medicine, such as diethylentriamine pentaacetic acid (DTPA) and ethylenediaminetetraacetic acid (EDTA), were open-chain agents that proved instable, often leading to radionuclide dissociation, and diminishing their clinical potential. Preventing this dissociation is vital to reduce the accumulation of radioactive material in the bloodstream and enhanced uptake at the tumor site [91].

To overcome these issues, more stable chelating agents have been developed, particularly macrocyclic chelators such as 1,4,7-triazacyclononanetriacetic acid (NOTA), 1,4,7,10-tetraazacyclododecane-1,4,7,10-tetraacetic acid (DOTA) and 1,4,8,11-tetraazacyclotetradecane-1,4,8,11-tetraacetate (TETA) (**Figure 14**). These macrocyclic structures provide high thermodynamic stability to metal complexes, improving their performance in clinical applications [84], [91]. NOTA, for instance, has three carboxylic acid groups that can be used for conjugation to the targeting moiety. However, sacrificing a carboxylate donor may reduce complex stability and modify the overall charge, which is not ideal. To address this, glutaric acid can be used as a pendant arm on the 1,4,7-triazacyclononane (TACN) instead of acetic acid, forming the 1,4,7-triazacyclononane-1-glutaric acid-4,7-acetic acid (NODAGA) chelator. NODAGA can be conjugated to a biomolecule without sacrificing the preferred donor atom set, thanks to the additional functional group on the pendant arm, which also increases the flexibility of the linker. 1,4,7,10-Tetraazacyclododececane,1-(glutaric acid)-4,7,10-triacetic acid (DOTAGA) is an analogous of NODAGA (**Figure 14**) [84], [91].

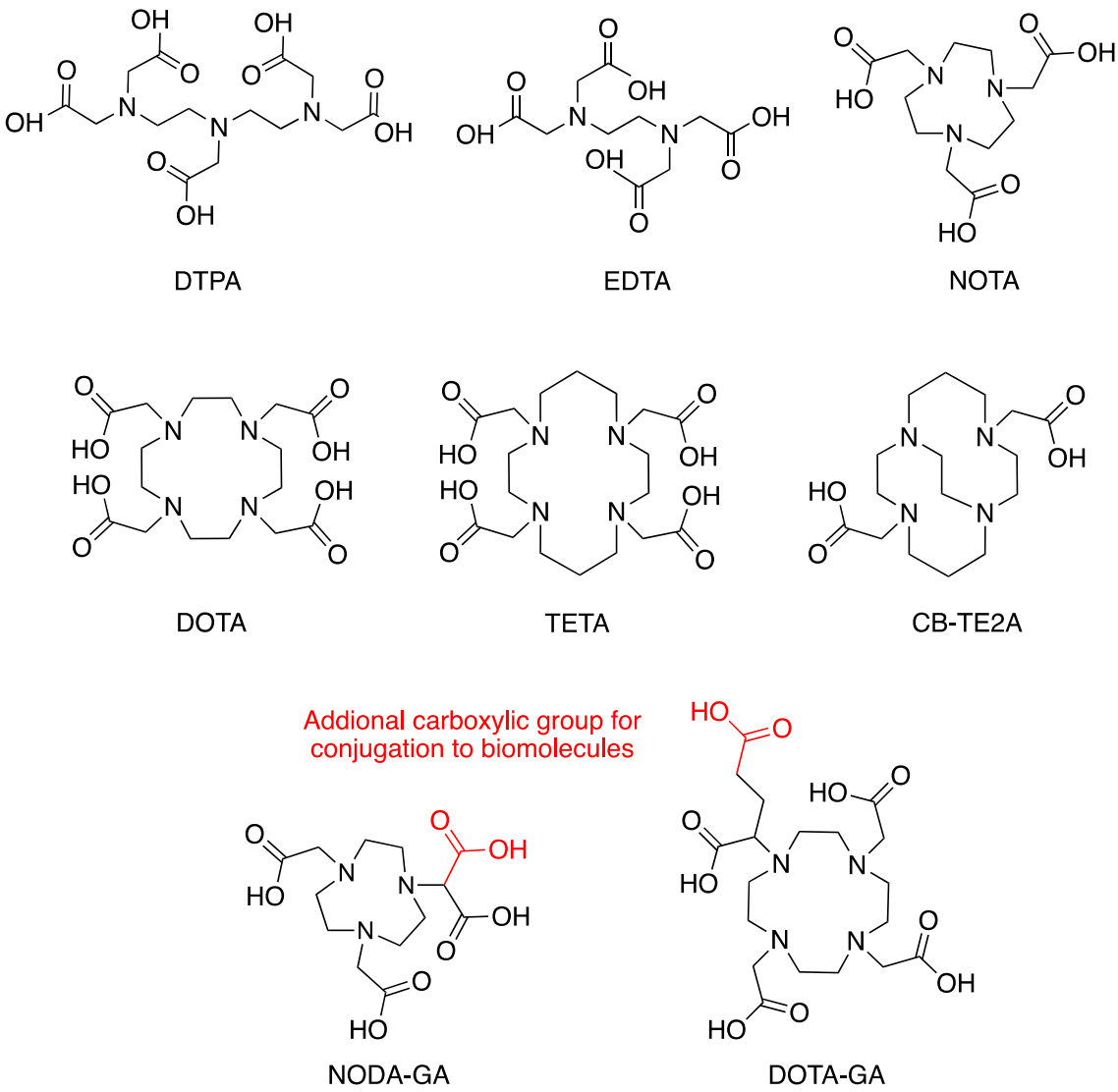

Figure 14 – Representation of some chelators explored in the literature for the stabilization of radiometals and conjugation to biomolecules.

1.9 Basic aspects of gallium radiochemistry

In nuclear medicine, the most commonly used isotopes for SPECT and PET differ based on their decay properties, imaging techniques, availability and specific applications. For example, technetium-99m (^{99m}Tc) is widely used in the clinic (> 70% of nuclear exams) for cardiac imaging, bone scans, and renal studies due to its ideal gamma energy (gamma emission of 140 keV) and short half-life (~ 6 h), making it safe and effective for routine clinical and research use. Additionally, this radionuclide is readily available from molybdenum-99/technetium-99m generators, eliminating the need for a cyclotron or a nuclear reactor, which makes it highly convenient and cost-effective for widespread use in nuclear medicine. Similarly, gallium-68 (^{68}Ga) is produced from the radioactive decay of germanium-68 (^{68}Ge) and can be also obtained using a ^{68}Ge/^{68}Ga generator, which has recently generated significant interest for applications in nuclear medicine (**Figure 15**) [92].

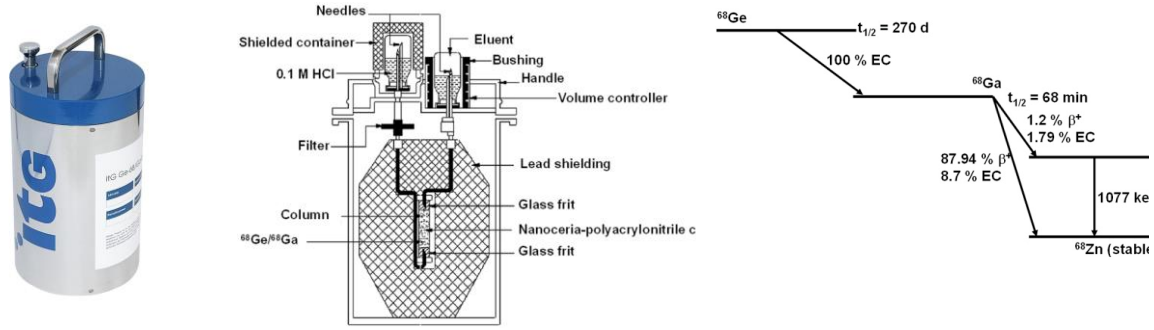

Figure 15 – 68Ge/68Ga generator based and its decay characteristics. From Ref. [92]

The long half-life of ^{68}Ge (271 days) enables the creation of cost-effective and durable generator systems, offering a major advantage over PET radionuclides typically produced by cyclotron irradiation. ^{68}Ga decays to zinc-68 (^{68}Zn) primarily through positron emission (89%) and partially by electron capture (11%), with a maximum energy of 1077 keV (**Figure 15**). Its half-life of 68 minutes makes it well-suited for labelling molecules with high clearance rates, such as low molecular weight compounds, antibody fragments and peptides, due to their rapid elimination from the body. However, for biomolecules with slower pharmacokinetics, like antibodies, ^{68}Ga is less ideal. In such cases, gallium-67 (^{67}Ga) may be a better option. Although ^{67}Ga emits gamma radiation, its longer half-life (78.3 h) allows for extended imaging studies [92].

Both ^{67}Ga and ^{68}Ga can form stable complexes with a variety of ligands containing donor atoms like nitrogen and oxygen, enabling the use of a wide range of chelating agents for complexation. Due to these advantageous properties, interest in the use of this pair of isotopes continues to grow.

^{67}Ga is well-suited for chelation with agents like DOTA, NOTA, DOTAGA, and NODAGA due to its +3 oxidation state and small ionic radius (**Figure 16**) [93]. These chelators form highly stable complexes

with ^{67}Ga, which is crucial for preventing the radiometal from dissociating *in vivo*. This stability minimizes the risk of non-specific binding and unwanted radiation exposure to non-target tissues. The strong binding affinity of these chelators ensures that ^{67}Ga remains securely attached to the targeting biomolecule, thereby enhancing the precision and efficacy of ^{67}Ga-radiopharmaceuticals used in both imaging and therapeutic applications [90].

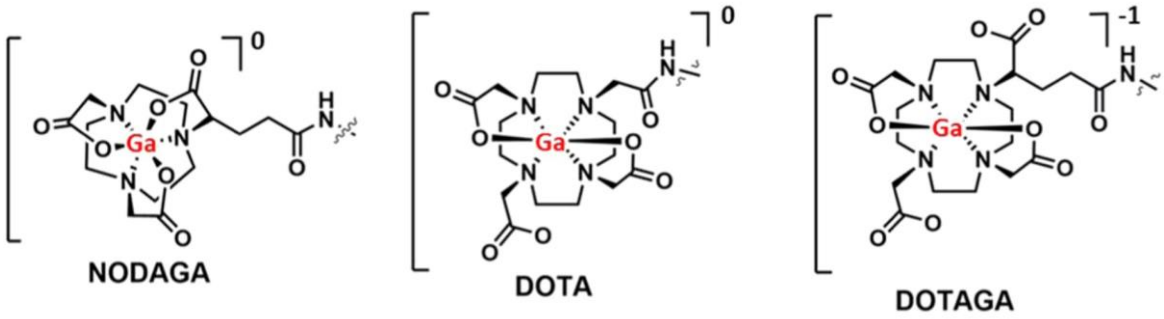

Figure 16 – Schematic structures of gallium complexes with NODAGA, DOTA and DOTAGA chelators. From Ref [93]

1.9.1 Radiolabelling of proteins

Radiolabelling peptides and antibodies is crucial in nuclear medicine for both diagnostic imaging and targeted therapy. Biomolecules can be labelled with radioisotopes either directly or indirectly. In general, the direct method involves the attachment of a chelator to a biomolecule using “cysteine or lysine chemistry”, as previously described, followed by radiolabelling (**Figure 17**). For this approach, Lysine-specific chelator such as N-hydroxysuccinimide esters or Cysteine-specific chelators such as maleimide derivatives are commercially available.

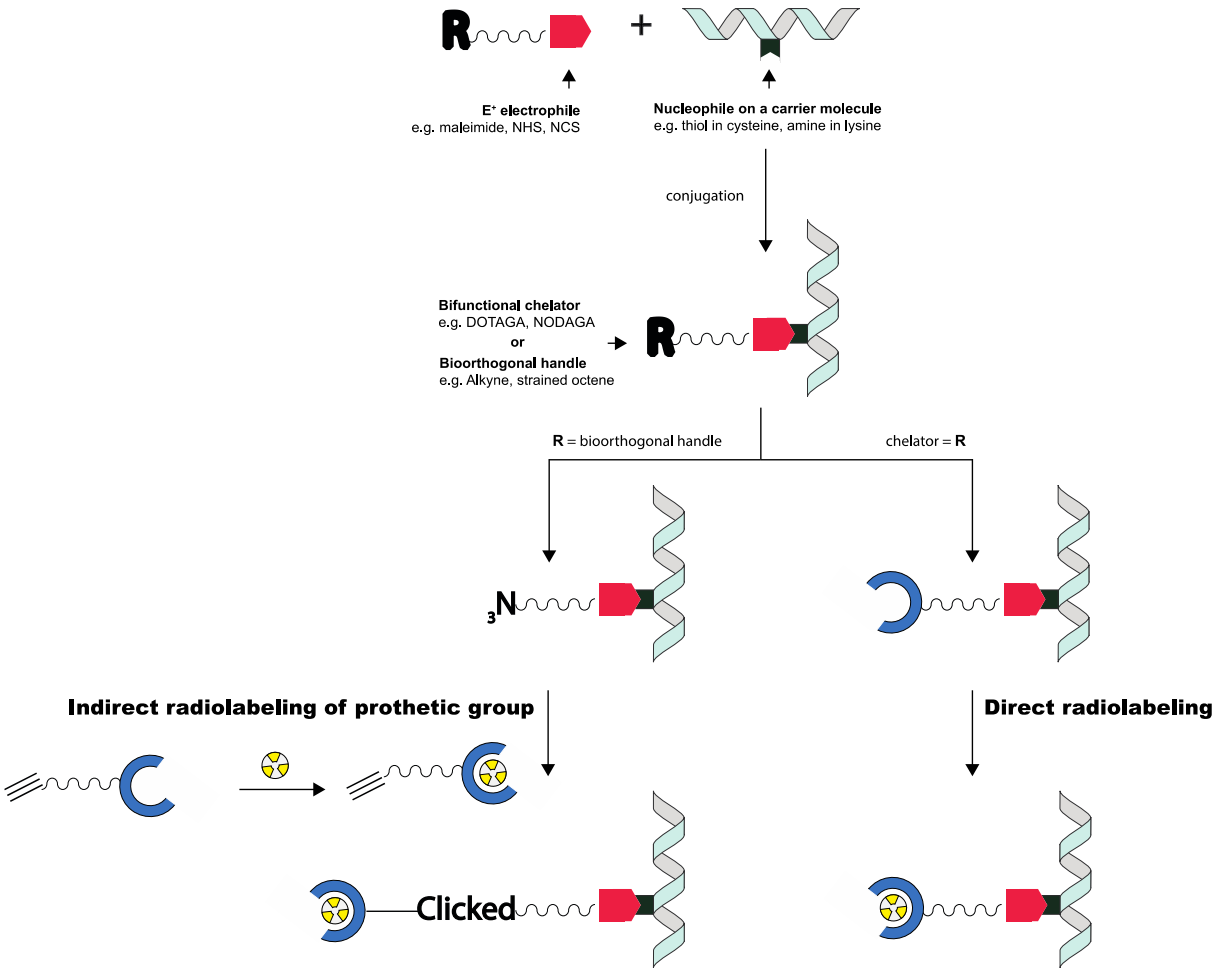

Figure 17 – Schematic Representation of the two strategies for Radiolabelling proteins for theranostic applications, emphasizing the importance of precise targeting for efficient tumor localization and minimized off-target effects. Created by BioRender.com

Indirect radiolabelling uses small molecules, or prosthetic groups, to attach the radionuclide to the biomolecule. This method is versatile and preserves the biomolecule's function. Click chemistry is often employed here, allowing for highly specific and efficient labelling under mild conditions [94]. In this context, the prosthetic group dibenzocyclooctyne (DBCO) is commonly used in SPAAC due to its ability to react with azide-functionalized biomolecules. For example, SPAAC was used to attach Fluorine-18 to peptides [95]. In this work, a [^{18}F]-labelled azide was reacted with a peptide containing a DBCO group conjugated via amide bond formation.

1.10 Theranostic compounds

While targeted therapies such as ADCs and PDCs/SPDCs have revolutionized cancer treatment by selectively delivering cytotoxic agents to tumor cells, there remains a significant need for advancements that can further optimize patient outcomes. A critical challenge lies not only in delivering the therapeutic agent precisely but also in monitoring its distribution and effectiveness in real-time. This challenge has

catalyzed the development of theranostic compounds, which represent a groundbreaking evolution in targeted therapy.

Theranostic compounds integrate therapeutic and diagnostic capabilities into a single agent, offering a dual-functionality approach. These compounds are designed to both treat the disease and simultaneously monitor the therapeutic process, enabling personalized treatment strategies. The ability to adjust treatment based on real-time data optimizes efficacy and minimizes toxicity, representing a significant advancement in bridging the gap between treatment and diagnostics in more effective and personalized cancer therapies.

Nuclear medicine, particularly with regard to applications in oncology, is currently one of the greatest components of the theranostic concept in clinical and research scenarios. Theranostics in nuclear medicine, refers to the use of radioactive compounds to image biologic phenomena, and then to use specifically designed agents to deliver ionizing radiation to the tissues that express these targets (**Figure 18**). The nuclear theranostic approach has sparked increasing interest and gained importance in parallel to the growth in molecular imaging and personalized medicine, helping to provide customized management for various diseases [96], [97].

A key aspect of this advancement is the use of paired isotopes, which enhance the efficacy of theranostic applications. Paired isotopes are chemically identical and exhibit similar half-lives, allowing the diagnostic agent to closely mirror the behavior of the therapeutic agent *in vivo*, thereby ensuring accurate dosimetry. For instance, isotopes such as lutetium-177 (^{177}Lu) and indium-111 (^{111}In) exemplify this concept. Lutetium-177 is valued for its therapeutic capabilities, emitting beta particles that effectively target and destroy cancer cells, while indium-111 is primarily employed for imaging due to its gamma emission, which allows visualization of the biodistribution of radiolabeled compounds [98].

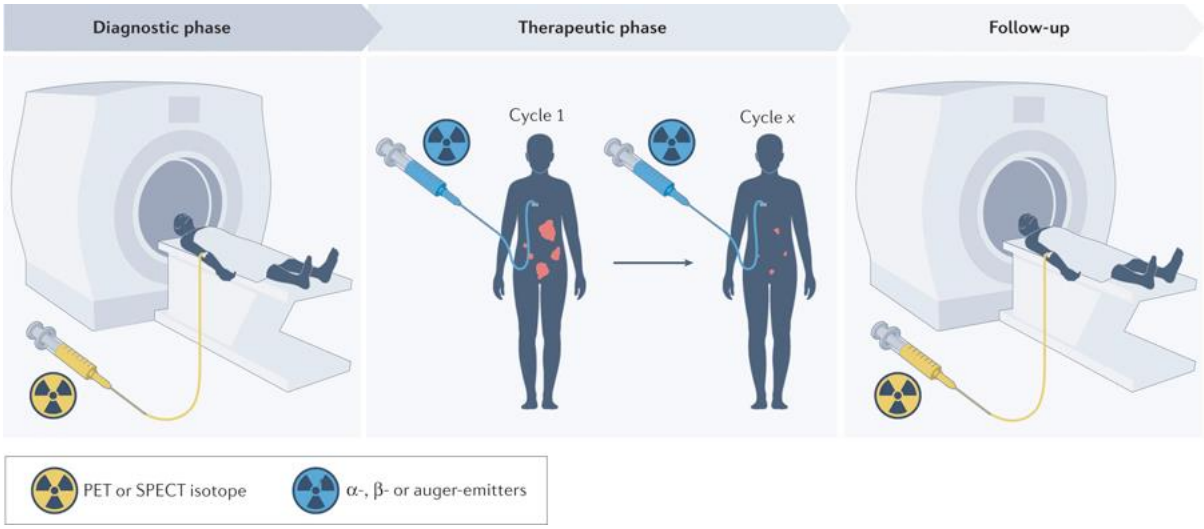

Figure 18 – Overview of the concept of radiotheranostics: radiopharmaceuticals are paired with targeted ligands to 'see with precision' and then 'treat with targeting'. From Ref. [97]

The integration of these isotopes allows researchers to develop robust theranostic agents that facilitate both targeted therapy and real-time imaging of treatment efficacy. By employing a PSMA-targeted peptide, Li et al. demonstrate how the combined use of lutetium and indium can optimize treatment planning and monitoring, ultimately improving patient outcomes in personalized cancer therapy. In contrast, non-chemically identical isotopes can lead to discrepancies in treatment assessments, underscoring the importance of utilizing paired isotopes for more effective therapies [99].

1.11 Emerging targets for cancer therapy: the role of immune checkpoint inhibitors

Over the past two decades, immunotherapies have increasingly emerged as first-line treatments for many cancers. One prominent approach is immune checkpoint blockade, which has shown encouraging results in clinical trials across various solid tumors [100]. The mechanism of action of immunotherapy is through the inhibition of the immune checkpoint ligand–receptor interactions, withdrawing the immune suppression exerted by tumor cells and enabling the immune system to recognize and destroy these cells (**Figure 19**). A key focus is the Programmed Cell Death Protein 1 (PD-1), which plays a vital role in inhibiting immune responses and promoting self-tolerance through T cells modulation. Programmed Cell Death Ligand 1 (PD-L1), a transmembrane protein, binds to PD-1, reducing the proliferation of PD-1 positive cells and inducing apoptosis.

The interaction between PD-1 on T cells and PD-L1 on tumor cells is blocked by a class of immunotherapies called PD-L1 inhibitors that prevent tumors from evading immune detection [100].

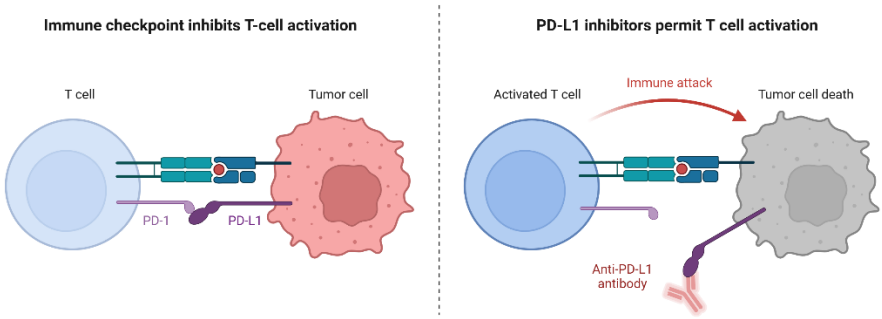

Figure 19 – Mechanism of action of immune checkpoint Inhibitor against tumor cells. Created with Biorender.com

Modifying PD-L1-targeting biomolecules could lead to innovative approaches for cancer imaging and therapy. Attaching additional functionalities, such as drugs or imaging tags, to these targeting molecules presents promising opportunities to improve these therapies by facilitating precise delivery of imaging agents or therapeutic compounds directly to the tumor microenvironment. This targeted approach holds great potential for advancing cancer diagnosis and enhancing treatment outcomes [101], [102].

1.12 Proteins targeting the PD-1/PD-L1 pathway

Recent advances in immunotherapy have significantly impacted cancer treatment, especially through checkpoint inhibitors targeting the PD-1/PD-L1 pathway.

Monoclonal antibodies (mAbs) are highly specific proteins that bind to antigens. Three targeting PD-L1 antibodies that have been investigated by FDA include Atezolizumab (Tecentriq) [103], Avelumab (Bavencio) [104], and Durvalumab (Imfinzi) [105]. These antibodies block the PD-L1 interaction with PD-1 on T cells, enhancing immune system activity against cancer cells [102]. However, Atezolizumab and Durvalumab prevent immune evasion by tumors, while Avelumab additionally induces antibody-dependent cellular cytotoxicity (ADCC) by engaging natural killer cells. Avelumab therefore has the potential to utilize both adaptative and innate immune mechanisms to destroy cancer cells. Each is approved for the treatment of specific cancers, such as non-small cell lung cancer (NSCLC), urothelial carcinoma, and Merkel cell cancer [106].

1.12.1 Miniproteins targeting the PD-L1

We envisaged that small proteins, similar to nanobodies, may preserve the potency and specificity benefits of antibodies while eliminating some of their drawbacks. Their smaller size enables better tissue penetration and faster clearance, potentially boosting efficacy and lowering side effects. Nanobodies, for example, have been successfully applied in cancer diagnostics and therapeutics, such as PD-L1-targeting nanobodies used for imaging in cancer treatment [107]. Miniproteins, owing to their versatile roles in cellular processes, are increasing their significance in cancer research. These small proteins are being explored for their potential in developing new cancer diagnostics and therapies [108]. For example, Knottins and Kalata B1 are cystine-reinforced miniproteins with notable potential in cancer therapies. Knottins are designed to specifically target cancer-related proteins, offering a precision approach to tumor treatment and potentially reducing off-target effects. Kalata B1, with its ability to enhance drug delivery, can improve the targeting of therapeutic agents directly to cancer cells, thus increasing treatment efficacy and minimizing systemic side effects. DARPins (designed ankyrin repeat proteins) are another class of binding molecules with the potential to overcome limitations of monoclonal antibodies, hence allowing novel therapeutic approaches [109]. These types of miniproteins utilize their stable structures to address various therapeutic needs effectively, making them valuable candidates for advancing cancer treatment and improving patient outcomes [110].

De novo miniproteins are a class of small proteins being developed using computational methods. Indeed, in recent decades, computational de novo protein design has enabled the creation of entirely novel protein sequences and structures from scratch without any pre-existing template or natural protein as a starting point. This research pioneered by David Baker has resulted in the discovery of many novel miniproteins targeting several receptors relevant for application in cancer [111], [112]. Based on recent progress in this field, the Bernardes group at iMM and the group of David Baker at IPD (Institute of Protein Design, Washington University), are exploring the use of miniproteins to delivery potent organic cytotoxic drugs to cancer cells in mouse models for chemotherapy [111], [112].

1.13 Objective of the study

The main goal of this study is to develop and evaluate a new class of theranostic metallodrugs that combine the benefits of ADCs and SPDCs for cancer imaging and therapy for a cancer theranostic approach. In detail, this work aims to deliver highly effective cytotoxic gold complexes selectively to tumor cells, exploring the targeting characteristics of these bioconjugates, aiming to decrease off-target effects and boost antitumor efficacy.

The Radiopharmaceutical Sciences group of C^2TN, IST, has recently reported a symmetric Au(I) bis-1,2,3-triazole-5-ylidene complex with two azide functional groups that showed high cytotoxicity on human ovarian cancer (A2780) and breast cancer (MCF-7) cell lines, surpassing the efficacy of cisplatin and auranofin by several orders of magnitude (IC_{50}:26.6 ± 1.3 nM in A2780 cells and 261 ± 75 nM in MCF-7 cells). The azide groups in the complex were chosen to introduce biorthogonality to the gold complex. Notably, the high cytotoxic activity is preserved even after modification of the azide group with a cyclooctyne partner. Having previously discussed the advantages of SPAAC, we sought to use this click chemistry reaction to attach the gold complex to proteins targeting the PD-L1 receptor. In this context, a maleimide linker equipped with a strained alkyne group was first conjugated to the antibody atezolizumab or to a miniprotein under optimized conditions (**Figure 20**). The alkyne-bearing proteins were then reacted with the azide-functionalized Au(I) complex. When these two groups interact, they undergo a SPAAC reaction, resulting in the formation of a stable bioconjugates featuring now an additional terminal azide moiety that provides a novel framework for further post-functionalization. This facilitates the incorporation of new vectors such as clickable radiochelators (e.g., NODAGA or DOTA derivatives with BCN alkyne handles) or fluorophores (fluorescent-DBCO reagents) (**Figure 20**), paving the way for the development of highly selective theranostic Au(I) complexes.

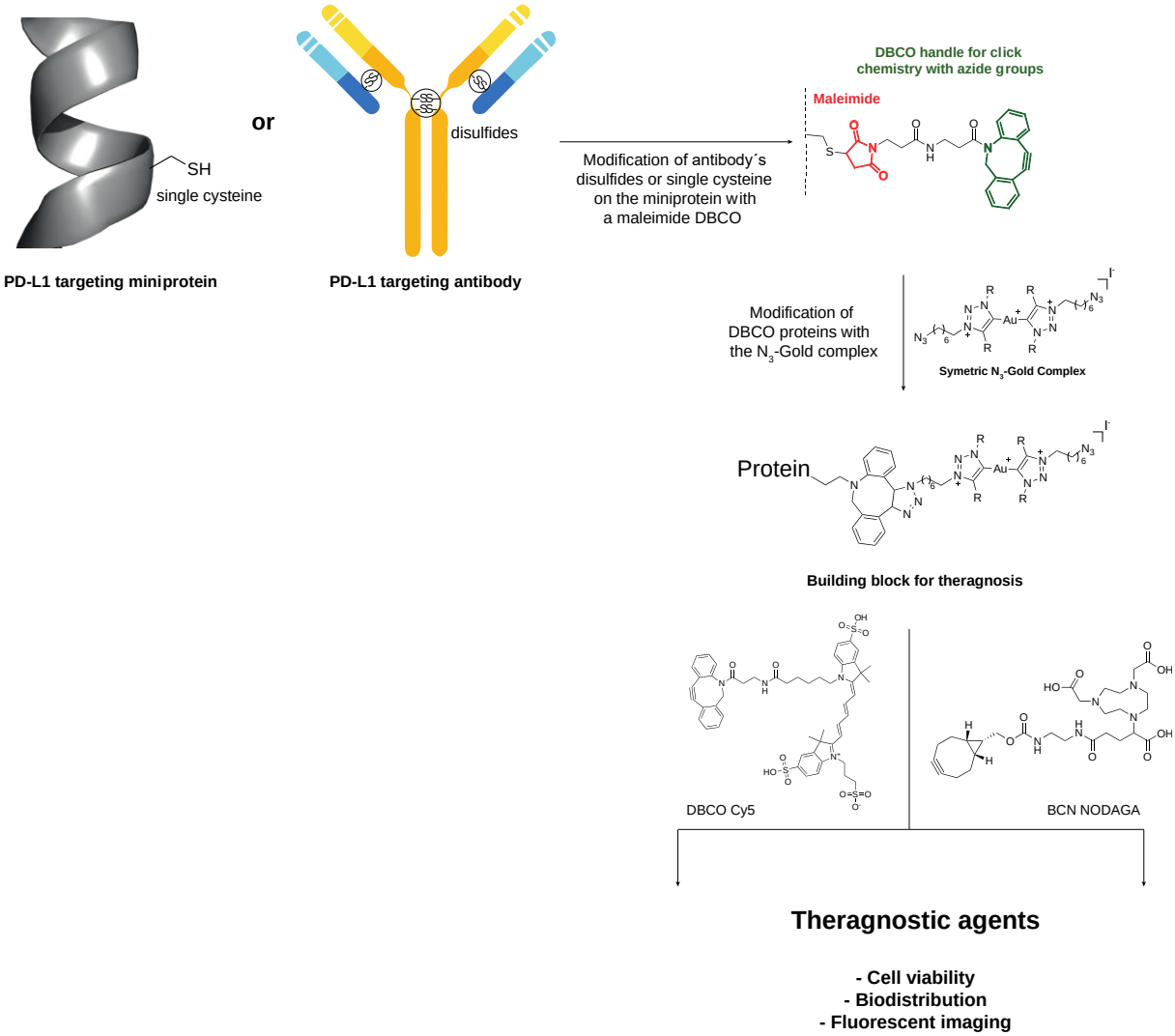

Figure 20 – Multifunctional approach to develop protein-based metallodrugs combining imaging and cytotoxic vectors for theragnosis.

The cytotoxicity of the metal-based miniprotein will be evaluated in cells using specific cancer cell lines overexpressing PD-L1. Additionally, the conjugated N_3-pendant group on the proteins will be further explored for click chemistry with NODAGA- and fluorescent-alkyne reagents. Specifically, the NODAGA-BCN will be used to radiolabel the metal-based miniprotein with a radionuclide (e.g. ^{67}Ga) to study its behavior in cells (e.g. cell uptake in PD-L1 expressing cells) and its biodistribution in mice inoculated with “PD-L1 tumors”. Similarly, the fluorescent antibody will be used for imaging of the gold therapeutic agents in mice bearing “PD-L1 tumors” by IVIS®. This approach aims to demonstrate the potential of these metal-based protein drugs as novel theranostic agents for cancer imaging and therapy.

2

MATERIALS AND METHODS

All chemical reagents and solvents acquired commercially were of reagent grade and utilized without further purification unless specifically noted.

The water (H_2O) used for the experiments was ultrapure Milli-Q water obtained from a Water Purification System.

2.1 Proteins

A mini protein, PDL1_JHR_8_7C_HIS having an internal cysteine at position 7 and a histidine tail, produced in *Escherichia coli* (E. coli) showing high affinity for PD-L1 (in the range of nM), was generously provided by Professor Gonçalo Bernardes´ laboratory at Instituto de Medicina Molecular (iMM) João Lobo Antunes. This protein, consisting of 115 amino acids (exact sequence undisclosed), was designed using computational methods (Rosetta Software) developed in Professor David Baker´s laboratory at Washington University, USA.

This mini protein has a molecular weight of 13164 Da and is supplied at a concentration of 5.2 mg/mL in phosphate-buffered saline (PBS) at pH 7.4, containing 1 mM of TCEP, a reducing agent used to prevent protein dimerization.

2.2 Antibody

Atezolizumab (Tecentriq®, F. Hoffmann-La Roche Ltd), a high-affinity human IgG1 mAb was generously provided by Rita Fior´s laboratory from Champalimaud Foundation.

Atezolizumab targets PD-L1, enhancing immune response against cancer cells by blocking PD-L1 interactions with its receptors. Each vial contains 60 mg/mL of atezolizumab and is formulated in glacial acetic acid (16.5 mg), L-histidine (62 mg), polysorbate 20 (8 mg) and sucrose (821.6 mg) at pH 5.8. Atezolizumab has a molecular weight of 145000 g/mol [113].

The antibody was produced using recombinant DNA technology in a Chinese hamster ovary (CHO) mammalian cell expression system [114], [115].

2.3 Purification of the miniprotein and the marketed monoclonal antibody

Prior to modification, the miniprotein suffered desalting using Zeba™ Spin Desalting Columns (7K MWCO, 0.5 mL, Thermo Fisher Scientific, Massachusetts, USA) to remove residual TCEP that could potentially interfere with subsequent reactions. The manufacturer's protocol, involving specific washing and centrifugation cycles, was meticulously followed. Following purification, the protein was prepared for further modification, detailed in the subsequent section.

Notably, contrary to some approaches reported in the literature for mAb like Atezolizumab, which typically involve dialysis to remove excipients, this step was omitted in our protocol [116], [117]. Despite this deviation, subsequent modification reactions proceeded successfully with high yields.

2.4 Protein and antibody modification, radiolabelling, purification and characterization

2.4.1 Protein modification

The synthesis of the PDC began with the coupling of the miniprotein PDL1_ JHR_8_7C_HIS to a maleimide bearing a DBCO group, facilitating subsequent conjugation reactions. Following this, the miniprotein was further reacted with the gold complex Autr(az/az), which was previously synthesized as described in the protocol [75] and features two azide groups per side. This enables additional conjugation with BCN-NODAGA to form a theranostic protein drug conjugate and allows subsequent labelling with gallium-67.

The initial step involved purifying the miniprotein as described in section 2.3 to remove TCEP from the storage solution. After purification, the miniprotein solution was reacted at 25 ºC with 300 rpm agitation for 1 – 2 h with 5 equivalents of the maleimide-DBCO and Autr(az/az) gold complex, both dissolved in DMF (final concentration of DMF in the reaction = 5%), and 5 eqs of BCN-NODAGA dissolved in water. Following the conjugation reactions, the PDC was purified using an Amicon column (Amicon® Ultra, 0.5 mL, 3K MWCO, Millipore) according to the manufacturer´s protocol. Protein modification was confirmed by Liquid Chromatography - Mass Spectrometry (LC-MS), ensuring the successful conjugation of the miniprotein with the desired reagents. **Table 4** shows a list of compounds used in the synthesis and their respective molecular weights.

Table 4 – Compounds used in the synthesis of the PDC

Compounds	Molecular weight (g/mol)
Maleimide DBCO ($C_{25}H_{21}N_3O_4$) Thermo Scientific	427.45
Gold complex (Autrz(az/az))	1059.07
BCN-NODAGA ($C_{28}H_{43}N_5O_9$), CheMatech	593.67

2.4.2 Antibody modification

ADC was synthesized using the same molecules as those conjugated to the miniprotein, utilizing an antibody as biological carrier. A key modification involved substituting the Maleimide DBCO linker with a Maleimide PEG DBCO linker to enhance hydrophilicity and optimize reaction yields. Additionally, for theranostic compound, the antibody was also conjugated with DBCO Cy5, a fluorophore. Detailed descriptions of new reagents are provided in **Table 5**.

Initially, the antibody suffered reduction with 20 equivalents of TCEP reagent at 37 ºC for 30 minutes to separate the light chain (LC) from the heavy chain (HC). Following reduction, the solution was allowed to react at 25 ºC with 300 rpm agitation for 1 – 2 h. ADC was formed using 20 equivalents of the same reagents as those used for miniproteins, except DBCO Cy5, which was used at 5 eqs. Conjugation reactions were purified using Dialysis Units (Slide-A-Lyzer® MINI Dialysis Unit, 1L, 7K or 20K MWCO, Thermo Scientific) and Dialysis Cassettes (Slide-A-Lyzer® MINI Dialysis Cassettes, 0.1 mL – 0.5 mL, 3.5K MWCO, Thermo Scientific) to remove unreacted reagents and by-products. Protein modification was verified by LC-MS analysis. Prior to analysis, antibodies were treated with 20 eqs of TCEP at 37 ºC for 30 minutes to reduce disulfide bonds, ensuring free thiol groups for accurate structural analysis. **Table 5** shows a list of compounds used in the synthesis, including their respective molecular weights.

Table 5 – The new compounds used for the conjugation of the antibody

Compounds	Molecular weight (g/mol)
EZ-Link™ Maleimide-PEG4-DBCO ($C_{36}H_{42}N_4O_9$) Thermo Scientific	674.74
DBCO Cy5 ($C_{64}H_{86}N_6O_{11}S_3$) Sigma-Aldrich	1211.59

2.4.3 Characterization of the conjugates

2.4.3.1. LC-MS analysis of Native Proteins, Antibodies, and Their Conjugates

The native proteins and native antibody, as well as their conjugates, were analysed using LC-MS. This analysis was conducted on a Waters Acquity UPLC system equipped with a single quadrupole mass detector (QDa). The separation was achieved using a Xbridge BEH C4 column (Waters, 3.5 µm, 300 Å pore size, 2.1 x 100 mm) maintained at 40 ºC. The mobile phase consists in 0.1 % v/v formic acid in distilled water (solvent A) and 0.01 % v/v formic acid in acetonitrile (solvent B). The gradients of solvents A and B were applied according to the following method: 10 % B for 5 min, followed by a slow gradient to 100 % B in 15 min. At 20.1 min, B returned to 10 %, remaining at this % for a further 7.9 min to re-equilibrate the column. The total run time was 28 min at a flow rate of 0.2 mL/min. The injection volume was 10 µL. The electrospray source was operated at a capillary voltage of 1.5 kV and a cone voltage of 20 V. Nitrogen was used as the desolvation gas at a total flow rate of 800 L/h with a cone volume of 1 L/h and the temperature was set at 400 ºC. To obtain the ion series, protein peaks from the total ion chromatogram were selected for integration. The mass spectra were then reconstructed using the MaxEnt algorithm pre-Installed in the MassLynx software (Waters version 4.1) using a maximum

entropy deconvolution range between 2.000 – 30.000 Daltons for mini proteins and 10.000 – 70.000 Daltons for antibodies.

2.4.3.2. Quantification of the conjugates using Quibit™ 4 Fluorometer

After modification and purification, the protein and antibodies were quantified using a Qubit™ 4 Fluorometer (Thermo Scientific, Invitrogen Qubit Assays). This assay utilizes target-selective dyes that emit fluorescence only when bound to their specific protein targets. First, the Qubit™ working solution was prepared by diluting the Qubit™ reagent 1:200 in Qubit™ buffer. For each standard and sample, 200 µL of the working solution was prepared. In each tube, 190 µL of the working solution was combined with 10 µL of the standard or sample. The tubes were then vortexed for 2 – 3 seconds to ensure proper mixing. Following mixing, the samples were incubated for 15 minutes at room temperature to allow the dye to bind to the protein targets. After incubation, the tubes were placed in the Qubit™ fluorometer, and the fluorescence was measured according to the manufacturer's instructions. This method ensured accurate quantification of the protein, and antibody present in the samples.

2.4.4 Purification of the conjugates

As mentioned in the section 2.4.1 and 2.4.2, the purification of the miniprotein and the antibody was conducted using amicon columns and dialysis, respectively. It´s crucial to select the appropriate molecular weight cutoff for both the amicon column and dialysis membrane.

For miniproteins, the buffer solution used was PBS at pH 7.4 and for atezolizumab, it was 5 mM L-histidine at pH 5.8.3

To initiate the purification of the miniprotein, the Amicon Ultra-0.5 centrifugal filter unit was prepared by adding 500 µL of PBS and centrifuging at 14000 x g for 5 – 10 minutes to remove the PBS. This equilibration step was repeated once for thorough preparation. The miniprotein sample was then loaded into the prepared filter device and centrifuged at 14000 x g for 10 minutes. Throughout centrifugation, the filter unit was monitored every 5 minutes to prevent sample over-concentration. After the initial spin, 500 µL of fresh PBS was added to the concentrated protein sample in the filter device, followed by centrifugation at 14000 x g for 10 minutes. This buffer exchange step was repeated 2 – 3 times to effectively remove unwanted salts or small molecules. Upon completing the final centrifugation, the purified miniprotein was collected by inverting the filter device into a new collection tube. The device was then centrifuged at 1000 x g for 2 minutes to recover the purified and concentrated miniprotein sample. Subsequently, the volume of the recovered sample was measured using a pipette, and the miniprotein concentration was determined with an appropriate protein assay method, such as the Qubit Fluorometer assay. Finally, the purified miniprotein was stored under recommended conditions until further use.

To the purification of the antibody, the dialysis devices were hydrated according to the manufacturer's instructions, and the antibody solution was transferred into the devices, leaving space for expansion. The units were securely sealed and immersed in a beaker filled with a large volume of buffer solution. The beaker was placed on a stirring device to ensure continuous movement and prevent concentration

gradients. Dialysis was conducted at 4 °C for 4 to 24 h, with buffer changes every 2 to 4 h, typically three times. After dialysis, the units were removed, and the purified antibody solution was transferred to a clean container. The concentration and purity of the antibody were assessed using appropriate assays.

2.4.5 Manipulation of radioactive compounds

The handling of radioactive compounds strictly adhered to safety and radiological protection standards in laboratories equipped with appropriate facilities, including negative pressure ventilation systems. Radioactive solutions were stored in thick lead containers and managed with utmost care. Before and after each use, the background radiation levels were measured using a portable digital radiation meter. All manipulations of radioactive solutions were performed inside a laminar flow chamber, protected by a lead-shielded screen. Additionally, the absorbed radiation dose during experimental procedures was periodically monitored by reading individual chest dosimeters.

2.4.6 Radiolabelling with Gallium (^{67}Ga)

2.4.6.1 ^{67}Gallium citrate transformation

5.5 mL of ^{67}Ga-citrate (205 MBq in 5.5 mL, Curium, Netherlands) were converted to ^{67}Ga-chloride ($^{67}GaCl_3$) using a specified procedure [118]. Initially, a Silica Light SEP-PAK column (Waters, USA) was washed with 10 mL of H_2O at 1 mL/min to equilibrate the column and remove any residual impurities. The ^{67}Ga-citrate solution was then applied to the column. To effectively remove the citrate, the column was gently eluted with 5 mL of H_2O, and the retention of ^{67}Ga in the SEP-PAK was monitored using a gamma counter (CRC®-55tW Curiemeter, Capintec) to ensure efficient separation from the citrate ions. Next, 0.5 mL of 0.1 M hydrochloric acid (HCl) solution was added to the column, and the first fraction (F1) was collected. This fraction typically contains minimal or negligible radioactivity. The acid wash step (0.1 M HCl) was repeated four times to obtain subsequent fractions: F2, F3, F4 and F5, which were collected sequentially. Finally, to dry the column and recover any remaining activity, 0.5 mL of air was through the SEP-PAK, and the residual activity was collected in fraction F5. The activity of all collected fractions (F1 to F5) was measured using the gamma counter to determine the distribution and purity of ^{67}Ga-chloride. Upon completion of the protocol, the total recovered activity and efficiency of the conversion process were assessed based on the gamma counter measurements of each fraction.

2.4.6.2 Radiolabelling of protein/antibody NODAGA-conjugates with gallium-67

After obtaining $^{67}GaCl_3$, the solution was mixed with 0.1 M sodium acetate ($C_2H_3NaO_2$) solution adjusted to pH 5 in a 1:3 ratio. Following pH adjustment, protein/antibody-maleimide-gold complex-NODAGA conjugates were reacted with $GaCl_3$ in a 1:1 ratio (final concentrations varied in each radiolabelling experiment). The reactions were conducted at 37 °C for varying durations of 20 minutes, 1h, and 2h with agitation. Reaction progress was monitored using instant thin layer chromatography with a

silica gel (iTLC-SG) and Reversed-Phase High-Performance Liquid Chromatography (RP-HPLC) analysis. The final radioactivity of the solutions containing ^{67}Ga-labeled compounds was quantified using a gamma counter.

For cell and *in vivo* assays involving the miniprotein, the radiolabeled protein was purified using an Amicon Ultra-0.5 mL 3 kDa filter to separate it from free gallium precursor. The purity of the purified samples was confirmed by iTLC-SG and HPLC analysis.

2.4.7 Characterization of the radiolabeled compounds

2.4.7.1 iTLC

To determine labelling yields, iTLC was employed, which measures the distribution of radioactivity between the radiolabeled compound and free gallium-67. Strips of silica gel-impregnated glass microfiber chromatography paper (Agilent Technologies, Santa Clara, CA, USA) were used as the substrate. A volume of 3 µL of the radiolabeled sample was carefully applied to the iTLC strip near one end. A mixture of ethanol and hydrochloric acid (HCl, 0.6 M) was prepared in a 99:1 (v/v) ratio and used as the elution solvent. As the solvent migrated, free gallium-67, being less bound to the silica gel, moved toward the front (lower retention factor (Rf) value). Conversely, the radiolabeled protein, bound more strongly to the silica gel, remained near the application point (higher Rf value).

2.4.7.2 RP-HPLC

RP-HPLC is a technique continuously growing in purification and analysis of peptides and uses the concept of polarity, therefore the most apolar compound takes longer to be eluted since it has stronger interactions with column's nonpolar packing. In addition, RP-HPLC is versatile since mobile phases can be polar such as H_2O and Acetonitrile (ACN) with Trifluoroacetic Acid (TFA) which are best for peptides [119], [120]. RP-HPLC analytical control of the radiolabeled compounds was conducted in a Perkin Elmer LC Pump 200 with a Berthold-LB 509 Radioflow detector and a Shimadzu SPD 10 AV UV/Vis detector. Degassing the solvents through Uniflow Degasys DG-3210 in a flow of 1.0 mL/min detected at 220 nm (wavelength absorbed by most compounds) in a Macherey Nagel Analytical, EC250/3 Nucleosil 100-5 C18 column with Method A (**Table 6**).

Table 6 – Method (A) for HPLC analysis of radiolabeled conjugates Eluent A: TFA 0.1% in H_2O; Eluent B: TFA 0.1% in ACN.

Step	Time (minutes)	%A	%B
0	5.0	95.0	5.0
1	20.0	0.0	100.0
2	5.0	0.0	100.0
3	1.0	95.0	5.0
4	4.0	95.0	5.0

2.5 Biochemical characterization of the fluorescent antibody

SDS-Polyacrylamide Gel Electrophoresis (SDS-PAGE) was conducted to separate the light chain, heavy chain, and heterogeneous IgG antibodies based on their electrophoretic mobility. The concentration of the resolving gel, ranging between 10% and 20%, was selected according to the size of the antibodies. The resolving gel consisted of 1.5 M Tris buffer (pH 8.8), 30% acrylamide/bisacrylamide solution (Invitrogen, Karlsruhe), 10% SDS (w/v), deionized distilled water (ddH_2O), 10% ammonium persulfate (APS, Merck, Dresden), and 5 µL N',N',N'-Tetramethylethylenediamine (TEMED, Sigma-Aldrich, Deisenhofen). The exact volumes were adjusted based on the desired gel concentration (e.g., 10% for smaller proteins, 20% for larger proteins). The mixture was poured into the gel casting apparatus and allowed to polymerize for 30 – 45 minutes. The stacking gel (4% acrylamide) was prepared with 30% acrylamide/bisacrylamide solution, 0.5 M Tris buffer (pH 6.8), 10% SDS (w/v), ddH2O, 10% APS, and 5 µL TEMED. The stacking gel mixture was poured on top of the polymerized resolving gel, and a silicon comb was inserted to create wells. The gel was left to polymerize completely for 20 – 30 minutes. For sample preparation, 16 µL of each antibody sample was mixed with an equal volume of 4X Laemmli buffer (containing SDS and a reducing agent such as DTT or β-mercaptoethanol) and heated at 95 °C for 5 minutes to denature the proteins. After cooling, the samples were loaded into individual wells, and 5 µL of PageRuler Prestained Protein Ladder (Thermo Scientific) was loaded into a separate well for molecular weight estimation. The gel was placed in an electrophoresis chamber filled with SDS running buffer (25 mM Tris, 192 mM glycine, and 0.1% SDS). Electrophoresis was conducted at a constant current of 100 mA for 30 – 60 minutes or until the dye front reached the bottom of the gel. Electrophoresis was performed at room temperature. After electrophoresis, the gel was carefully removed from the apparatus and imaged using an Amersham Imager to capture the protein bands before staining. Following imaging, the gel was stained with Coomassie Brilliant Blue R-250 solution for 15 minutes to visualize the protein bands. The gel was then destained with a destaining solution (methanol, acetic acid, and water) until clear protein bands were visible.

2.6 Assays In murine cancer cell lines

2.6.1 Cell Lines and culture conditions

The A20 and MC38 cell lines were selected for this study due to their significant relevance in immune-oncology research, particularly for examining responses to PD-1/PD-L1 inhibitors. The MC38 cell line was provided by Professor Gonçalo Bernardes from iMM. Whenever cell lines are acquired from an external source, it is essential to evaluate them for mycoplasma contamination. Mycoplasma contamination can compromise the integrity and validity of experimental results by significantly affecting cell physiology and experimental outcomes. To address this concern, a small volume of cell culture supernatant was collected from the MC38 cell line for mycoplasma testing. The mycoplasma testing was performed following the manufaturer's protocol to ensure accurate and reliable results [121].

Murine B-cell lymphoma cell line (A20) and Murine Colorectal Carcinoma cell line (MC38) were expanded and maintained in T75 culture flasks. A20 cells were cultured in Roswell Park Memorial

Institute (RPMI) 1640 Medium with GlutaMAX supplement (Gibco™ by Thermo Fisher Scientific, Paisley, UK), while MC38 cells were cultured in Dulbecco's Modified Eagle Medium (DMEM) with GlutaMAX supplement (Gibco™ by Thermo Fisher Scientific, Paisley, UK). Both media were supplemented with 10% (v/v) fetal bovine serum (FBS) (Gibco™ by Thermo Fisher Scientific, Grand Island, New York, USA). Cultures were maintained in a humidified atmosphere containing 5% CO2 at 37 °C.

Cells were subculture upon reaching 70% - 80% confluence to prevent contact inhibition and lack of nutrients. Daily, cultures were examined under an inverted optical microscope (Zeiss, Primovert, New York, USA) for contamination, cell growth, and morphological assessment.

For the MC38 cell line, the original medium was aspirated, and cells were washed with 1x PBS to remove any residual culture medium. The MC38 cells were then detached from the culture flask using TrypLE™ Express (Gibco™ by Life Technologies, Invitrogen, Carlsbad, California, USA) for 3 – 5 minutes in a 5% CO_2 humidified incubator at 37 °C. Trypsin works by cleaving peptide bonds on the C-terminal sides of lysine and arginine, thereby dissociating adherent cells. To inhibit the enzymatic activity of Trypsin, cell culture medium was added at a 2:1 Trypsin volume ratio. If cell counting was required, the cells were then centrifuged at 1500 g for 5 minutes at 20 °C. After centrifugation, the supernatant was aspirated, and the cell pellet was resuspended in fresh culture medium.

For the A20 cell line, which grows in suspension, the entire culture volume was transferred to a 15 mL Falcon tube and centrifuged at 1000 g for 5 minutes at 20 °C. The supernatant was discarded, and the cell pellet was resuspended in the appropriate medium.

2.6.2 Cell counting

For cell counting, 10 µL of the resuspended cell pellet was diluted in 0.4% (v/v) trypan blue solution (Sigma-Aldrich, UK). The dilution ratios were 1:3 for A20 cells and 1:2 for MC38 cells. From this diluted sample, 10 µL was pipetted onto a hemocytometer.

Trypan blue is a vital stain that permeates only cells with compromised membranes, thus enabling the differentiation between viable (translucent) and non-viable (blue-stained) cells. The viable cells were counted using an inverted optical microscope.

The cell concentration (cells/mL) was calculated using the **Equation 1**, adjusting for the dilution factor and hemocytometer volume (10^4 is the volume conversion factor for the hemocytometer (mL^{-1})). The total number of cells was calculated by multiplying the cell concentration by the total volume of the resuspended pellet and represented by **Equation 2**. To obtain a specific cell concentration, the necessary volume of medium was calculated and used to resuspend the cell pellet. The percentage of cell death or the viability was determined by comparing the number of dead cells to the total number of cells counted (**Equation 3**).

Equation 1 – Cell concentration (cells/mL)

$$\boldsymbol{Cell\ Concentration} = \left(\frac{\boldsymbol{Number\ of\ viable\ cells\ counted}}{\boldsymbol{Number\ of\ quadrants\ counted}}\right) \times \boldsymbol{Dilution\ Factor} \times \mathbf{10^4}$$

Equation 2 – Total Number of Cells

$$\boldsymbol{Total\ Number\ of\ Cells} = \boldsymbol{Cell\ Concentration} \times \boldsymbol{Total\ Volume\ of\ the\ Pellet\ Resuspended\ in\ Medium}$$

$$Volume\ of\ Medium = \frac{Desired\ Cell\ Concentration}{Cell\ Concentration} \times Total\ Volume\ of\ the\ Pellet\ Resuspended\ in\ Medium$$

Equation 3 – Cell´s Viability

$$\%\ Cell\ death = \left(\frac{Number\ of\ Death\ Cells}{Total\ Number\ of\ Cells\ Counted}\right) \times 100$$

Optimal range falls between 20 – 100 cells per cm^2. Desired dilutions can be done after this step in a new flask. The cells were maintained in the incubator at 37 °C, 5% CO_2 for continued culture. Any remaining volume of the cell suspension was used as needed for further experimental procedures.

2.7 Biological Evaluation Studies

2.7.1 *In vitro* studies in murine cancer cell lines

2.7.1.1 Cell Viability Assay

To evaluate the cytotoxic effects of the gold complex on both cell lines (A20 and MC38), we conducted a cell viability assay [122]. In brief, dispense 190 µL of cell suspension (5 × 10^3 cells) into each well of a 96-well clear, flat-bottom plate. Incubate the plate overnight in a humidified incubator at 37 °C with 5% CO_2. After the overnight incubation, add 10 µL of various concentrations of miniproteins dissolved in PBS or PBS alone to the culture media in each well. Ensure proper mixing by gently swirling the plate. Incubate the plate for 72 h in the same humidified incubator. After the 72 h incubation, add 10 µL of Cell Titer-Blue® reagent to each well. Incubate the plate for an additional 3 h at 37 °C in a 5% CO_2 incubator. Measure the fluorescence using a Thermo Scientific™ Varioskan™ LUX plate reader, controlled by Thermo Scientific SkanIt® Software, at an excitation wavelength of 560 nm (20 nm bandwidth) and an emission wavelength of 590 nm (10 nm bandwidth). Determine the percentage of cell viability using the following equation:

Equation 4 – Percentage of cell viability

$$cell\ viability\ (\%) = \left(\frac{mean\ fluoresncence\ in\ test\ wells}{mean\ fluorescence\ in\ control\ wells}\right) \times 100$$

Recommended Controls

1) No-Cell Control: Set up triplicate wells without cells to serve as the negative control to determine background fluorescence that may be present in the assay.

2) Untreated Cells Control: Set up triplicate wells with untreated cells to serve as a vehicle control. Add the same solvent used to deliver the test compounds to these control wells.

3) Positive Control for Cytotoxicity: Set up triplicate wells containing cells treated with a known cytotoxic compound to serve as a positive control, validating the assay´s ability to detect cell death.

2.7.1.2 Cellular uptake Assay

Cellular uptake assays with 67Ga-protein were performed in the A20 cell line, seeded at a density of 200000 cells per well in 24-well plates with 250 µL RPMI containing 10% FBS and 1% penicillin/streptomycin antibiotic solution. Cells were allowed to multiply overnight under standard culture conditions. On the following day, the cells were exposed to ^{67}Ga-BCN-NODAGA-gold complex-maleimide-DBCO-miniprotein (approximately 200000 cpm in 250 µL or 2 µCi/mL of assay medium: RPMI with 50 mM 4-(2-hydroxyethyl)-1-piperazineethanesulfonic acid (HEPES) and 0.4% (w/v) BSA) for a period ranging from 5 minutes to 3 h. The assay was conducted under four different conditions: at 37 °C and 5% CO_2, at RT and at 37 °C, 5% CO_2 but with the receptors blocked with the antibody atezolizumab and with the native miniprotein without any conjugation reaction. The receptor blockers were added 30 minutes before the cells were exposed to ^{67}Ga-protein. Incubation was terminated by removing the cells and washing the wells with 500 µL of PBS containing 0.2% BSA into a 2 mL Eppendorf tube. The solution was centrifuged for 5 minutes at 180 g (1000 rpm), and the medium was removed. To wash away excess medium, the cells were resuspended in 500 µL of PBS with 0.2% BSA and centrifuged again. The cell pellet was then measured using a Hidex AMG Automatic Gamma Counter. The percentage of cell-associated radioactivity was calculated and represented as a function of incubation time. Uptake studies were conducted with at least three replicates for each time point.

2.7.2 *In vivo* studies in animal models

2.7.2.1 Establishment of the animal model

Biological studies of the antibodies with a fluorophore were conducted on mice with subcutaneous tumours resulting from the inoculation of A20 cells. A total of 8 mice (BALB/c), each weighing approximately 25 g, were included in the study. This part of the work was performed by Ana Raquel from Bernardes Lab but followed by the author of this thesis.

Biological studies of the miniprotein with ^{67}Ga were conducted on mice with subcutaneous tumors resulting from the inoculation of A20 cells. A total of 9 mice (BALB/c), each weighing between 21 g, were included in the study. Each mouse (8 weeks old) was subcutaneously injected with 100 µL of a Matrigel:PBS 50:50 (v:v) mixture containing $\sim 5 \times 10^6$ of A20 cells. Tumor growth was determined by measuring the tumors using a digital caliper twice a week. Tumors with 100 mm^3 developed after 10 to 12 days after inoculation. The volume of A20 spheroid tumors was calculated using **Equation 5**. Mice

were maintained in a temperature and humidity-controlled room with 12h light/12h dark schedule and access to food and water with a normal diet ad libitium until the completion of the study.

Equation 5 – Determination of the volume of A20 spheroid tumor

$V = \frac{4}{3} \times \pi \times r^3$, where r represents the radius of the sphere.

2.7.2.2 *In vivo* Fluorescence Imaging

The animals were intravenously injected in the tail with 100 µL (-18 nM/kg) of the Bevacizumab Maleimide DBCO Gold complex DBCO Cy5 or Atezolizumab Maleimide DBCO Gold complex DBCO Cy5, the synthesized ADC with a fluorophore to check whether the antibody accumulates in the tumour. After 1, 6, 24 and 48 h of administration of the imaging agent, the mice were anesthetized, according to approved protocols to minimize movement during imaging, and positioned on the imaging stage of the IVIS Lumina system to track the drug distribution. Before, the IVIS Lumina system was allowed to warm up according to manufacturer specifications to ensure optimal performance and the appropriate camera settings were set up. A mouse injected with PBS, was used as negative control, which shows the absence of autofluorescence in the tumors and record the background fluorescence from the animal and surroundings. To selectively visualize the fluorescence of the imaging agent a 646 nm excitation wavelength and a 662 nm emission filter were chosen.

These studies were conducted by Ana Raquel from iMM and followed by the author of this thesis.

2.7.2.3 Biodistribution

The animals were intravenously injected in the tail vein with 100 µL (around 5 MBq) of the radioactive preparation of the protein conjugated with ^{67}Ga. After 1 and 4 h of administration of the radiolabeled compound, the mice were sacrificed by cervical dislocation to study the biodistribution of the radiolabeled compound. The total administered radioactivity and the remaining radioactivity in the sacrificed animal were measured in an ionization chamber (Aloka, Curiemeter IGC-3). It was assumed that the difference in activity in the animal after injection and sacrifice was due to excretion.

Blood samples were collected when the animal was dissected and the main organs were removed, weighed, and counted in a gamma counter (Hidex AMG Automatic Gamma Counter, Hidex). The accumulation of activity in the tissues was calculated and expressed as a percentage of the injected dose per organ (% ID/organ) and/or as a percentage of the injected dose per gram of tissue (% ID/g of organ). The experimental conditions for conducting the biological assays complied with the technical guidelines for the housing and care of small rodents, as approved by DL 129/92 of July 6 and No. 197/96 of October 16, which transpose into domestic legal order Directive No. 86/609/EEC, establishing minimum standards for the protection of animals used for experimental and other scientific purposes. These studies were conducted by Dr. Lurdes Gano and Elisabete Correia (C^{2}TN) and accompanied by the student.

3

RESULTS AND DISCUSSION

3.1 Introduction to the chapter "Results and Discussion"

The main objective of this work was to explore the potential of miniproteins targeting the PD-L1 receptor as carriers for targeted delivery of metalloconjugates to tumors for cancer imaging and therapy. The "PD-L1 miniprotein", produced in *E. coli* with high affinity for PD-L1 (nM range), was kindly provided by Professor Gonçalo Bernardes from iMM. This protein, consisting of 115 amino acids (undisclosed sequence, 13164 Da), was designed using computational methods (Rosetta software) by the laboratory of Professor David Baker at Washington University, and include one cysteine at position 7 of the amino acid sequence that was explored for protein conjugation with maleimide chemistry (**Figure 21**). In this approach, a maleimide linker containing a strained alkyne group was first conjugated to the miniprotein under optimized conditions. The alkyne-functionalized protein was then reacted with a symmetric Au(I) complex having two azide groups, via a SPAAC reaction. This resulted in the formation of a bioconjugate with an additional terminal azide moiety, providing a versatile platform for further functionalization with a clickable chelator (e.g., NODAGA BCN), facilitating the development of selective theranostic Au(I) complexes after radiolabelling with ^{67}Ga. The potential for diagnostic and therapeutic applications of the modified miniprotein was evaluated through a series of *in vitro* and *in vivo* tests, which are discussed in the following sections.

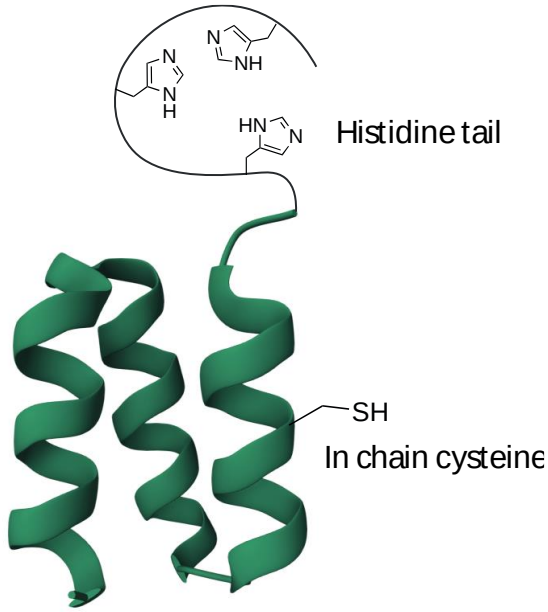

Figure 21 – Schematic representation of the PD-L1 miniprotein used in this study having one free cysteine for protein conjugation and a histidine tail.

3.1.1 Conjugation of miniprotein with the Maleimide-DBCO

The miniprotein was desalted to PBS (as described in section 2.3) before being conjugated to Maleimide DBCO (Mal DBCO), a linker known for its high reactivity toward cysteine residues. This linker facilitated the attachment of the DBCO handle to the PD-L1 miniprotein for further reaction by click chemistry (**Figure 22**).

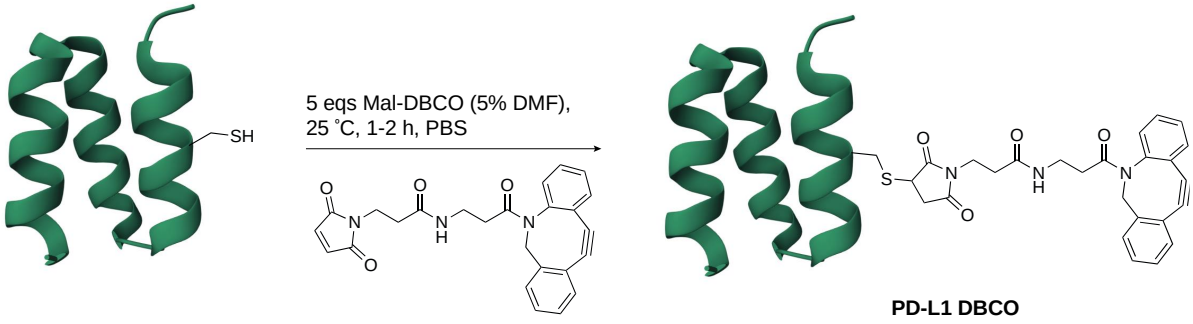

Figure 22 – Optimized conditions for conjugation of the PD-L1 miniprotein to the Maleimide DBCO linker.

Using 5 equivalents of Mal DBCO the reaction proceeded to completeness after 1 to 2 h at 25 ºC, as confirmed by the consumption of the starting protein observed by ESI LC-MS analysis. **Figure 23** and **24** shows a typical analysis of a conjugation reaction by LC-MS, where the ESI-MS spectrum of the native miniprotein (**Figure 23**) is compared with the spectrum of the conjugated miniprotein (**Figure 24**).

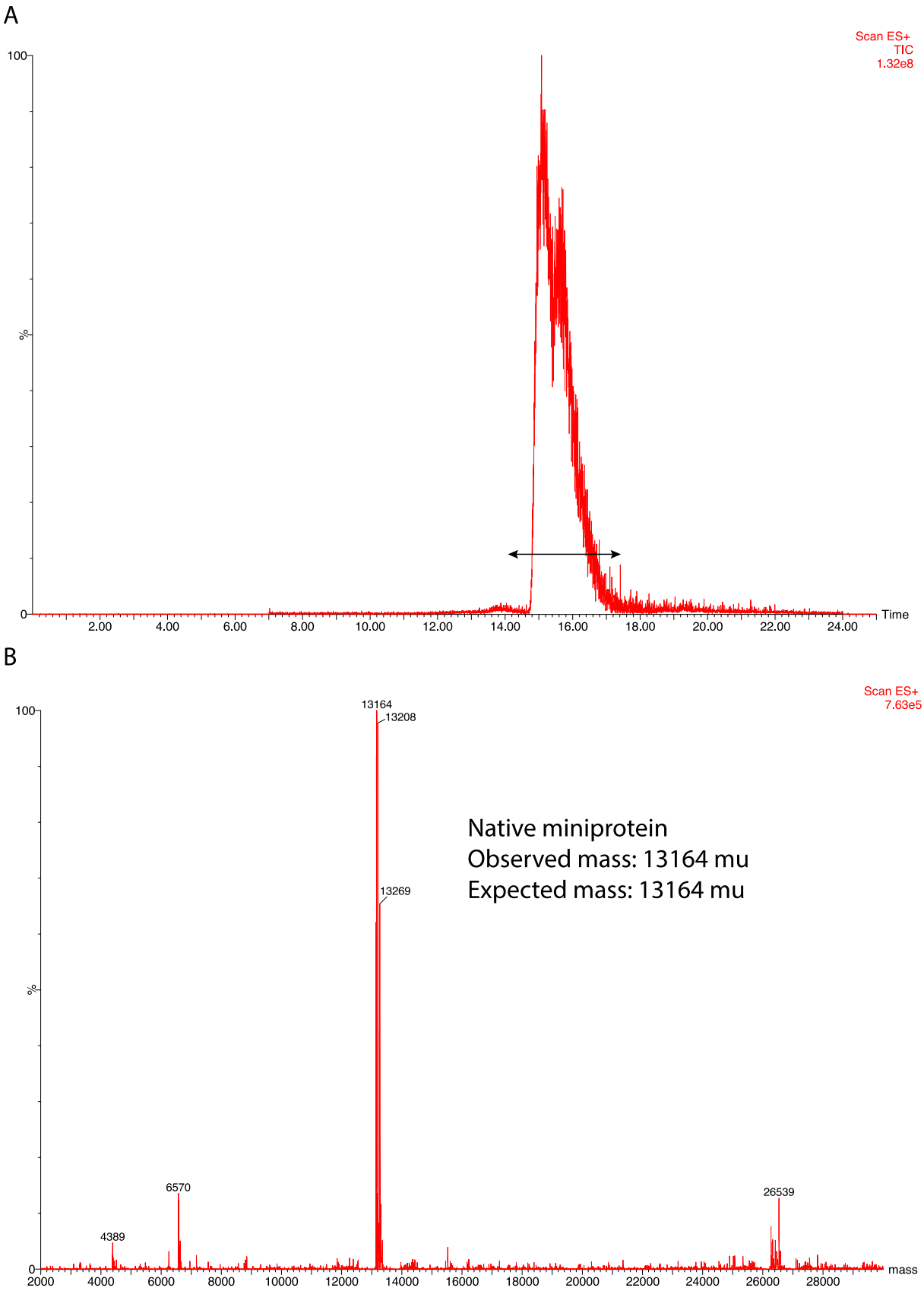

Figure 23 – Native protein. A – Total ion ESI LC-MS chromatogram of the native protein; B – Deconvoluted mass spectrum of the peak shown in A. The mass of the principal peak (13164 Da) corresponds to the molecular weight of the native protein. Peak

with 13208 Da (mass shift of 44 Da) suggests the formation of an adduct of the miniprotein, possibly generated under the conditions used during the LC-MS analysis.

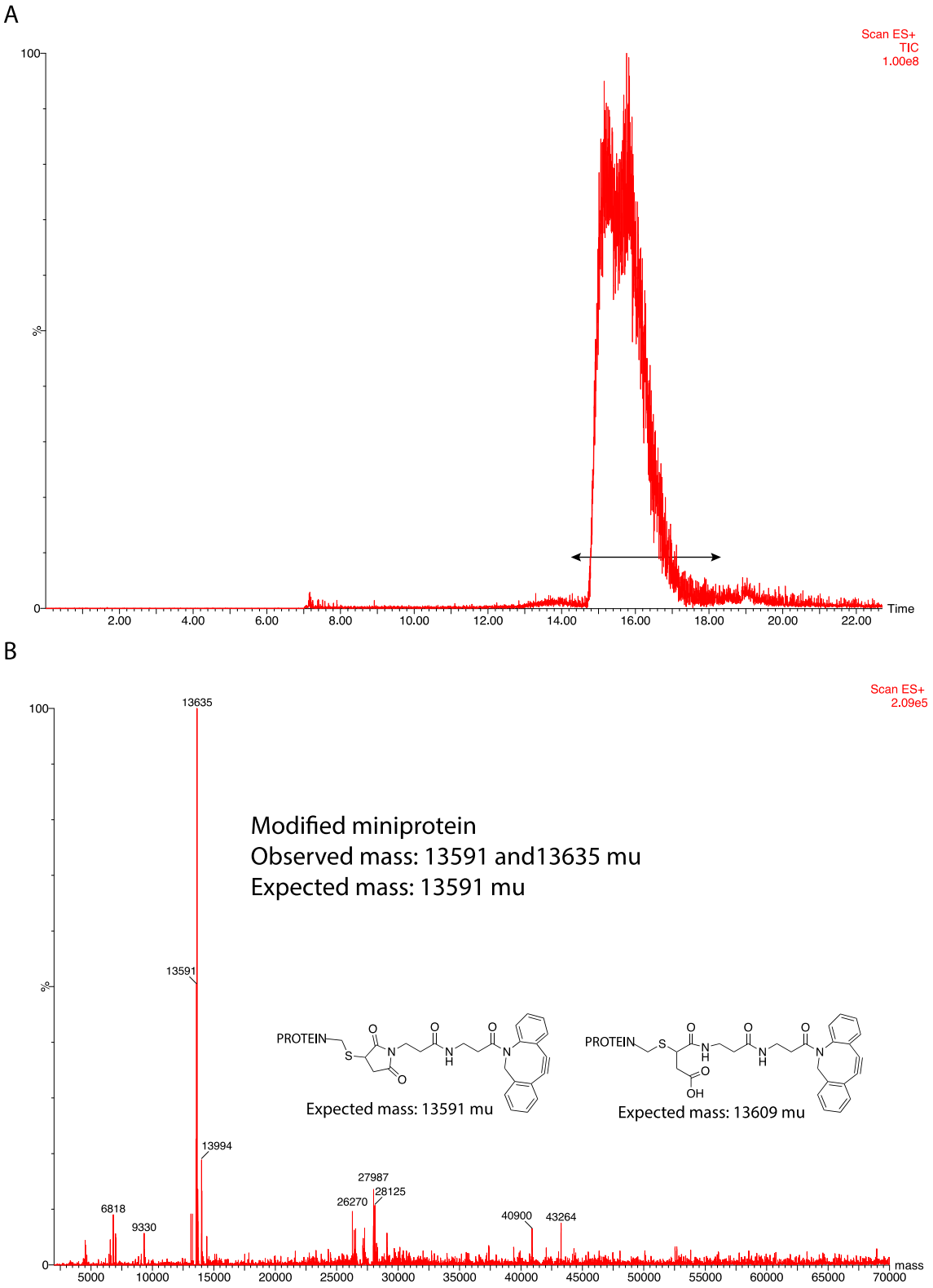

Figure 24 – ESI-MS analysis after protein conjugation with the Mal DBCO linker. A – Total ion ESI LC-MS chromatogram of the protein conjugated to Mal DBCO; B – Deconvoluted mass spectrum of the peak shown in A. The peak with 13591 mass units corresponds to the molecular weight of the miniprotein conjugated to Mal DBCO (13164 Da from native protein + 427.5 Da from

Mal DBCO). The main peak at 13635 mass units (+44 Da) was attributed to the formation of an unidentified adduct, likely resulting from the conditions used during the LC-MS analysis. Minor species (less than ~15% of the total signal) were also observed.

Comparing the mass spectra of the native (**Figure 23 – B)** and conjugated miniprotein (**Figure 24 – B**) it is observed that the expected and observed masses are in accordance, confirming the conjugation of the Mal DBCO linker to the miniprotein (+427.5 mass units). Additionally, absence of the peak corresponding to the native miniprotein (molecular weight 13164 Da) further supports the modification with the DBCO handle, as indicated by the formation of a peak with the expected mass of 13591 Da. However, the appearance of a main peak with 13635 Da, reflecting a mass shift of 44 Da, may suggest the formation of an unknown adduct. In fact, sequential analyses of both the native and conjugated miniproteins consistently revealed peaks with mass increases of +44 Da, with varying intensities across the analyses. Thiosuccinimide hydrolysis leading to the formation of an opened maleimide (expected mass: 13609 Da) combined with oxidation of the two methionines residues present in the structure (addition of +16, +32, or +48 Da) is also a possible explanation for the differences between the expected and observed masses [123]. Further detailed characterization of the adducts formed, using high-resolution ESI-Q-TOF and MS/MS analysis of tryptic digests, is still required. The modified miniprotein was subsequently purified through Amicon filtration, and its concentration was determined using the Qubit method, as described in section 2.4. Starting from a concentration of 4.5 mg/mL of native miniprotein (200 uLs), the conjugated protein with the DBCO handle was obtained with a concentration of 3.5 mg/mL (210 uLs) after purification.

3.1.2 Conjugation of miniprotein with the gold complex

After successful modification with Mal DBCO, the miniprotein was conjugated with a gold complex containing two azide groups via a copper-free DBCO-azide click reaction (**Figure 25**).

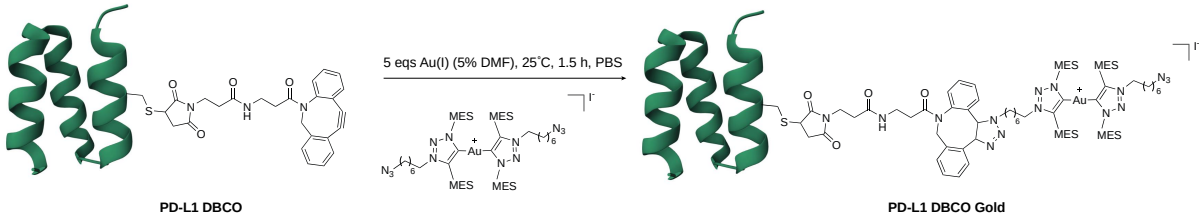

Figure 25 – Conjugation of the N_3-Gold complex to the DBCO miniprotein.

The reaction was conducted with 5 equivalents of the gold complex at 25 ºC for 1.5 h.

ESI LC-MS analysis confirmed the conjugation with full consumption of the starting miniprotein, as shown in **Figure 26**.

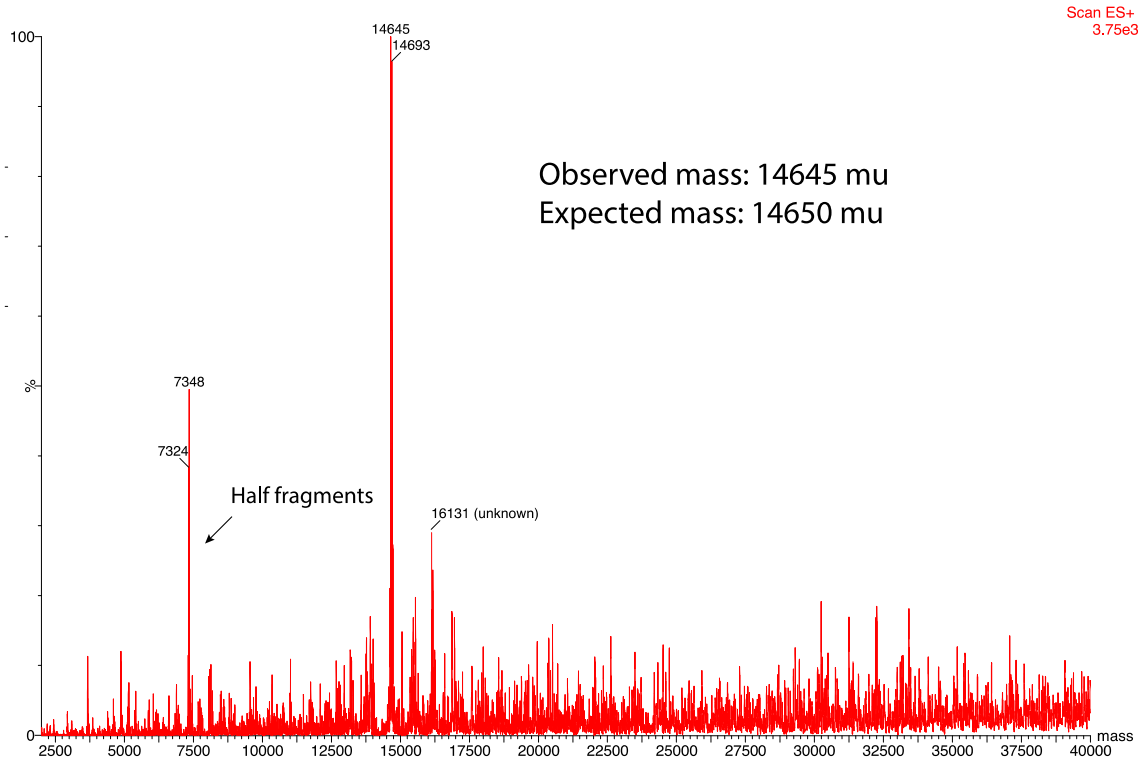

Figure 26 – ESI-MS analysis of the conjugate PD-L1 DBCO Gold. Deconvoluted mass spectrum showing conjugation of the N_3-Gold complex to the "PD-L1 DBCO miniprotein" (13591 Da from PD-L1 DBCO + 1059 Da from N_3-Gold complex).

The mass spectrum (**Figure 26**) shows a peak corresponding to the protein conjugated to the N_3-Gold complex, confirming the formation of metalloprotein (Expected mass = 14650; Observed mass = 14645; within estimated error for single quadrupole mass detection). The formation of a peak with a mass shift of approximately 44 Da (14693 Da) from the expected mass of 14650 Da can be attributed to the presence of the previously mentioned adduct. Additionally, the absence of peaks for the "DBCO protein" (13591 Da) indicates full conversion to the product. The miniprotein was further purified, and the concentration determined following the same protocol as before (starting reaction concentration = 3.5 mg/mL, volume = 150 μLs; final concentration = 1.4 mg/mL, volume = 170 μLs).

3.2 Radiolabelling of the PD-L1 miniprotein

3.2.1 Conjugation with BCN-NODAGA Chelator

To prepare the miniprotein for radiolabelling, a NODAGA chelator containing a strained alkyne (BCN-NODAGA) was conjugated to the miniprotein, for subsequent stabilization of the radioactive metal, gallium-67 (^{67}Ga) (**Figure 27**). Indeed, the NODAGA chelator provides an optimal conformation for coordinating ^{67}Ga, facilitating effective radiolabelling with high yield at low temperatures (37 ºC). This bioorthogonal and modular strategy enables the creation of miniprotein conjugates for both therapeutic and diagnostic applications.

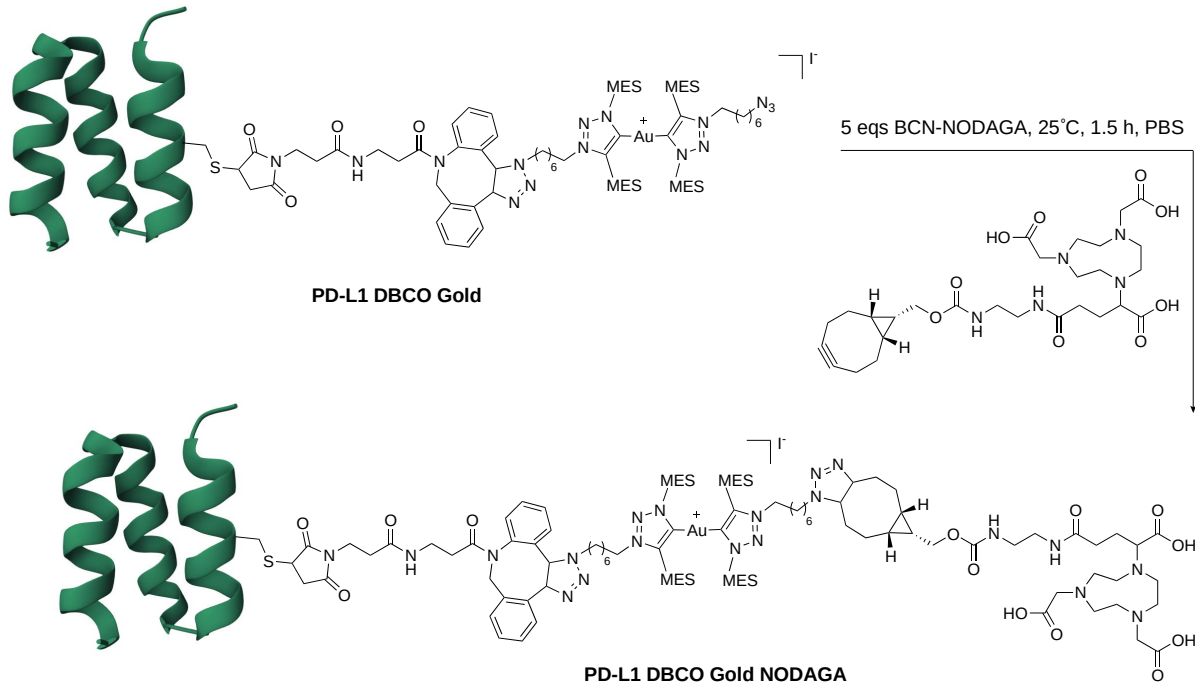

Figure 27 – Conjugation reaction of BCN-NODAGA to the miniprotein PD-L1 DBCO Gold.

The reaction was carried out using 5 equivalents of the chelator dissolved in water and reaction times of 1 to 2 h at 25 ºC. LC-MS analysis confirmed the conjugation, showing the complete consumption of the PD-L1 miniprotein bearing the N_3-Gold complex (PD-L1 DBCO Gold) (**Figure 28**).

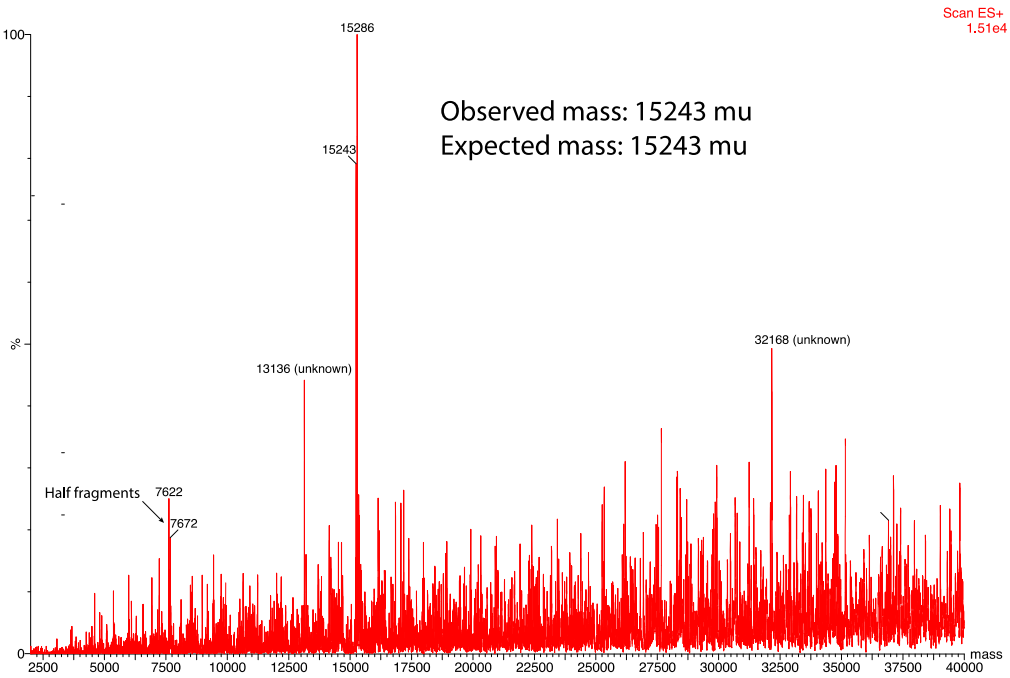

Figure 28 – ESI-MS analysis of the conjugate PD-L1 DBCO Gold NODAGA. Deconvoluted mass spectrum showing the formation of the "metallominiprotein" conjugated to the NODAGA chelator (14650 Da from PD-L1 DBCO Gold + 593 Da from BCN-NODAGA chelator).

The mass spectrum showed peaks corresponding to the conjugated miniprotein bearing the BCN-NODAGA chelator. In specific, the peak at 15243 Da corresponds to the expected mass, while a second peak at 15286 Da indicates the presence of a +44 Da adduct on the miniprotein. Additionally, the formation of two unidentified peaks with 13136 Da and 32168 Da was also observed. Given that the ionization efficiency for the metallominiprotein could be significantly reduced, the intensity of these peaks (31% and 33% relative to the PD-L1 DBCO Gold NODAGA conjugate) may not accurately represent the actual proportion of these species in terms of mass yield [124], [125]. This being said, the final conjugate was thoroughly purified by Amicon (8 washes) and its concentration quantified by Qubit (starting reaction concentration = 1.4 mg/mL, volume = 100 μLs; final concentration = 1.8 mg/mL, volume = 60 μLs, ~118 μM). The "NODAGA PD-L1 conjugate" proceeded for next studies to test the radiolabelling conditions with the radionuclide Gallium-67.

3.2.2 Labelling with Gallium-67

The NODAGA macrocyclic chelator is suitable for radiolabelling the protein with the isotope ^{67}Ga, facilitating subsequent studies on cell uptake and *in vivo* biodistribution in both cellular and tumor-bearing mouse models. The preparation of ^{67}Ga and the subsequent radiolabelling of the protein are detailed in section 2.4.6. The process involved first the transformation of ^{67}Gallium citrate to ^{67}Gallium chloride ([^{67}Ga]$GaCl_3$) using the specified procedure described in the Methods [118]. After obtaining the [^{67}Ga]$GaCl_3$ complex, the solution was mixed with 0.1 M sodium acetate solution to adjust the pH to 5 (1 part of ^{67}Ga and 3 parts of buffer). For radiolabelling the miniprotein, the PD-L1 DBCO Gold NODAGA conjugate (20 and 60 μM in PBS) was added to [^{67}Ga]$GaCl_3$ (1:1 mixture, 30 – 80 μCi) and let to react for 20 minutes to 1 hour at 37 ºC. The progress of the radiolabelling reaction was monitored using iTLC-SG. The iTLC analysis of the [^{67}Ga]$GaCl_3$ complex, using a solvent system of 99% methanol (MeOH) and 1% 6M hydrochloric acid (HCl), confirmed the radiochemical purity of the precursor, indicating that it was obtained without colloidal impurities (**Figure 29**). In this system, the separation of [^{67}Ga]$GaCl_3$ from colloidal species is achieved due to the differing affinities of the compound for the stationary and mobile phases. In the **Figure 29**, the gallium chloride precursor migrates with a Rf of 0.73, and no colloids are present at the origin (Rf=0).

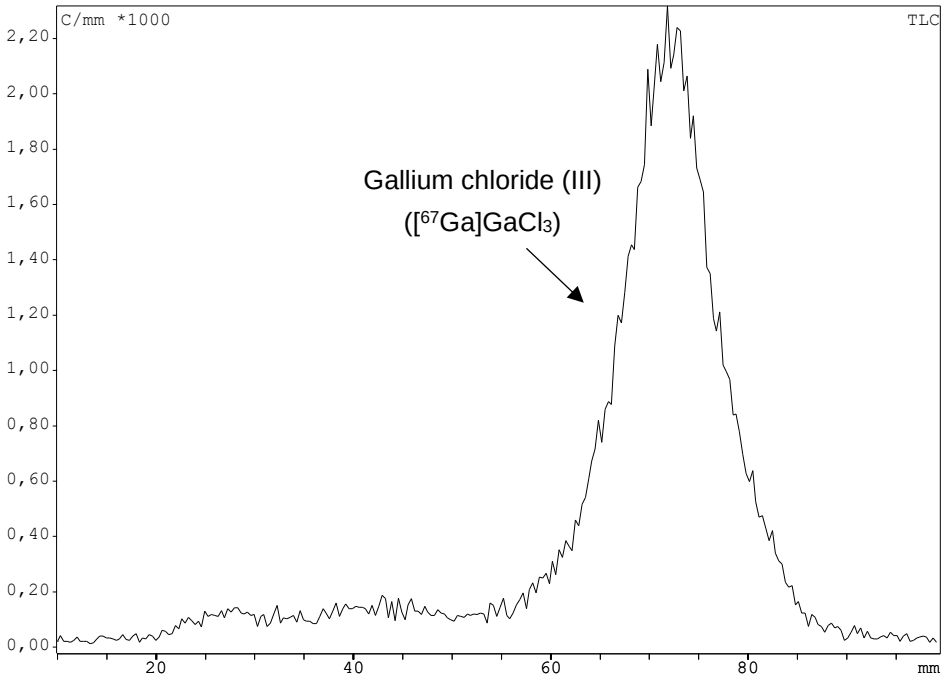

Figure 29 – iTLC-SG radiochromatogram after conversion of gallium citrate in gallium chloride (III) ([^{67}Ga]$GaCl_3$), using as mobile phase 99% of MeOH and 1% HCl 6M.

After reacting the protein with [^{67}Ga]$GaCl_3$ for 30 minutes at 37 ºC with agitation, the reaction yield was assessed using iTLC. The mobile phase used for this analysis was the same as previously described.

During the iTLC analysis, it was observed that the labeled protein appeared near the origin, while the free [^{67}Ga]$GaCl_3$ migrated as expected, with a Rf of 0.75 – 0.80. The reaction yield was 90% using a concentration of 30 μM of the protein conjugated to NODAGA. The use of lower concentrations of protein using the same radiolabelling conditions, namely 10 μM of "PD-L1 NODAGA", 30 min, 37 ºC and 0.1 M sodium acetate pH 5, resulted in poor radiochemical yields (~60% conversion). **Figure 30** illustrates the iTLC of the radiolabeled protein after purification via centrifugation using an Amicon filter with a 3000 Da cut-off. In this case, the labeled protein appears near the origin with a Rf value of 0.25 and a radiochemical purity of 95%. The free gallium chloride complex, which was not entirely removed during purification, is presented at 5% at the solvent front.

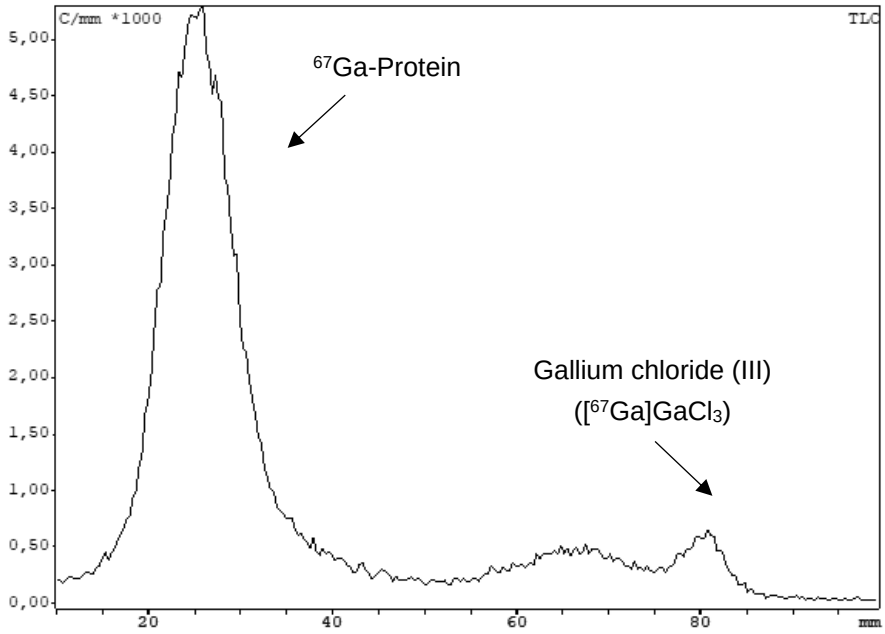

Figure 30 – iTLC-SG radiochromatogram of the reaction of the protein with [^{67}Ga]$GaCl_3$ during 30 min, 37 ºC at a final concentration of the miniprotein of 30 μM in 0.1 M sodium acetate. Chromatogram shown is after purification with Amicon. Mobile phase used was 99% of MeOH and 1% HCl 6M.

Compared to literature results, the PD-L1 miniprotein bearing the NODAGA chelator was labeled at concentrations considered acceptable for radiolabelling. For instance, in a study by the group of Nick Devoogdt, a PD-L1 nanobody modified with a maleimide NODAGA linker was successfully radiolabeled with gallium at a final concentration of 3.6 μM, after incubation for 15 minutes at 50 °C [107].

Occasionally, when the protein remains in solution for extended periods, there is a risk that the metal may decoordinate. However, the protein was labeled with a 95% conversion efficiency, and after 12 h at 37 ºC, the conversion remained > 88%, as shown in **Figure 31**. This confirms that the metal remains specifically coordinated to the protein via the conjugated chelator, demonstrating the successful synthesis of the “PD-L1 Gold metallodrug” bearing a NODAGA moiety for radiolabelling.

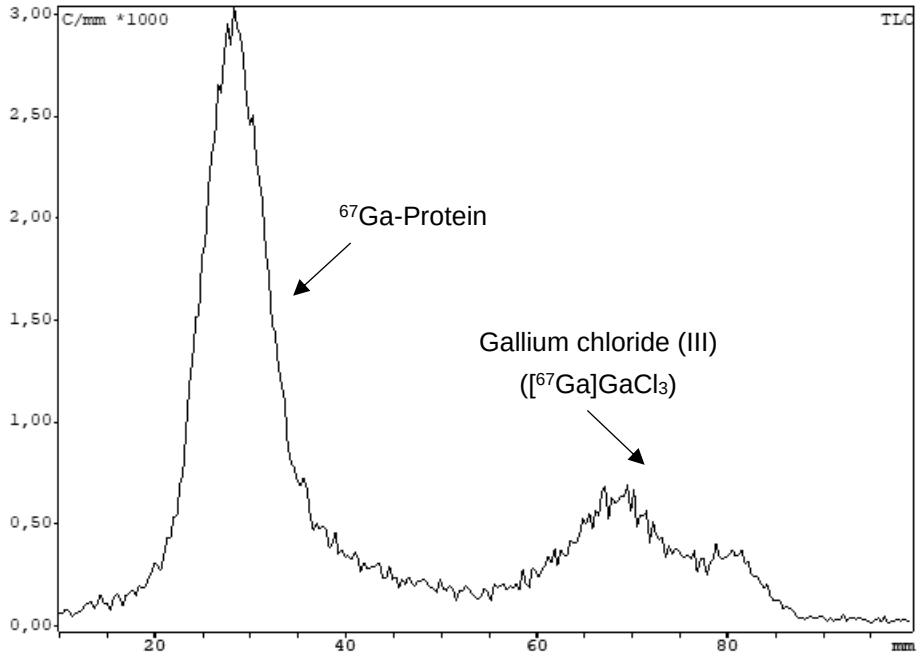

Figure 31 – iTLC-SG radiochromatogram of the radiolabeled protein with [^{67}Ga]GaCl$_3$ after 12 h at 37 ºC. Mobile phase 99% of MeOH and 1% HCl 6M.

To verify these results, the labeled protein was also analysed using HPLC with a radiodetector. The radio-HPLC results are represented in **Figure 32**. Results from the radio-chromatogram are in accordance with the iTLC results, confirming the radiolabelling of the miniprotein with [^{67}Ga]GaCl$_3$.

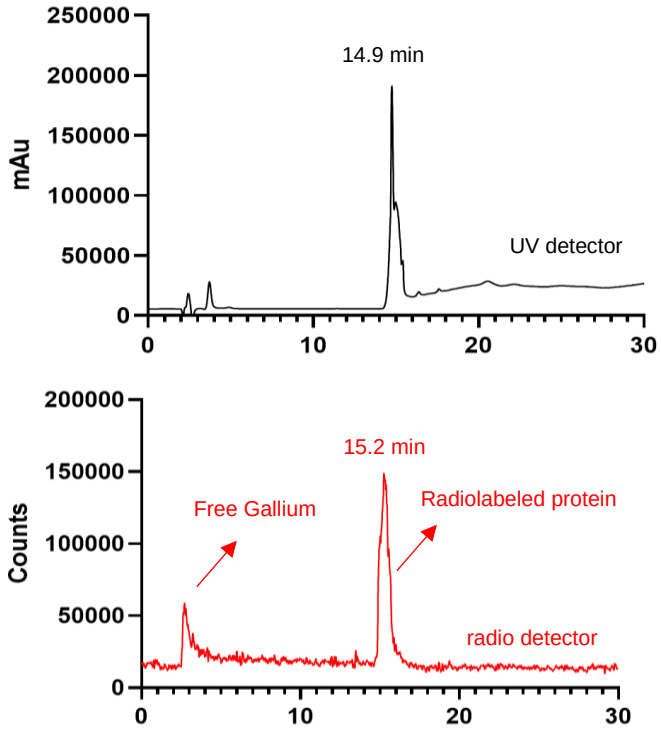

Figure 32 – HPLC Chromatograms of the radiolabeled protein with [^{67}Ga]$GaCl_3$. Top – UV detector chromatogram; Bottom – radio detector chromatogram. The HPLC was performed using a mobile phase consisting of 90% water in trifluoroacetic acid (TFA) and 10% acetonitrile in TFA, with a gradient run over 30 minutes, as detailed in the experimental procedures (Section 2.4.7). The small difference in the retention time in the UV- and radio-chromatograms (14.9 and 15.2 mins) is due to the sequential installation of both detectors.

It is important to mention that preliminary radiolabelling studies with a batch of PD-L1 DBCO Gold NODAGA, purified with only 3 washes using an Amicon filter, instead of the 8 washes applied in the optimized protocol, resulted in a radiochromatogram showing 3 distinct peaks (**Figure 33**). It was hypothesized that these peaks corresponded to free BCN-NODAGA, free NODAGA (arising from hydrolysis of the conjugation linker), and a small amount of the radiolabeled protein. Radiolabelling of BCN-NODAGA and free NODAGA for comparison of their retention times confirmed that additional purification steps are necessary to completely remove residual BCN-NODAGA. Therefore, it is critical to purify the “PD-L1 NODAGA protein” at least 8 times before radiolabelling to ensure higher yields and complete radiolabelling, free from NODAGA contaminants.

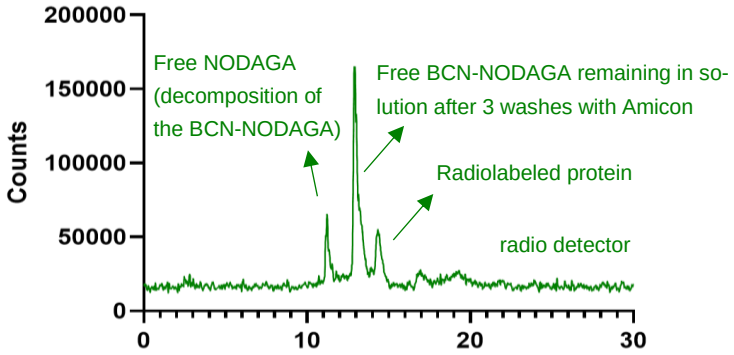

Figure 33 – HPLC chromatogram of the radiolabelling of the protein PD-L1 DBCO Gold NODAGA purified with Amicon only 3 times, instead of 8 times in the optimized conditions.

Overall, the protein labeled with ^{67}Ga was isolated with satisfactory purity (90%), allowing for an evaluation of its cellular uptake using the A20 cell line.

3.2.3 Cellular uptake

To evaluate the ability of the ^{67}Ga-radiolabeled miniprotein to recognize the PD-L1 protein in cancer cells, the A20 cell model, which expresses PD-L1, was used. The cells were incubated with the radiolabeled miniprotein under three different conditions: (1) with the radiolabeled miniprotein at 37 ºC, (2) with the unlabeled miniprotein blocking the PD-L1 receptors before adding the radiolabeled miniprotein at 37 ºC, and (3) with the radiolabeled miniprotein at 25 ºC. For all conditions, cells were incubated for various time points (5, 15, 30, 60, 120 and 180 minutes), after which the radioactivity associated with the cells was measured using a Hidex gamma counter. Cellular uptake is presented as the total activity percentage per mg of protein at each time point (**Figure 34**). Details of the experimental procedure are described in section 2.7.1.

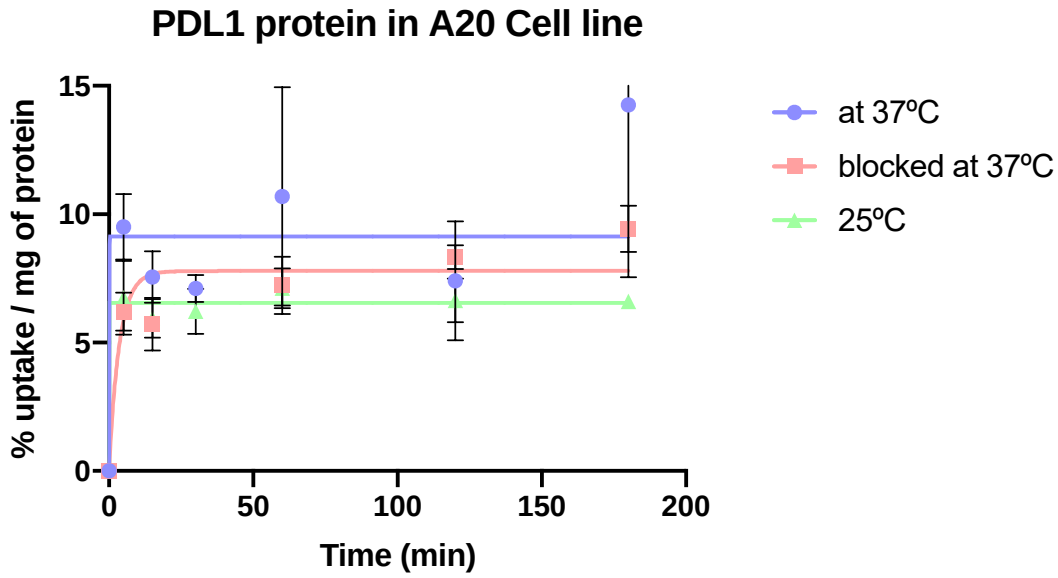

Figure 34 – Cellular uptake of the radiolabeled protein with ^{67}Ga in the A20 cell line. The values of cellular uptake are expressed as percentage of total activity added to normalized cells divided by mg of protein ± standard deviation (n=3 to each point of time). Solid curves are fitting results from Graph Prism (one phase association) for observed experimental data.

Comparison of the cell uptake of the radiolabeled miniprotein alone (purple circles) with the uptake following pre-incubation with unlabeled miniprotein (10 μM) to block PD-L1 receptors (pink squares) does not yield definitive conclusions about specificity for PD-L1 binding. While there is a trend towards a reduced uptake in the blocking studies with A20 cells (pink squares), which overexpress PD-L1 (unpublished data from the Radiopharmaceutical Sciences Group, confirmed by Western Blot), the differences remain within the error bars, making it difficult to draw final conclusions. Further studies with longer incubation times, higher blocking concentrations and additional cell lines, both with and without PD-L1 expression, are still needed to confirm specificity. On the other hand, uptake studies performed at 37 ºC (purple circles) and 25 ºC (green triangles) indicate that cell uptake increases with temperature, suggesting that the radiolabeled miniprotein may have active binding mechanism that promotes increased internalization over time.

The high cellular uptake observed in the A20 cells exceeded previously observed values, typically below 4% uptake/mg of protein, seen in cancer cell lines with other miniprotein probes tested in the Radiopharmaceutical Sciences Group. This result warranted further investigation of the *in vivo* biodistribution of the PD-L1 protein using a mouse model.

3.3 Biological evaluation of the gold-based protein conjugates

3.3.1 Cell viability assay

Viability studies were conducted in 96-well plates in section 2.7.1 to assess the impact of the highly cytotoxic gold complex used in this study on A20 and MC38 cell lines. Preliminary experiments demonstrated that the gold complex does not interfere with background fluorescence, as the fluorescence measured in wells without cells and containing PBS was identical to that in wells without cells but containing the gold complex.

The gold complex alone exhibited significant cytotoxicity even at low concentrations, resulting in an Inhibitory Concentration 50% (IC_{50}) of 0.78 μM (95% confidence interval (CI), 0.61 to 0.99 μM) in the A20 cell line (**Figure 35 – A**) and an IC_{50} of 0.35 μM (95% CI, 0.30 to 0.42 μM) in the MC38 cell line (**Figure 35 – B**).

A

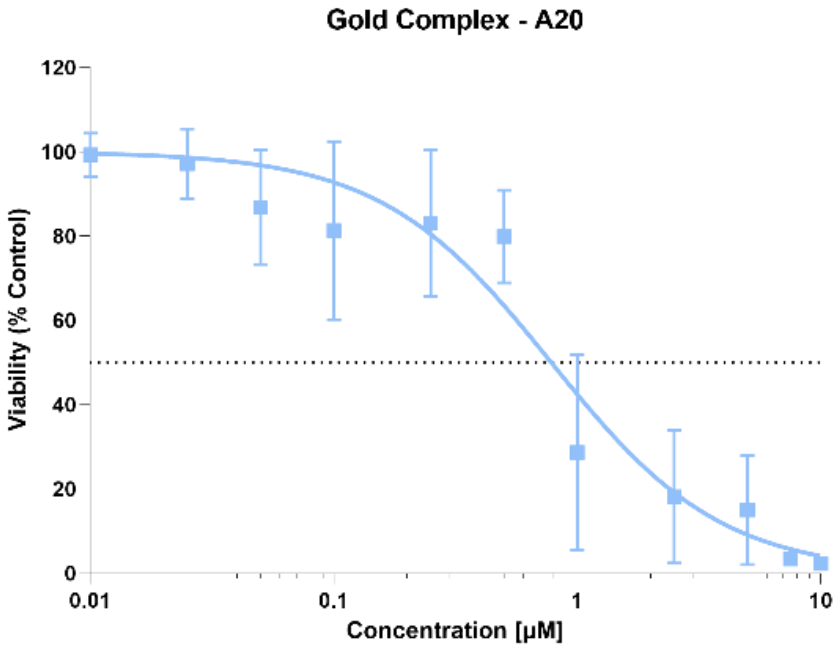

B

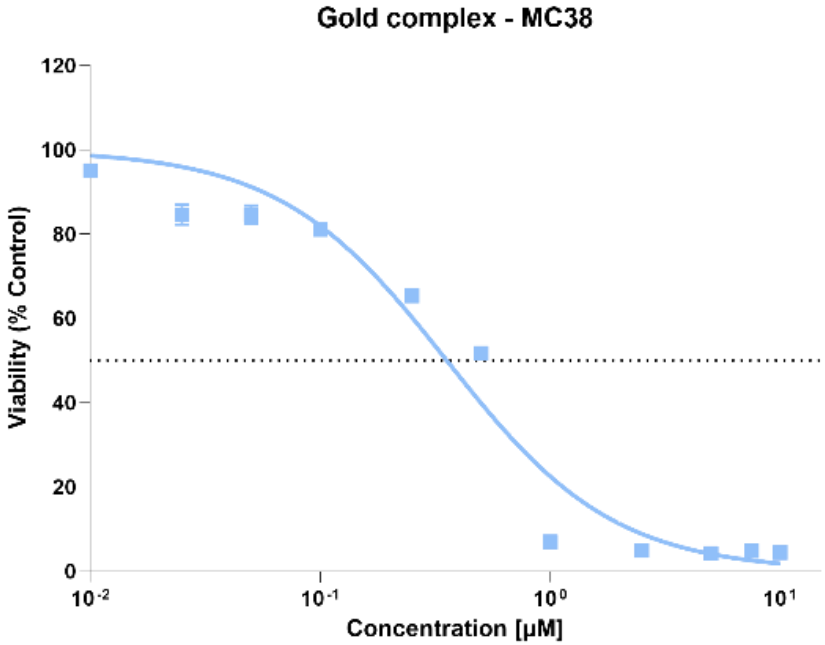

Figure 35 – Cellular viability of the N_3-Gold complex in A20 (A) and MC38 (B) cell lines. Results from two different experiments (3 wells for each concentration).

The toxicity of the gold complex when conjugated to the miniprotein was also evaluated in both cell lines, using a concentration range between 0.01 µM and 10 µM. For the A20 cell line, the IC_{50} was 0.35 µM (95% CI, 0.33 to 0.37 µM) (**Figure 36 – A**), and for the MC38 cell line, the IC_{50} was 0.33 µM (95%

CI, 0.31 to 0.37 µM) (**Figure 36 – B**). Overall, the gold complex alone or conjugated to a protein carrier shows similar toxicity towards cancer cell lines.

A

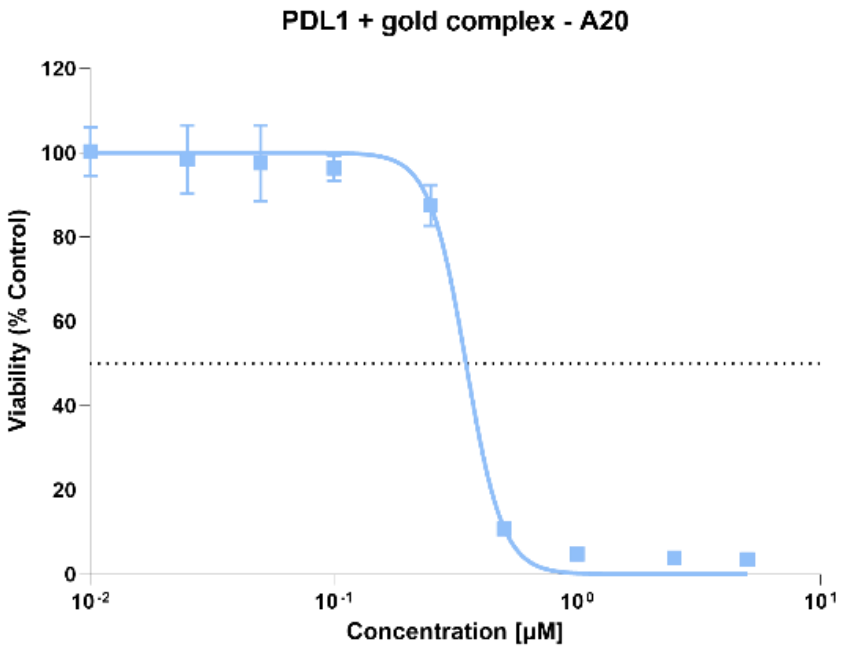

B

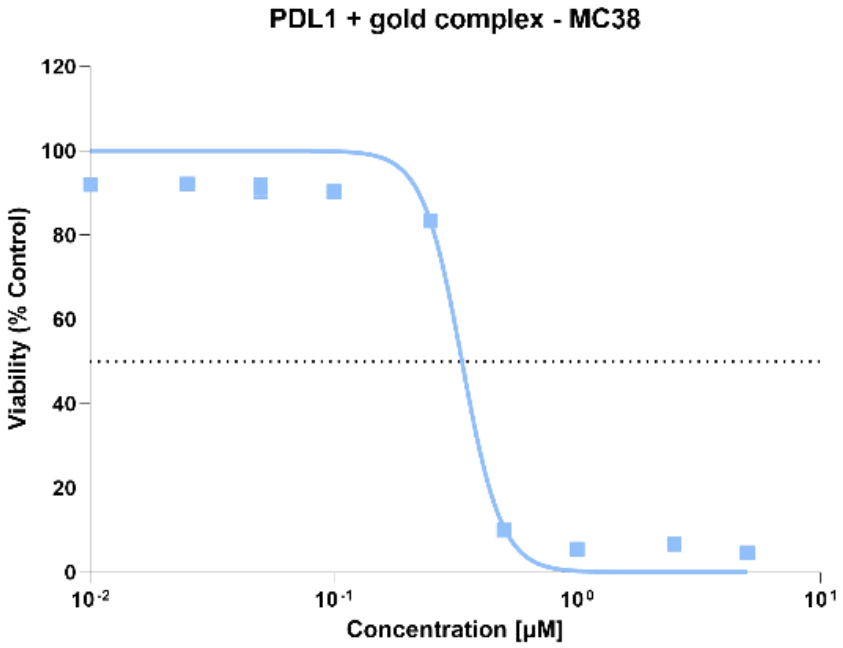

Figure 36 – Cellular viability of the miniprotein conjugated to the gold complex with cell line A20 (A) and MC38 (B). Results from two different experiments (3 wells for each concentration).

3.3.2 Biodistribution

The miniprotein demonstrated promising results in cellular uptake studies, prompting further evaluation of its *in vivo* biodistribution when radiolabeled with ^{67}Ga, as detailed in section 2.7.2. For this analysis, various organs, along with blood and urine samples, were examined at 1 hour and 4 h post-injection (p.i.) of the radiolabeled compound. The percentages of injected activity per gram of organ are presented in **Table 7** and **Figure 37**.

The biodistribution data of the ^{67}Ga-radiolabeled miniprotein in A20 tumor-bearing mice, as outlined in **Table 7** and **Figure 37**, reveal important insights into its *in vivo* behavior. Blood activity although decreased from 14.19 ± 1.64 % IA/g at 1 h to 7.49 ± 2.18 % I.A./g at 4 h, indicates some persistence in circulation overtime. On the other side, tumor uptake was 2.01 ± 0.38 % I.A./g at 1 hour and increased to 2.71 ± 0.64 % I.A./g at 4 h, demonstrating sustained and even enhanced retention over time. Importantly, a similar PD-L1 miniprotein conjugated directly with a maleimide-NODAGA linker for labelling with [^{67}Ga]$GaCl_3$ (similar sequence without HIS tag; confidential work) showed a similar tumor uptake of 2.45 ± 0.72 I.A./g. This suggests an effective tumor targeting observed for the PD-L1 prepared using the bioorthogonal approach herein applied.

Nevertheless, a high liver retention, with values rising from 21.55 ± 2.25 % I.A./g at 1 h and 29.79 ± 1.28 % I.A./g at 4 h *versus* 8.55 ± 1.55 % I.A./g at 1 hour and 7.02 ± 1.31 % I.A./g at 4 h for the directed labeled PD-L1 miniprotein (**Table 7**, confidential), raises concerns about potential hepatotoxicity, particularly for therapeutic applications.

Importantly, kidney activity was lower (7.60 ± 1.14 % I.A./g at 1 hour and 4.86 ± 0.10 % I.A./g at 4 h, **Table 7**) when comparing with the directly labeled ^{67}Ga-PD-L1 miniprotein (140.35 ± 20.24 % I.A./g at 4 h), suggesting a better profile in terms of renal reabsorption. The overall excretion increased from 17.0 ± 1.6 % I.A. at 1 h to 22.3 ± 0.4 % I.A. at 4 h (**Table 7**), indicating a more efficient clearance over time. Overall, it is crucial to further investigate the biodistribution profile of the PD-L1 DBCO Gold NODAGA miniprotein labeled with ^{67}Ga to determine whether the probe continues to clear from non-target organs while maintaining or increasing accumulation in the tumor.

In conclusion, the ^{67}Ga-radiolabeled miniprotein shows a biodistribution profile marked with some blood persistence, renal excretion, and promising tumor-targeting properties. However, high liver retention is present at 4h p.i. which may result in hepatotoxicity, especially for therapeutic applications. The observed decline in blood activity over time suggests that the ratio could become even more favorable at longer time points, improving tumor-specific targeting. Future studies should focus on studying the biodistribution profile at 24 h p.i. to see if accumulation in blood, liver, lungs and spleen keeps decreasing and conclude about the potential of the probe for both diagnostic and therapeutic applications in cancer treatment.

Additionally, establishing a correlation between the tumor uptake of the radiolabeled miniprotein and the expression levels of its target in tumor cells is also crucial for validating its specificity.

Table 7 – Percentage of activity of ^{67}Ga radiolabeled miniprotein after 1h and 4h of intravenous injection (100 µL, ~100 µCi) in BALB/c inoculated with A20 tumors (n = number of mice).

	% Injected activity (IA) / g of organ (n = 3)		
Probe	**Bioorthogonally labeled PD-L1 Gold metalloprotein**		**Directly labeled PD-L1 protein**
Time of sacrifice	**1h p.i.**	**4 h p.i.**	**4 h p.i.**
Blood	14.19 ± 1.64	7.49 ± 2.18	0.98 ± 0.27
Liver	21.55 ± 2.25	29.79 ± 1.28	7.02 ± 1.31
Intestine	1.88 ± 0.18	2.09 ± 0.29	1.17 ± 0.11
Spleen	5.79 ± 2.66	5.12 ± 0.26	3.59 ± 1.14
Heart	3.36 ± 1.00	2.25 ± 0.13	0.88 ± 0.20
Lungs	7.29 ± 2.68	4.17 ± 0.67	1.01 ± 0.17
Kidney	7.60 ± 1.14	4.86 ± 0.10	140.35 ± 20.24
Muscle	0.78 ± 0.28	0.81 ± 0.04	0.53 ± 0.10
Bone	2.07 ± 0.29	1.85 ± 0.20	2.19 ± 0.18
Stomach	1.60 ± 0.23	0.96 ± 0.26	1.13 ± 0.08
Pancreas	1.32 ± 0.21	0.97 ± 0.09	0.95 ± 0.24
Brain	0.52 ± 0.06	0.23 ± 0.02	0.03 ± 0.03
Tumor	2.01 ± 0.38	2.71 ± 0.64	2.45 ± 0.72
Excretion (% IA)	17.0 ± 1.6	22.3 ± 0.40	7.5 ± 0.8

A

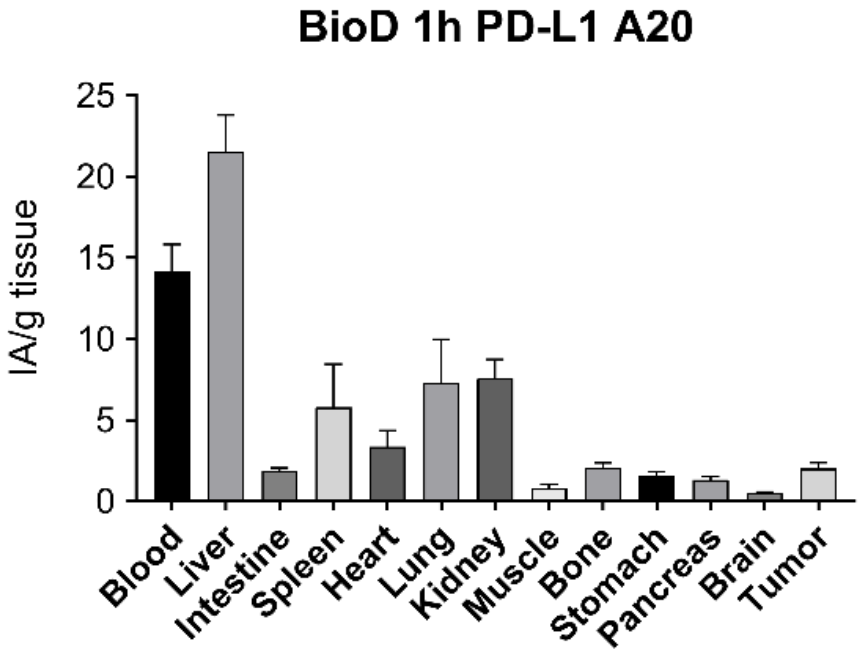

B

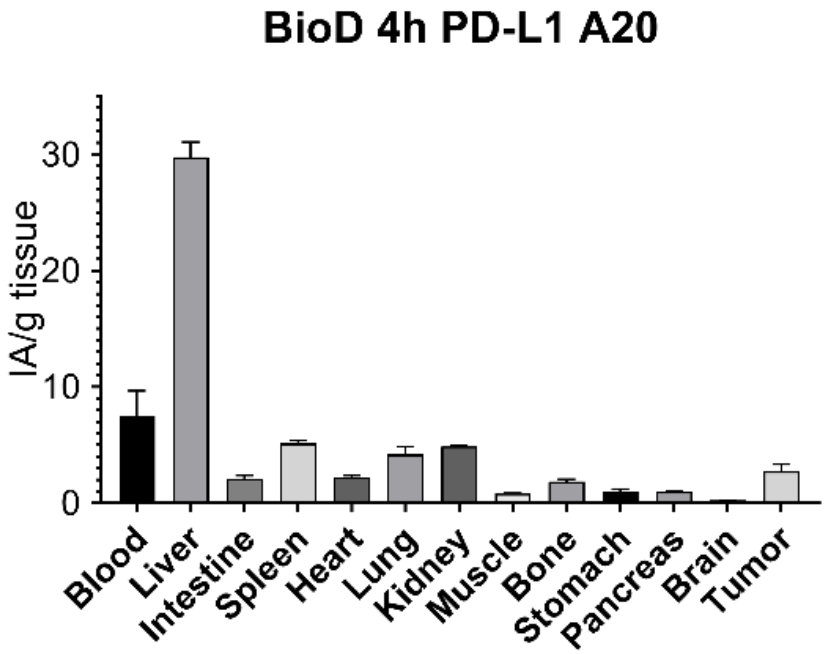

Figure 37 – Biodistribution studies for 1h and 4h after injection of the miniprotein radiolabeled with ^{67}Ga.

The stability and distribution of the radiolabeled miniprotein in blood were assessed at 1h and 4h post-injection using a Radio detector (**Figure 38**).

At 1h and 4 h post-injection, an single peak was observed, suggesting that the radiolabeled miniprotein was present in its intact form without decomplexation of ^{67}Ga, release of the chelator or degradation of the protein to more hydrophilic species. Overall, these results demonstrate that the radiolabeled miniprotein is relatively stable in the bloodstream during the first 4 h post-injection. This data supports the potential utility of the miniprotein for applications requiring extended circulation times.

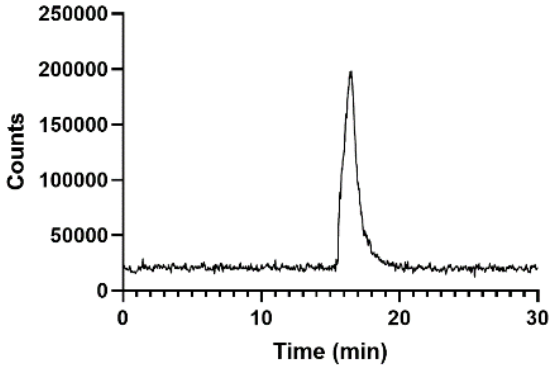

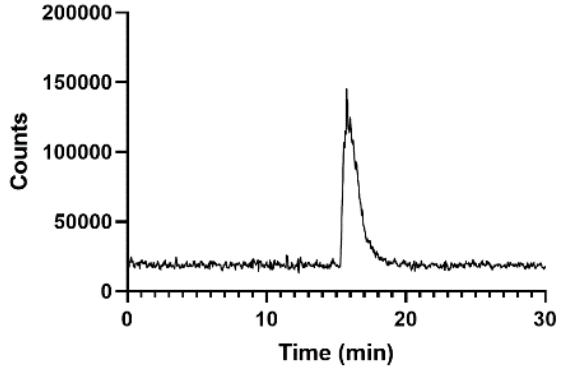

Figure 38 – RP-HPLC analysis of blood sample of the miniprotein stability after 1 (top) and 4 (bottom) h post-injection.

To assess the excretion and stability of the radiolabeled miniprotein, urine samples were also analysed at 1h and 4h post-injection (**Figure 39**). This analysis provides insights into the elimination pathway of the compound and its potential degradation over time.

Analysis of the radiochromatograms at 1h and 4h post-injection confirmed the presence of the intact radiolabeled compound also in the urine.

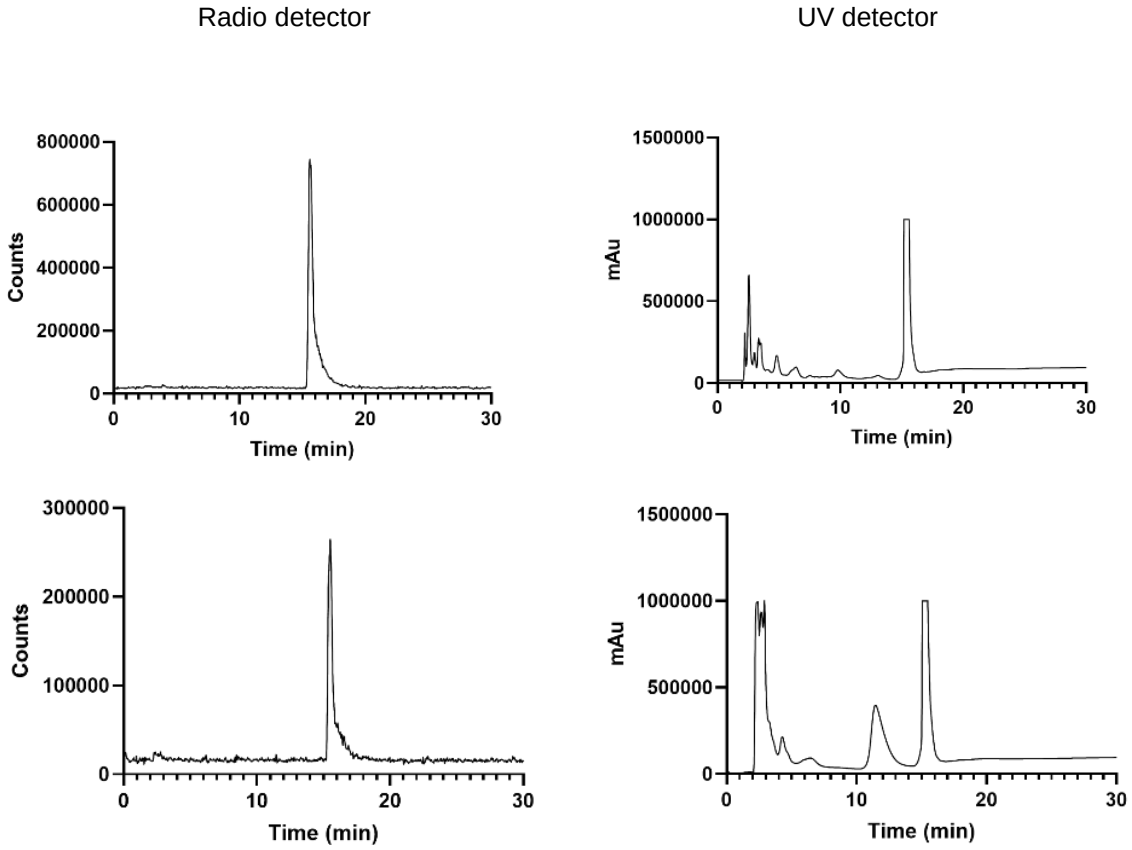

Figure 39 – RP-HPLC analysis of urine samples of the PD-L1 DBCO Gold NODAGA miniprotein labeled with ^{67}Ga after 1h and 4h post-injection.

In summary, radio RP-HPLC analyses of blood and urine samples indicate that the miniprotein remains stable in circulation without degradation for at least 4h p.i. and is excreted intact via the renal pathway (combined with a significant hepatobiliary component). Of importance, the detection of the miniprotein in the bloodstream even after 4h suggests a slower metabolism and prolonged circulation compared to the miniprotein labeled directly with the maleimide NODAGA chelator (at 4h p.i. no activity was observed in the blood for this probe). This difference in pharmacokinetics demonstrates the significant impact of conjugating the lipophilic gold complex with the clickable maleimide DBCO and BCN-NODAGA chelator on the *in vivo* profile of the miniprotein. Despite these changes, the radiolabeled ^{67}Ga-metalloprotein still exhibits a significant tumor accumulation, with high stability *in vivo*, demonstrating potential to be further explored in therapeutic or diagnostic applications.

3.4 Synthesis of an ADC

Building on the successful synthesis of the SPDC, which demonstrated effective targeting and therapeutic potential using a multifunctional miniprotein, we extended our approach to the development of an ADC. While SPDCs offer several advantages, including smaller size and faster tissue penetration, ADCs are designed to exploit the high specificity and affinity of antibodies for targeting cancer cells or other diseased tissues.

To synthesize the ADC, a similar two-step conjugation process to that used for the SPDC was employed. This process involved the attachment of a maleimide-based linker to the antibody, followed by conjugation with the cytotoxic gold complex.

The following sections detail the synthesis of the ADC, including the conjugation conditions and subsequent characterization using techniques such as LC-MS and HPLC to verify conjugation efficiency, product purity and stability.

In this study, two antibodies were synthesized for the development of ADCs. The first, Atezolizumab, which targets PD-L1 (the primary focus of this research), was used to ensure the ADC specifically binds to PD-L1-expressing cancer cells. Bevacizumab, targeting VEGF, is described in detail in Supplementary Material (Section A) and was primarily used to optimize the reaction conditions for ADC synthesis, ensuring robust protocols applicable to various ADCs. By employing two antibodies, we demonstrate the broader applicability of the described modular approach across a wider range of ADCs, emphasizing the versatility and reproducibility of the synthesis methods developed in this study.

3.4.1 Removal of excipients

According to the literature, it is essential to remove all the excipients present in Atezolizumab (Atezo) prior to conjugation to ensure optimal reaction conditions. To achieve this, a zeba desalting column was used, and the concentration of the antibody was measured before and after purification. The results showed that after using the Zeba column, the antibody concentration dropped around 4 times. While desalting effectively removed the excipients, it also caused a substantial loss of the antibody. To prevent

this issue, efforts were made to modify the antibody in the presence of the excipients L-histidine hydrochloride monohydrate, sucrose, and polysorbate 20.

3.4.2 Reduction of disulfide bridges´ reaction

Before proceeding with antibody conjugation, it was necessary to prepare the antibodies by reducing the disulfide bonds to generate free thiol groups. This step is crucial for enabling subsequent conjugation reactions. This was achieved using TCEP, a hydrosoluble reducing agent that is often used for conjugating cysteines with maleimides (**Figure 40**).

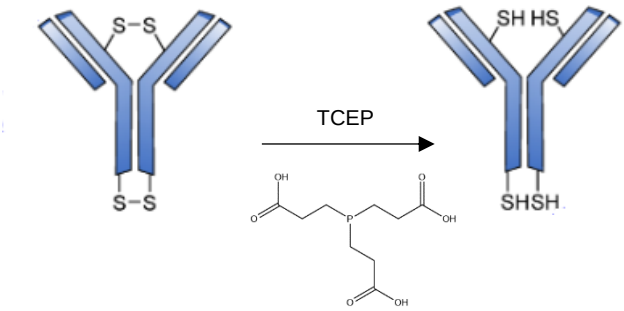

Figure 40 – Reaction of the reduction of disulfide bridges with TCEP

The reaction of the antibody with TCEP, conducted at 37 ºC with 20 equivalents of TCEP, was optimized using Bevacizumab and is described in detail in Section A.2.1.

3.4.3 Conjugation with Maleimide DBCO

After the reduction of the disulfide bonds, the thiol groups are free to react with the carbon-carbon double bond on the Mal DBCO reagent, already used to modify the miniprotein (**Figure 41**).

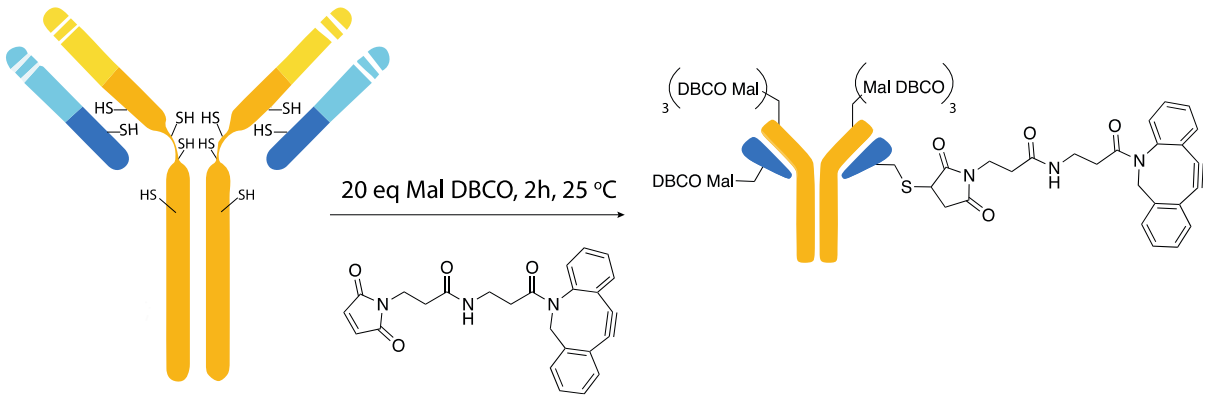

Figure 41 – Schematic scheme for the conjugation of Mal DBCO to the antibody Atezolizumab

The reaction was optimized considering several conditions (Section A.2.2). Conjugation with Mal DBCO was best performed with 20 equivalents of the reagent, reacting for 2 h at room temperature without purifying with a zeba column to remove excipients.

To confirm that the modification was fully successful, the antibody in its native state was characterized and compared with the conjugated form (**Figure 42**).

A

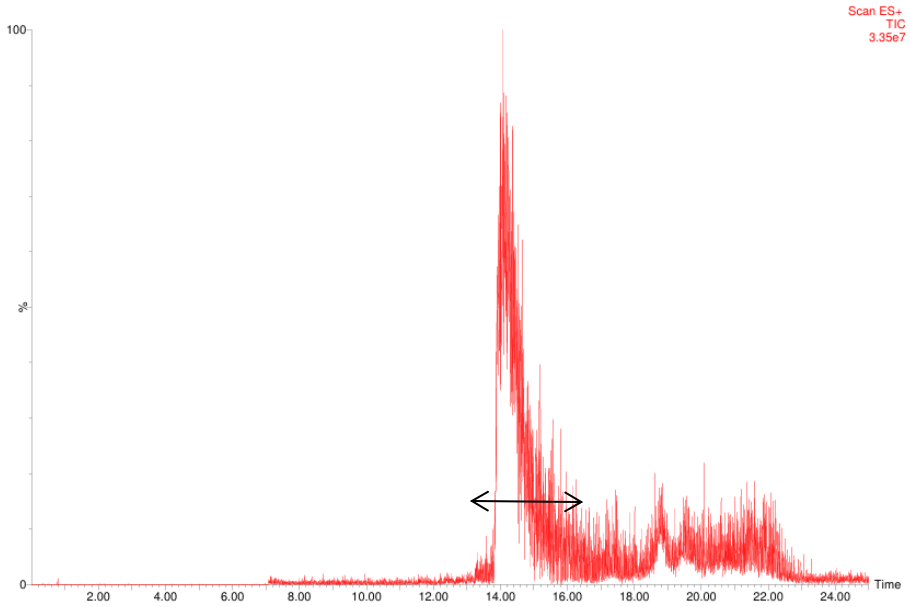

B

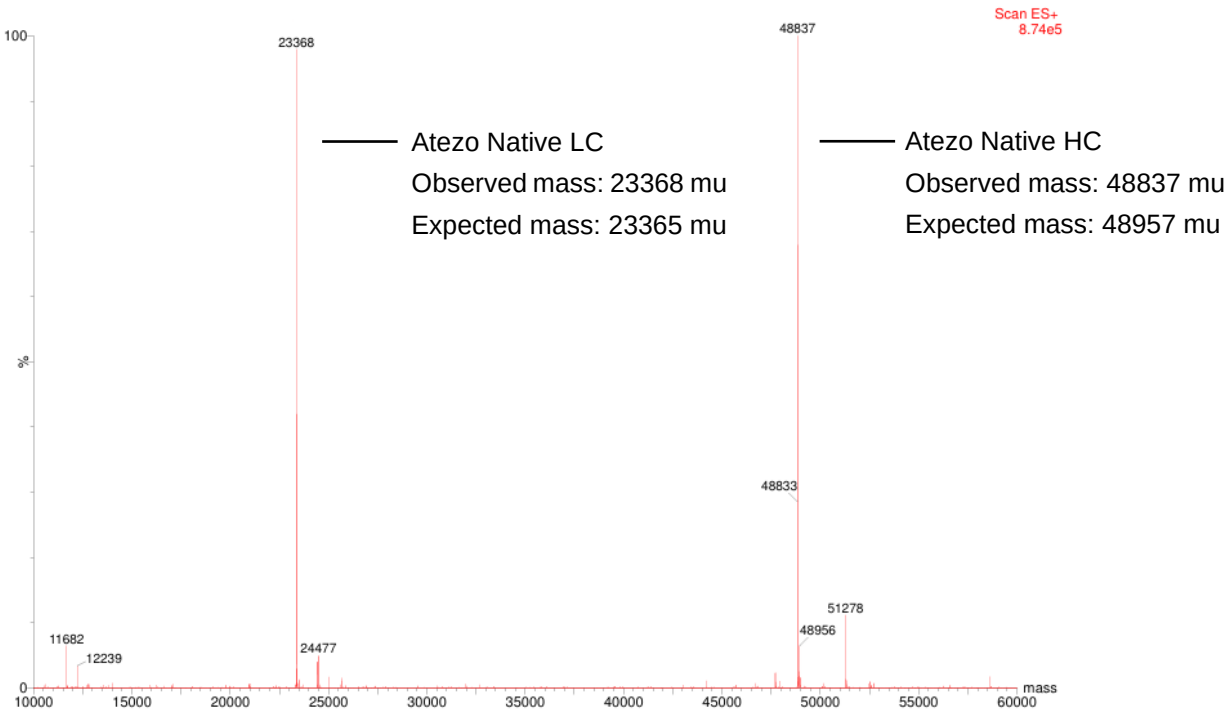

Figure 42 – ESI-MS analysis of the native antibody. A – Total ion ESI LC-MS chromatogram of the native antibody; B – Deconvoluted mass spectrum of the peak shown in A; Main peaks represent the expected molecular weight of the LC and HC, respectively of the native antibody. Sequence of Atezolizumab available at https://www.kegg.jp/entry/D10773 (accessed on 13-10-24)

A

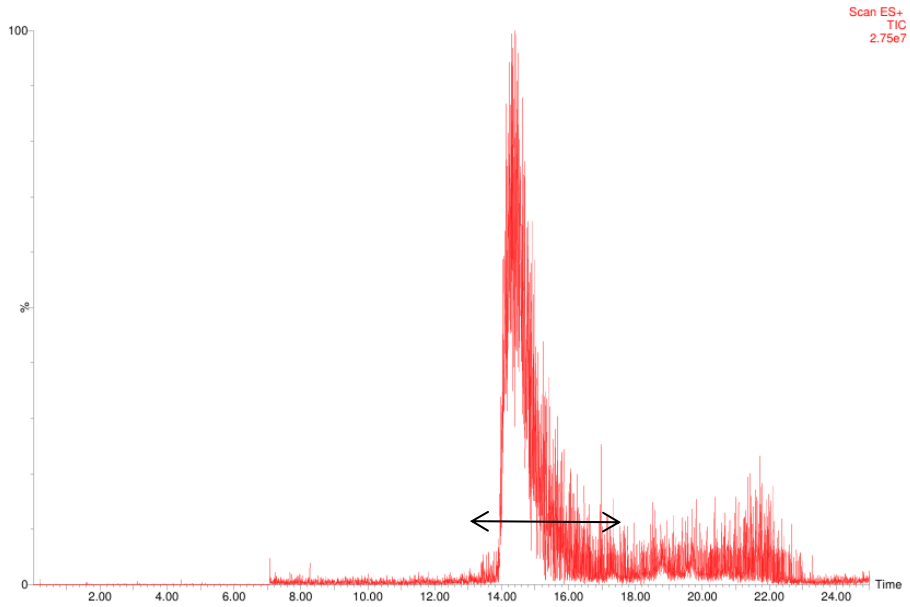

B

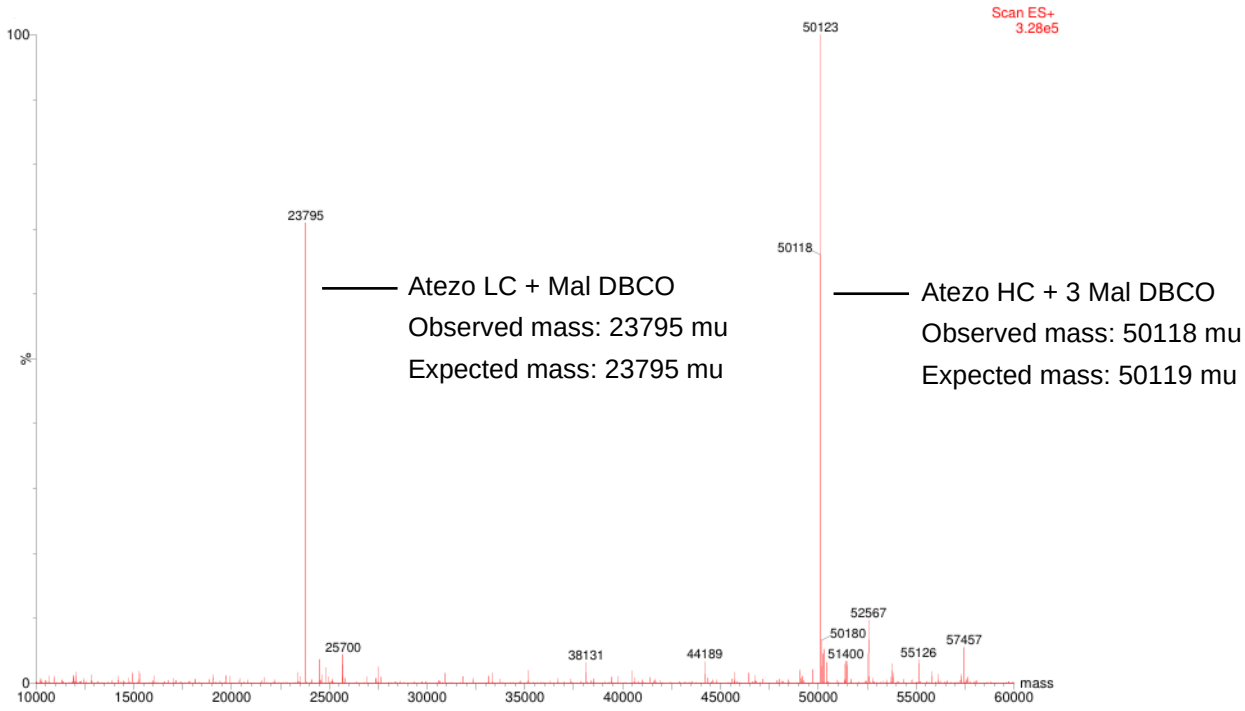

Figure 43 – Analysis of the conjugation of Mal DBCO to the antibody. A – Total ion ESI LC-MS chromatogram of the antibody conjugated with Mal DBCO; B – Deconvoluted mass spectrum of the peak shown in A; Main peaks represent the expected molecular weight of the LC and HC of the antibody conjugated to Mal DBCO (23368 Da of the LC + 427.5 Da from Mal DBCO; 48837 Da of the HC + 427.5 x 3 Da from conjugations of three Mal DBCO groups).

A comparison of the molecular weight of the native protein (**Figure 42 – B**) with the molecular weight of conjugated antibody (**Figure 43 – B**), reveals that the observed and expected masses of the LC and HC are in accordance, confirming that the conjugation was effective with complete reaction with Mal DBCO. In the deconvoluted mass spectrum of the conjugated antibody, no peaks corresponding to the molecular weight of the native antibody are observed (23368 Da for the light chain and 48837 Da for the heavy chain), demonstrating that all the native antibody was successfully modified. Importantly, the heavy chain of the modified antibody shows the presence of three Mal DBCO molecules. It is worth mentioning that Atezolizumab contains a total of 16 disulfide bridges (H22-H96, H145-H201, H221-L214, H227-H'227, H230-H'230, H262-H322, H368-H426, H'22-H'96, H'145-H'201, H'221-L'214, H'262-H'322, H'368-H'426, L23-L88, L134-L194, L'23-L'88, L'138-L'194; information retrieved from https://www.kegg.jp/entry/D10773, accessed on 13-10-24). Despite using an excess of reagent sometimes greater than 20 equivalents, only three disulfide bridges were consistently modified on the heavy chain. The modified antibody was subsequently purified through dialysis, and its concentration was determined using the Qubit method, as described in section 2.4. Starting from a concentration of 5.2 mg/mL of native antibody (200 uLs), the conjugated antibody with the DBCO handle was obtained with a concentration of 1.2 mg/mL (210 uLs) after purification.

3.4.4 Conjugation with gold complex

After successful modification with Mal DBCO, the antibody was conjugated with the gold complex (**Figure 44**).

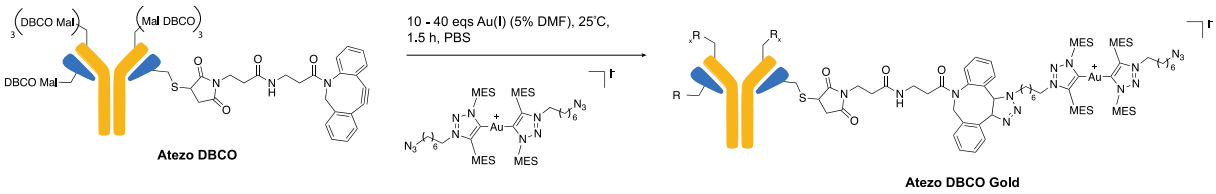

Figure 44 – Conjugation of the symmetric Au(I) bis-1,2,3-triazole-5-ylidene complex having two azides to the Atezo DBCO antibody.

For the conjugation of Atezolizumab with the gold complex, several conditions were optimized to account for reaction efficiency and minimize unwanted side effects, such as protein precipitation. Initial experiments were conducted using 40 equivalents of the gold complex to ensure complete conjugation (**Figure 45**, further details in Section A.2.3). However, during these tests, a significant amount of precipitate was observed, suggesting that this concentration of the reagent might be too high.

To address this issue, the reaction was repeated with a reduced amount of the gold complex, i.e. 10 equivalents. This adjustment resulted in less precipitation, improving the mass yield as accessed by Qubit. However, despite less precipitate being observed, the reaction was incomplete, as indicated by LC-MS analysis represented in **Table 8**. Using less equivalents full conjugation was not achieved, leaving some Atezo DBCO unmodified.

These findings highlight the importance of optimizing conditions to achieve a balance between less precipitation and complete conjugation. While using fewer equivalents reduced precipitation, it also lowered the overall efficiency of the reaction.

Table 8 – Modification of the LC and HC of Atezolizumab using 10 and 40 equivalents of gold complex

Gold equivalents	% of modification of LC	% of modification of HC
10	15	0
40	100	0

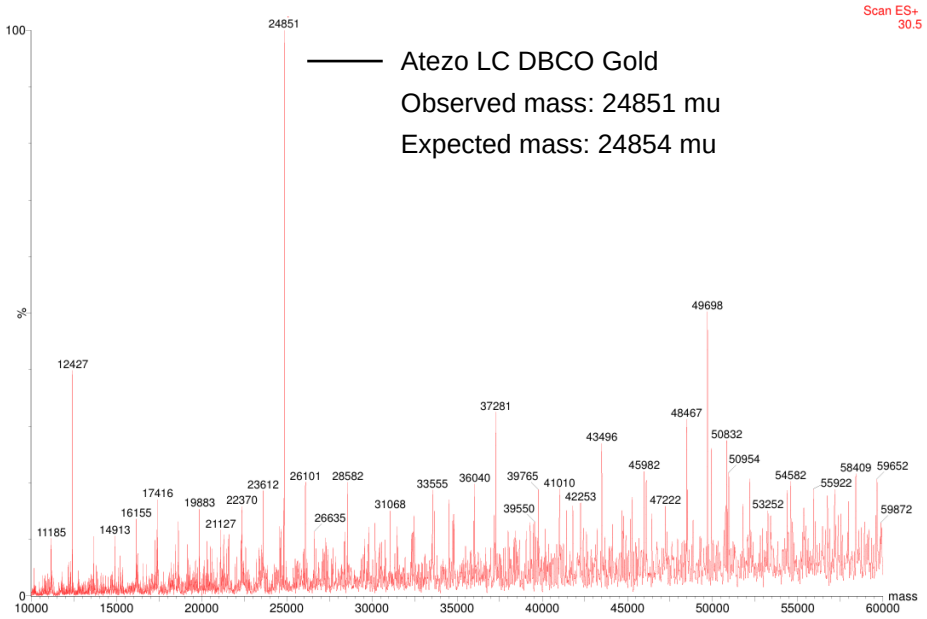

Figure 45 – ESI-MS analysis of the conjugate Atezo DBCO Gold. Deconvoluted mass spectrum showing conjugation of the N_3-Gold complex to the LC of "Atezo DBCO" (23795 Da from Atezo DBCO + 1059 Da from N_3-Gold complex). Modification of the HC of "Atezo DBCO" with the N_3-Gold complex was not observed in the ESI-MS spectrum (50119 Da from Atezo DBCO + 1059 x 3 Da from N_3-Gold complex = 53296 Da).

Overall, after reaction with 40 equivalents of the N_3-Gold complex, the light chain was fully converted as shown in **Figure 45**. However, detection of the heavy chain modified with the gold complex (expected mass: 53296 Da), or either the modified heavy chain with DBCO (50119 Da for Atezo DBCO) or the native heavy chain (48837 Da) was not observed in the ESI-MS spectrum. This could be related to the low ionization efficiency of the heavy chain after reacting with the gold complex, or potentially due to precipitation of the reacted heavy chain. The antibody modified with the N_3-Gold complex was purified, and its concentration was determined using the Qubit method, as described in section 2.4. Starting from a concentration of 1.2 mg/mL of the conjugated antibody with the DBCO handle (210 µLs), the conjugated antibody with the N_3-Gold complex was obtained with a concentration of 0.38 mg/mL (150 µLs) after purification.

3.4.5 Improve hydrophilicity of Atezolizumab

Starting with a concentration of 40 µM, the reaction between the antibody and the Mal DBCO reagent typically ended with a final concentration of around 10 µM. Following conjugation with the gold complex, the concentration decreased further, leading to low mass yields by mass. The hydrophilicity of the linker is crucial in designing ADCs; when both the payload and linker are hydrophobic, the resulting ADC may have a tendency to aggregate. To avoid these risks, improve reaction yields, and enhance stability of the modified antibody, we used a Mal DBCO reagent with a PEG linker (**Figure 46**). PEG linkers are known for their hydrophilic properties, which increase the overall solubility of the ADC [49].

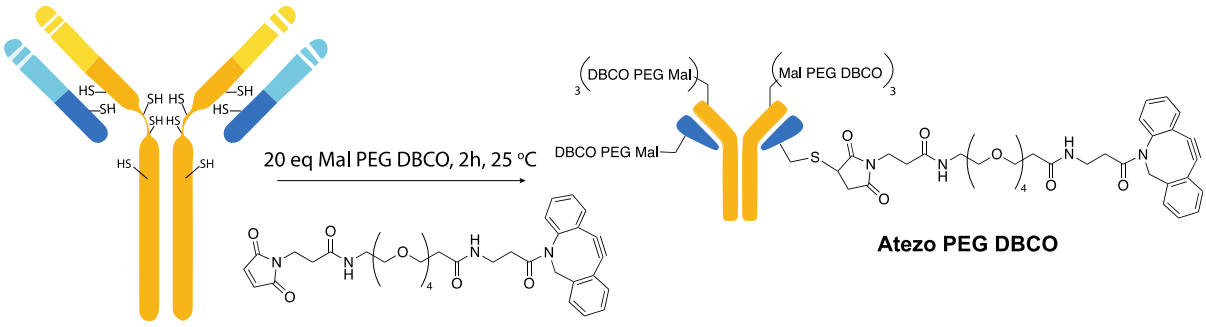

Figure 46 – Modification of the antibody with the maleimide PEG DBCO linker

To confirm that the modification was completed using the standard conditions previously described (20 equivalents, 2 h reaction at room temperature) the native antibody (**Figure 42 – B**) was compared with the modified version (**Figure 47 – B**).

A

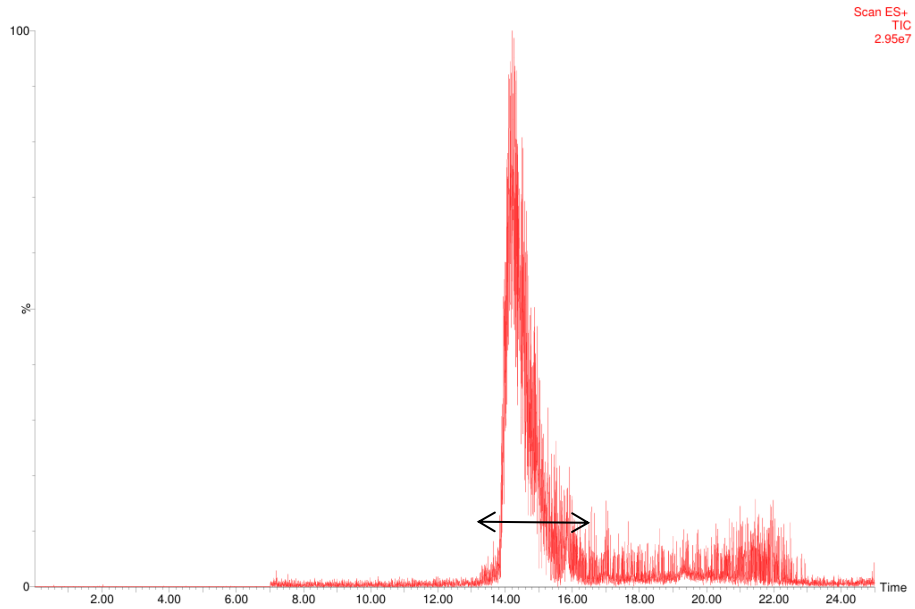

B

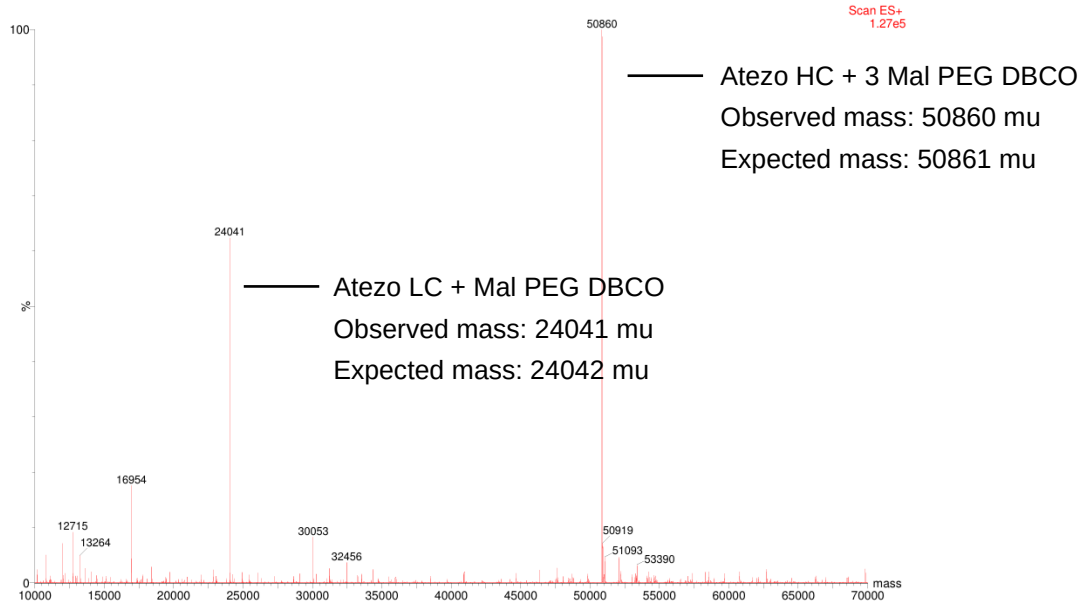

Figure 47 – Analysis of the conjugation of Mal PEG DBCO to the antibody. A – Total ion ESI LC-MS chromatogram of the antibody conjugated with Mal PEG DBCO; B – Deconvoluted mass spectrum of the peak shown in A; the main peaks represent the molecular weight of the LC and HC of the antibody conjugated to Mal PEG DBCO (23368 Da of the LC + 674,7 Da from Mal PEG DBCO; 48837 Da of the HC + 674,7 x 3 Da from conjugations of three Mal PEG DBCO groups).

The mass spectrum (**Figure 47 – B**) shows peaks corresponding to the antibody conjugated with Mal PEG DBCO. Of note, the HC was modified with three Mal PEG DBCO molecules, consistent with the results from the Mal DBCO reaction. The absence of peaks corresponding to the native antibody (23368 Da for the LC and 488837 Da for the HC) confirms that the reaction was completed.

The concentration of the antibody was determined by Qubit using the same protocol described for the miniprotein. Importantly, the concentration of the antibody conjugated with the PEG linker increased significantly, reaching 20 µM. This suggests that enhancing the hydrophilicity of the modified antibody improves the reaction yield to 50% by mass, doubling the yield observed for the Mal DBCO conjugate without the PEG linker. These results were thoroughly validated through triplicate experiments.

3.4.6 Conjugation of the Gold complex to Atezo modified with Mal PEG DBCO

After switching to a more hydrophilic linker, the conjugation reactions using 20 and 40 equivalents of the gold complex were repeated, as these conditions were the most promising with the Mal-DBCO linker. LC-MS analysis confirmed that both conditions resulted in the modification to the LC of the antibody. The absence of peaks corresponding to intermediates, or the native antibody suggests that the modification process was both efficient and completed (**Figure 48**). Based on these findings, 20

equivalents were selected for the reaction with the gold complex to minimize reagent consumption while preserving efficiency.

Compared to the results obtained with the Mal-DBCO linker, the hydrophilic linker significantly improved the solubility of the final product, as evidenced by reduced precipitation and aggregation in the reaction mixtures, as assessed by determination of the mass yields by Qubit (Section 2.4). Starting from a concentration of 2.8 mg/mL (150 µLs) of the conjugated antibody with the maleimide PEG DBCO, the conjugated antibody with the N_3 Gold complex was obtained with a concentration of 0.45 mg/mL (180 µLs) after purification. However, reaction of the heavy chain bearing the PEG DBCO group (50861 Da) with the gold complex (expected mass: 54038 Da) was not observed in the ESI-MS spectrum (**Figure 48**). This could be related with the low ionization efficiency of the heavy chain after reacting with the gold complex, or potentially due to precipitation of the reacted heavy chain, although this is unlikely.

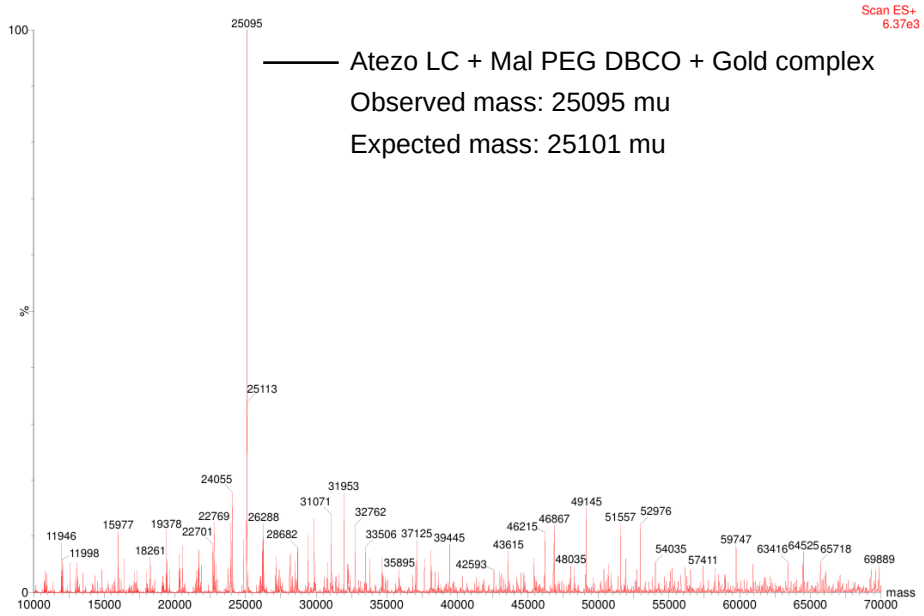

Figure 48 – ESI-MS analysis of the conjugation of the N_3-Gold complex to Atezo PEG DBCO. Deconvoluted mass spectrum showing conjugation of the N_3-Gold complex to the LC of "Atezo PEG DBCO" (24042 Da from Atezo PEG DBCO + 1059 Da from N_3-Gold complex). Modification of the HC of "Atezo PEG DBCO" with the N_3-Gold complex was not observed in the ESI-MS spectrum (50861 Da from Atezo DBCO + 1059 x 3 Da from N_3-Gold complex = 54038 Da).

3.4.7 Purification of the antibody between conjugation reactions

To ensure the success of the conjugations, the antibody was purified between steps using dialysis, as described in the experimental section (2.4.4). Initially, PBS at pH 7.4 was used as the dialysis buffer. However, this led to significant antibody precipitation, resulting in substantial antibody loss as assessed by Qubit quantification. To address this issue and improve antibody stability, a histidine buffer was chosen instead, as it is part of the formulation of Atezolizumab that was envisioned to help in the stabilization of the antibody.

Comparing the concentration of the conjugated antibody after dialysis with the two buffers, the histidine buffer demonstrated a marked improvement in stability. It effectively reduced precipitation and increased the final concentration of the antibody after reaction with the Gold complex from approximately 1 µM to 10 µM.

3.5 Fluorescent labelling of Atezolizumab

3.5.1 Conjugation with DBCO-Cy5

To enable fluorescence-based detection and imaging, the antibody was conjugated with the fluorescent dye DBCO Cy5 (**Figure 49**). This dye, which contains a DBCO functional group, enables the conjugation through bioorthogonal click chemistry with the free azide group on the gold complex. Conjugation of the fluorophore to the antibody Atezo PEG DBCO Gold was analysed by SDS-PAGE in-gel fluorescence.

Figure 49 – Schematic representation of the conjugation of DBCO Cy5 to the antibody Atezo PEG DBCO Gold

3.5.2 In-gel fluorescence imaging

To confirm that the antibody was fluorescent, an SDS-PAGE gel was run, followed by standard procedures for detecting the full antibody and its light and heavy chains. Fluorescence imaging was performed using an Amersham imaging system (**Figure 50**) together with Coomassie Blue staining for visible dye detection (**Figure 51**).

For the SDS-PAGE analysis, negative controls were included: well A contained the native (unmodified) antibody, while well B contained the native antibody subjected to the same reaction conditions as the conjugated antibody, but without the addition of the DBCO and gold complex. Well C contained the antibody modified with the maleimide PEG DBCO, gold complex and fluorophore dye. In-gel fluorescence imaging shows the presence of fluorescent bands corresponding to the LC, HC and full IgG as detected by SDS-PAGE that is consistent with the incorporation of Cy5 fluorophore in the antibody (**Figure 50**).

In the Coomassie Blue-stained gel (**Figure 51**), distinct bands were observed: at 25 kDa, corresponding to the LC, and at 60 kDa, corresponding to the HC. The top band at 150 kDa is assigned to the full IgG molecule; however, we cannot rule out the possibility of a dimeric IgG, which requires further confirmation.

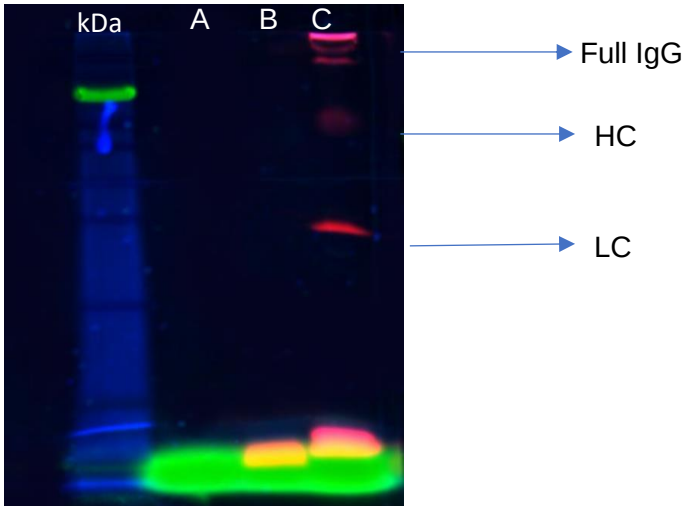

Figure 50 – The Amersham Image. The well A, B and C contain the same as the dye coomassie blue

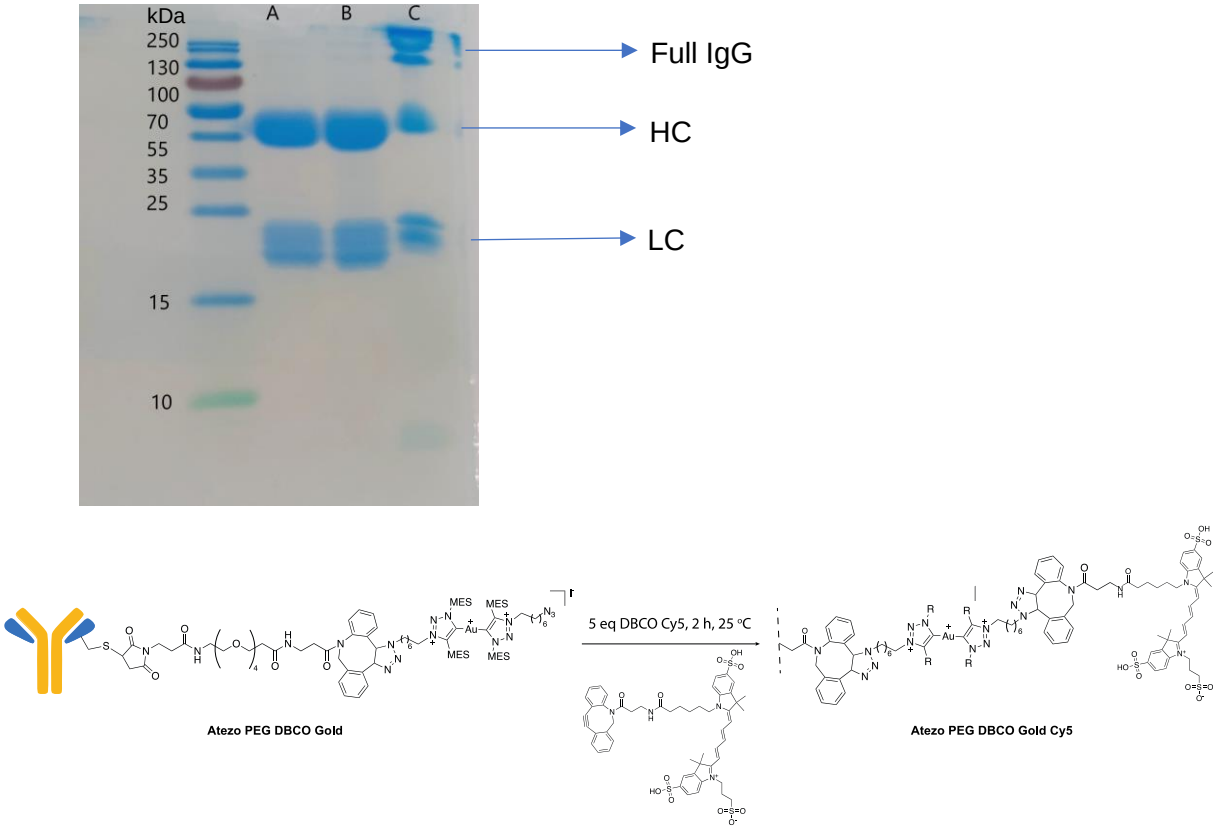

Figure 51 – The visible dye coomassie blue. Well A - native antibody; well B - Native antibody + fluorophore; Well C – Antibody modified with maleimide PEG DBCO, gold complex and fluorophore. Details can be found in section 2.7.2

3.5.3 *In vivo* imaging

After confirming the fluorescence of the antibody, we proceeded to *in vivo* studies using mice inoculated with the A20 tumor cell line, which is known to overexpress PD-L1, as reported in the literature

[126]. The aim was to determine whether the fluorescently labeled antibody accumulates in the tumor tissue.

In vivo fluorescence imaging acquired using a IVIS Lumina system was performed at four different time points (1, 6, 24, and 48 h post-injection) after injection of ~18 nM/kg of probe. During each imaging session, the mice were analysed for 5 seconds to capture the fluorescence signal. The **Figure 52** demonstrate that the accumulation of the labeled antibody in the tumor was highest at 6 h post-injection, with a significant fluorescence signal detected in all imaged animals injected with the probe (Mouse Green, Mouse Red and Mouse Blue) compared to the control.

The color scale used in the imaging ranged from brown (representing the lowest intensity) to yellow (representing the highest intensity), with corresponding values from $1{,}7 \times 10^{-4}$ to $6{,}00 \times 10^{-4}$ fluorescent units. The fluorescence signal showed a steady increase over time, indicating a gradual accumulation of the antibody within the tumor. This is consistent with the slow excretion and extended blood half-life of antibodies, which can range from 6 to 28 days *in vivo*. The control mouse, injected with the vehicle (PBS), displayed no autofluorescence in the tumor region across all time points, as seen in **Figure 52**.

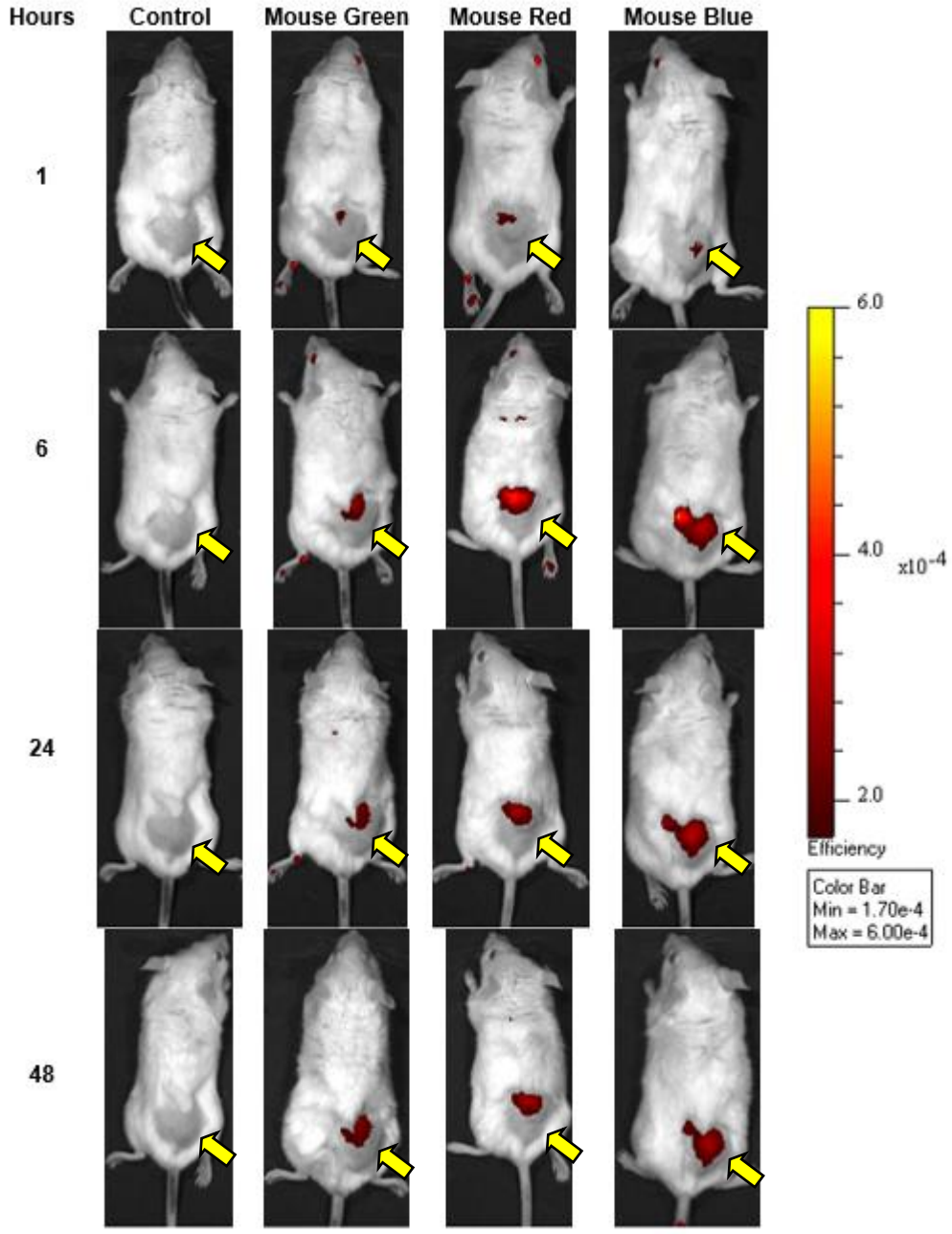

Figure 52 – Non-invasive *in vivo* imaging of Atezolizumab labeled with Cy5 in mice with A20 tumors (overexpressing PD-L1). Fluorescence images were taken at 1, 6, 24, and 48 h post-injection (18 nM/kg). The color scale on the right indicates fluorescence intensity from brown (lowest) to yellow (highest), with values from 1.70×10^{-4} to 6.00×10^{-4}. Tumor location are marked with arrows. The control mouse (injected with PBS) showed no fluorescence, confirming the specific accumulation of the labeled Atezolizumab in the tumor tissue.

3.6 Radiolabelling of Atezo PEG DBCO Gold

3.6.1 Conjugation with BCN-NODAGA chelator

To prepare the antibody for radiolabelling the BCN-NODAGA chelator was conjugated to the antibody for subsequent stabilization of the radioactive metal ^{67}Ga (**Figure 53**).

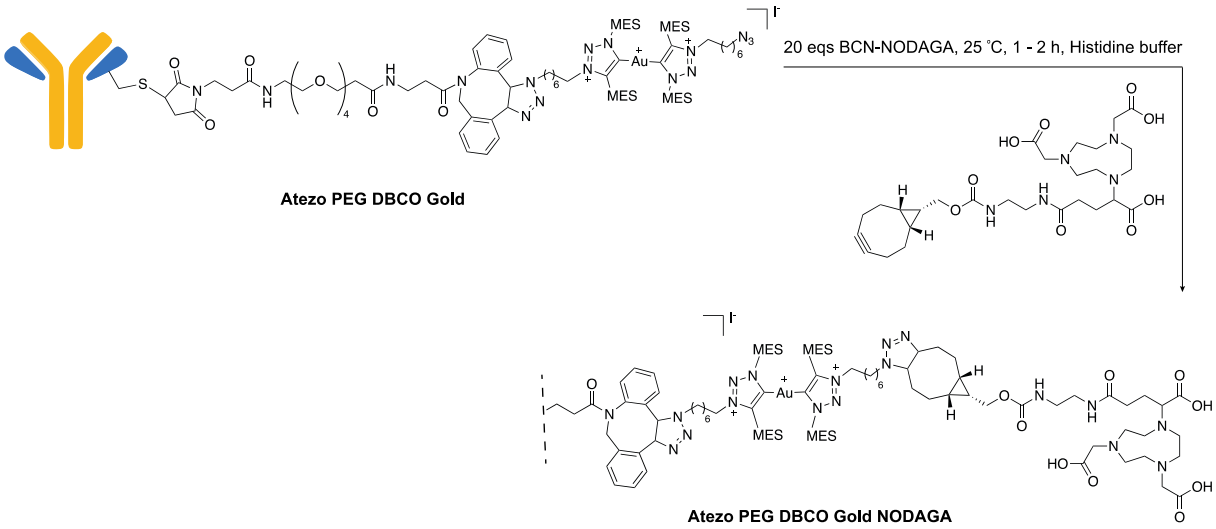

Figure 53 – Conjugation of BCN-NODAGA to Atezo PEG DBCO Gold

The reaction was carried out using 20 equivalents of the chelator at 25 ºC for 1 – 2 h. LC-MS analysis clearly showed that the starting protein was reacted i.e. Atezo PEG DBCO Gold (25101 Da) with a formation of a peak with 25689 Da (expected mass: 25694 Da) corresponding to modification of the light chain with the NODAGA chelator (**Figure 54**). As previously observed and discussed, modification of the heavy chain of "Atezo PEG DBCO Gold" with the chelator was not observed in the ESI-MS spectrum. Purification and quantification of the concentration (1,1 mg/mL, volume 100 µL) followed the standard protocol.

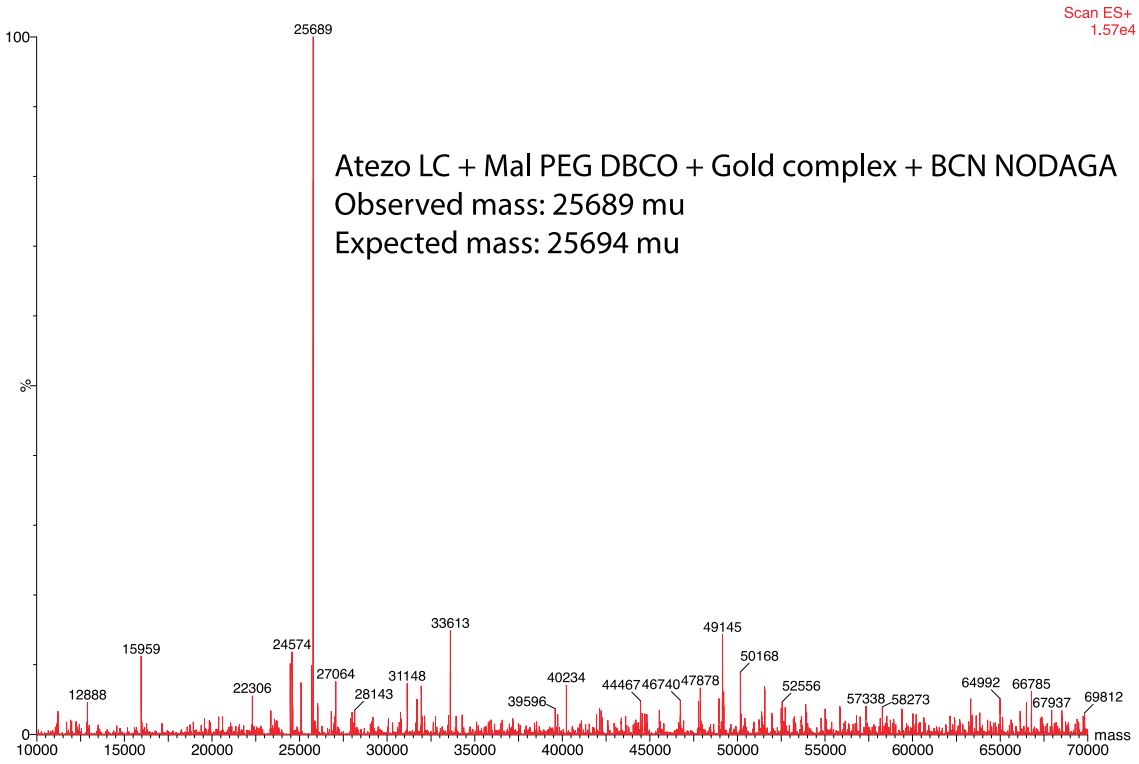

Figure 54 – ESI-MS analysis of the conjugation of BCN-NODAGA to Atezo PEG DBCO Gold. Deconvoluted mass spectrum showing conjugation of the chelator to the LC of "Atezo PEG DBCO Gold" (25101 Da from Atezo PEG DBCO Gold + 593 Da from

N_3-Gold complex). Modification of the HC of “Atezo PEG DBCO Gold” with the chelator was not observed in the ESI-MS spectrum (54038 Da from Atezo PEG DBCO Gold + 593 x 3 Da from BCN-NODAGA = 55817 Da).

3.6.2 Labelling with gallium-67

The radiolabelling conditions for the antibody are presented in section 2.4.6. In detail, the Atezo PEG DBCO Gold NODAGA conjugate (3 µM in Histidine buffer, pH 5.5) was incubated with [^{67}Ga]$GaCl_3$ (in a 1:1 ratio, 20 µCi in acetate buffer pH 5.0) for 1 hour at 37 °C, resulting in a final concentration of 1.5 µM and a total volume of 40 µL. Radiolabelling yields were assessed using iTLC, as shown in **Figure 55**. Similar to the miniprotein, the labeled antibody remained at the origin, while free [^{67}Ga]$GaCl_3$ migrated in the solvent front, as expected. The highest radiochemical yield for the NODAGA-conjugated antibody was 65% after 1 hour at 37 °C. Of relevance, extended incubation times did not further improve the radiolabelling yield. As a control, the same protocol was applied to label the native Atezolizumab antibody without being conjugated to NODAGA. iTLC analysis showed no significant labelling of the antibody with ^{67}Ga, which indicates that the radiometal was bound to Atezo through NODAGA chelation in the ADC prepared by click chemistry.

When compared to the PD-L1 miniprotein, it was concluded that the antibody could be labeled at a lower concentration under similar conditions, achieving a 65% radiochemical yield at 1.5 µM, compared to 60% at 10 µM for the miniprotein. Mass spectrometry analysis indicated that at least two NODAGA chelators were conjugated to the antibody (one for each light chain). Considering that the heavy chain is also expected to have 3 to 6 chelators, although not detected due to the limitations of the mass spectrometry method used, the final concentration of the chelator on both proteins is at the same range. Further attempts to produce the NODAGA-conjugated antibody at higher concentrations were unsuccessful due to protein precipitation, which hindered in vivo studies with the labeled atezolizumab.

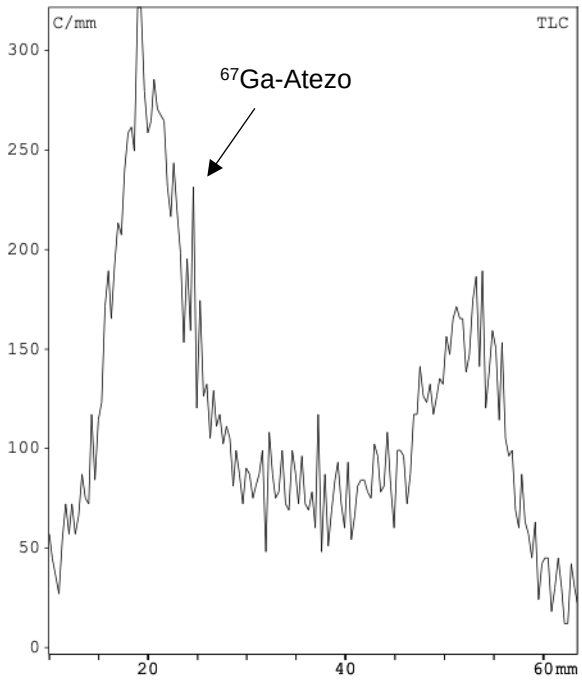

Figure 55 – iTLC-SG radiochromatogram for the radiolabelling of the NODAGA-conjugated atezolizumab with [^{67}Ga]$GaCl_3$ during 1 hour at 37 ºC at a final concentration of 1.5 μM.

4

CONCLUSIONS

The synthesis of a multifunctional miniprotein-based metallodrug was successfully achieved combining click chemistry with bioorthogonal reagents i.e. a maleimide DBCO linker for cysteine bioconjugation, a symmetric N_3-functionalized gold complex, and a BCN-NODAGA. LC-MS analysis confirmed the modular conjugation of the cytotoxic complex and NODAGA chelator to the PD-L1 miniprotein, validating the applicability of the proposed method for the preparation of theranostic agents. Cell viability studies with the PD-L1 miniprotein containing the clicked-Gold-N_3 complex demonstrated that the modified protein maintained an IC_{50} of 0.35 µM in A20 cells and 0.33 µM in MC38 cells. These values are comparable to the cytotoxicity of the original complex (0.78 µM in A20 and 0.35 µM in MC38), suggesting that the modified protein retains the original biological activity of the unconjugated metallodrug. The NODAGA-conjugated PD-L1 miniprotein was effectively radiolabeled with ^{67}Ga, achieving a high radiochemical yield of 95% using low concentrations of the protein and mild conditions (30 µM, 30 min reaction at 37 °C in 0.1 M sodium acetate pH 5). Cell uptake studies showed a significant uptake (~10% uptake/mg of protein after 3 h at 37 °C) in PD-L1-expressing A20 cells. However, further studies are required to determine if this uptake is receptor-mediated. Biodistribution studies in mice inoculated with the A20 cancer cell line revealed a high tumor accumulation of the ^{67}Ga-miniprotein (2.71 ± 0.64 Injected Activity/ g of tissue, 4h p.i.). However, some uptake in non-target organs was also observed such as in the liver (29.79 ± 1.28 I.A./g), blood (7.49 ± 2.18 I.A./g), lungs (4.17 ± 0.67 I.A./g), and spleen (5.12 ± 0.26 I.A./g) at 4h p.i.. Further biodistribution studies at later time points are needed to determine if tumor-to-organ ratios improve with excretion of the probe. Similarly, an ADC was synthesized using a maleimide PEG DBCO linker, enabling the attachment of the Gold cytotoxic payload with a pendant N_3 group for subsequent conjugation to a DBCO-Cy5 fluorophore. IVIS imaging of the fluorescently labeled ADC revealed a clear visualization of A20 tumors, with the fluorescence signal increasing over time, indicating a gradual accumulation of the antibody in the tumor. The ADC was successfully radiolabeled with ^{67}Ga using the BCN-NODAGA chelator conjugated to the "N_3 Gold complex" on the antibody. Radiochemical yields reached 65% after 1 hour incubation at 37 °C with 1.5 µM of the modified antibody. Extending the incubation time to 37 °C did not lead to improved radiochemical yields. Further studies to improve the

radiolabelling yields were limited by difficulties in isolating the NODAGA-conjugated antibody in higher concentration.

In summary, the modular approach herein developed using click chemistry and bioorthogonal reagents for the preparation of protein-metal drugs was shown effective for the design of theranostic agents. The successful applications in radiolabelling and fluorescence imaging demonstrate their potential in both therapeutic and diagnostic contexts. Although the chemistry presented is robust for small proteins, further optimization is necessary for larger molecules, such as antibodies, due to challenges related with precipitation and/or aggregation of larger proteins.

5

FUTURE PERSPECTIVES

Although the current results reveal some challenges in characterizing the final metalloconjugates, there are some potential avenues for future research to overcome these issues and improve the efficacy of the proposed approach for preparing gold-based theranostic agents. One of the problems faced was the characterization of the gold conjugates using ESI-MS with single quadrupole. Although conjugation was evident due to the consumption of the starting proteins and the appearance of new peaks with molecular weight corresponding to the added reactive groups, detecting these conjugates in the ESI-MS spectrum was sometimes difficult, most likely due to their reduced ionization under the MS conditions used. For example, while there is no doubt about the modification of the PD-L1 miniprotein with the gold complex, the same does not extend to the reaction with the antibody. Indeed, after conjugating the gold complex, the modified heavy chain was not detectable. Future efforts will focus on the characterization of the antibody reactions using high-resolution ESI-Quadrupole Time-of-Flight (QTOF) mass spectrometry. Additionally, we plan to quantify the metal content per mg of protein using Inductively Coupled Plasma (ICP) techniques. To prevent protein precipitation during the modification of the antibody, we aim to optimize the reaction conditions to conjugate fewer gold complexes to the antibody, ensuring the stability of its structure is maintained. The synthesis of new gold complexes that are less lipophilic by re-placing the hydrocarbon-N_3 tail with a PEG-N_3 linker is also planned. To confirm the specificity of the radiolabeled proteins, future studies will also involve studies across a broader range of cancer cell lines and human cells with different levels of PD-L1 expression to determine if cytotoxicity, binding or tumor accumulation is linked to presence of the receptor.

Overall, studies aim to refine the design and functionality of these theranostic agents for improved *in vivo* behavior in both diagnostic and therapeutic applications.

REFERENCES

[1] Siegel, R. L.; Giaquinto, A. N.; Jemal, A. Cancer statistics, 2024. CA: A Cancer Journal for Clinicians **2024**, 74(1), 12–49. DOI: https://doi.org/10.3322/caac.21820

[2] Shareef, U.; Altaf, A.; Ahmed, M.; et al., Nagshabandi, M. K. A comprehensive review of discovery and development of drugs discovered from 2020–2022. Saudi Pharmaceutical Journal **2024**, 32(1), 101913. DOI: https://doi.org/10.1016/j.jsps.2023.101913.

[3] DeVita, V. T., Jr.; Chu, E. A history of cancer chemotherapy. Cancer Research **2008**, 68(21), 8643-8653. DOI: 10.1158/0008-5472.CAN-07-6611.

[4] Debela, D. A.-O.; Muzazu, S. G.; Heraro, K. D.; et al., Manyazewal, T. A.-O. New approaches and procedures for cancer treatment: Current perspectives. SAGE Open Medicine **2021**, 9, 20503121211034366. DOI: 10.1177/20503121211034366.

[5] Anand, U.; Dey, A.; Chandel, A. K. S.; et al., Chaudhary, A. Cancer chemotherapy and beyond: Current status, drug candidates, associated risks and progress in targeted therapeutics. Genes & Diseases **2023**, 10(4), 1367-1401. DOI: https://doi.org/10.1016/j.gendis.2022.02.007.

[6] Zhong, L.; Li, Y.; Xiong, L.; et al., Wang, T. Small molecules in targeted cancer therapy: advances, challenges, and future perspectives. Signal transduction and Targeted Therapy **2021**, 6(1), 201. DOI: 10.1038/s41392-021-00572-w.

[7] Joshi, D. C.; Sharma, A.; Prasad, S.; et al., Gupta, M. Novel therapeutic agents in clinical trials: emerging approaches in cancer therapy. Discover Oncology **2024**, 15(1), 342. DOI: 10.1007/s12672-024-01195-7.

[8] Lee, Y. T.; Tan, Y. J.; Oon, C. E. Molecular targeted therapy: Treating cancer with specificity. European Journal of Pharmacology **2018**, 834, 188-196. DOI: https://doi.org/10.1016/j.ejphar.2018.07.034.

[9] Pucci, C.; Martinelli, C.; Ciofani, G. Innovative approaches for cancer treatment: Current perspectives and new challenges. Ecancermedicalscience **2019**, 13, 961. DOI: 10.3332/ecancer.2019.961.

[10] Liu, B.; Zhou, H.; Tan, L.; et. al., Guan, X.-Y. B. Exploring treatment options in cancer: Tumor treatment strategies. Signal Transduction and Targeted Therapy **2024**, 9(1), 175. DOI: 10.1038/s41392-024-01856-7.

[11] Hoyt, E. A.; Cal, P. M. S. D.; Oliveira, B. L.; Bernardes, G. J. L. Contemporary approaches to site-selective protein modification. Nature Reviews Chemistry **2019**, 3(3), 147-171. DOI: 10.1038/s41570-019-0079-1.

[12] Boutureira, O.; Bernardes, G. J. L. Advances in chemical protein modification. Chemical Reviews **2015**, 115(5), 113-128. DOI: 10.1021/cr500399p.

[13] Jevševar, S.; Kunstelj, M.; Porekar, V. G. PEGylation of therapeutic proteins. Biotechnology Journal **2010**, 5(1), 113–128. DOI: https://doi.org/10.1002/biot.200900218.

[14] Chudasama, V.; Maruani, A.; Caddick, S. Recent advances in the construction of antibody-drug conjugates. Nature Chemistry **2016**, 8(2), 114-119. DOI: 10.1038/nchem.2415.

[15] Rowe, S. P.; Pomper, M. A.-O. Molecular imaging in oncology: Current impact and future directions. CA: A Cancer Journal for Clinicians **2022**, 72(4), 333–352. DOI: 10.3322/caac.21713.

[16] Kumar, M.; Reddy, N. C.; Rai, V. Chemical technologies for precise protein bioconjugation interfacing biology and medicine. Chemical Communications **2021**, 57(58), 7083–7095. DOI: 10.1039/d1cc02268g.

[17] Lang, K.; Chin, J. W. Cellular incorporation of unnatural amino acids and bioorthogonal Labeling of Proteins. Chemical Reviews **2014**, 114(9), 4764-4806. DOI: 10.1021/cr400355w.

[18] Bloom, S.; Liu, C.; Kölmel, D. K.; et al., MacMillan, D. W. C. Decarboxylative alkylation for site-selective bioconjugation of native proteins via oxidation potentials. Nature Chemistry **2018**, 10(2), 205–211. DOI: 10.1038/nchem.2888.

[19] Chen, L.; Xin, X.; Zhang, Y.; et al., Xu, Z. Advances in Biosynthesis of Non-Canonical Amino Acids (ncAAs) and the Methods of ncAAs Incorporation into Proteins. Molecules **2023**, 28(18), 6745. DOI: 10.3390/molecules28186745.

[20] Matos, M. J.; Oliveira, B. L.; Martínez-Sáez, N.; et al., Deery, M. J. Chemo- and Regioselective Lysine Modification on Native Proteins. Journal of the American Chemical Society **2018**, 140(11), 4004–4017. DOI: 10.1021/jacs.7b12874.

[21] Ravasco, J. M. J. M.; Faustino, H.; Trindade, A.; Gois, P. M. P. Bioconjugation with Maleimides: A Useful Tool for Chemical Biology. Chemistry - A European Journal **2019**, 25(1), 43-59. DOI: 10.1002/chem.201803174.

[22] Ohri, R.; Bhakta, S.; Fourie-O'Donohue, A.; et al., Bos, A. B. High-Throughput Cysteine Scanning to Identify Stable Antibody Conjugation Sites for Maleimide- and Disulfide-Based Linkers. Bioconjugate Chemistry **2018**, 29(2), 473–485. DOI: 10.1021/acs.bioconjchem.7b00791.

[23] Christie, R. J.; Fleming, R.; Bezabeh, B.; et al., Wu, H. Stabilization of cysteine-linked antibody drug conjugates with N-aryl maleimides. Journal of Controlled Release **2015**, 220, 660–670. DOI: 10.1016/j.jconrel.2015.09.032.

[24] Shen, B.-Q.; Xu, K.; Liu, L.; et al., Mai, E. Conjugation site modulates the in vivo stability and therapeutic activity of antibody-drug conjugates. Nature Biotechnology **2012**, 30(2), 184–189. DOI: 10.1038/nbt.2108.

[25] Vasco, A. V.; Taylor, R. J.; Méndez, Y.; Bernardes, G. J. L. On-Demand Thio-Succinimide Hydrolysis for the Assembly of Stable Protein-Protein Conjugates. Journal of the American Chemical Society **2024**, 146(30), 20709–20719. DOI: 10.1021/jacs.4c03721.

[26] Tong, J. T. W.; Harris, P. W. R.; Brimble, M. A.; Kavianinia, I. An insight into FDA approved antibody-drug conjugates for cancer therapy. Molecules **2021**, 26(19), 5847 DOI: 10.3390/molecules26195847.

[27] Chen, F.-J.; Gao, J. Fast Cysteine Bioconjugation Chemistry. Chemistry - A European Journal **2022**, 28(66), e202201843. DOI: 10.1002/chem.202201843.

[28] Bernardim, B.; Cal, P. M. S. D.; Matos, M. J.; et al., Jiménez-Osés, G. Stoichiometric and irreversible cysteine-selective protein modification using carbonylacrylic reagents, Nature Communications **2016**, 7(1), 13128. DOI: 10.1038/ncomms13128.

[29] Silva, M. J. S. A.; Faustino, H.; Coelho, J. A. S.; et al., Gois, P. M. P. Efficient Amino-Sulfhydryl Stapling on Peptides and Proteins Using Bifunctional NHS-Activated Acrylamides. Angewandte Chemie International Edition **2021**, 60(19), 10850–10857. DOI: 10.1002/anie.202016936.

[30] Djaló, M.; Silva, M. J. S. A.; Faustino, H.; et al., Gois, P. M. P. Multivalent NHS-activated acrylates for orthogonal site-selective functionalisation of peptides at cysteine residues. Chemical Communications **2022**, 58(57), 7928–7931, DOI: 10.1039/d2cc02204d.

[31] Huang, R.; Li, Z.; Sheng, Y.; et al., Jiang, B. N-Methyl- N-phenylvinylsulfonamides for Cysteine-Selective Conjugation. Organic Letters **2018**, 20(20), 6526–6529. DOI: 10.1021/acs.orglett.8b02849.

[32] Devaraj, N. K. The Future of Bioorthogonal Chemistry. ACS Central Science **2018**, 4(8), 952–959. DOI: 10.1021/acscentsci.8b00251.

[33] Bird, R. E.; Lemmel, S. A.; Yu, X.; Zhou, Q. A. Bioorthogonal Chemistry and Its Applications. Bioconjugate Chemistry **2021**, 32(12), 2457-2479. DOI: 10.1021/acs.bioconjchem.1c00461.

[34] Hang, H. C.; Yu, C.; Kato, D. L.; Bertozzi, C. R. A metabolic labeling approach toward proteomic analysis of mucin-type O-linked glycosylation. Proceedings of the National Academy of Sciences **2003**, 100(25), 14846. DOI: 10.1073/pnas.2335201100.

[35] Sletten, E. M.; Bertozzi, C. R. Bioorthogonal chemistry: Fishing for selectivity in a sea of functionality. Angew Chem Int Ed Engl **2009**, 48(38), 6974-6998. DOI: 10.1002/anie.200900942.

[36] Kolb, H. C.; Finn, M. G.; Sharpless, K. B. Click Chemistry: Diverse Chemical Function from a Few Good Reactions. Angewandte Chemie International Edition **2001**, 40(11), 2004-2021. DOI: 10.1002/1521-3773(20010601)40:11<2004::AID-ANIE2004>3.0.CO;2-5.

[37] Oliveira, B. L.; Guo, Z.; Bernardes, G. J. L. Inverse electron demand Diels-Alder reactions in chemical biology. Chem Soc Rev **2017**, 46(16), 4895-4950. DOI: 10.1039/c7cs00184c.

[38] Rostovtsev, V. V.; Green, L. G.; Fokin, V. V.; Sharpless, K. B. A Stepwise Huisgen Cycloaddition Process: Copper(I)-Catalyzed Regioselective "Ligation" of Azides and Terminal Alkynes. Angewandte Chemie International Edition **2002**, 41(14), 2596-2599. DOI: 10.1002/1521-3773(20020715)41:14<2596::AID-ANIE2596>3.0.CO;2-4.

[39] Tornøe, C. W.; Christensen, C.; Meldal, M. Peptidotriazoles on solid phase: [1,2,3]-Triazoles by regiospecific copper(I)-catalyzed 1,3-dipolar cycloadditions of terminal alkynes to azides. The Journal of Organic Chemistry **2002**, 67(9), 3057–3064. DOI: 10.1021/jo011148j.

[40] Agard, N. J.; Prescher, J. A.; Bertozzi, C. R. A strain-promoted [3 + 2] azide-alkyne cycloaddition for covalent modification of biomolecules in living systems. Journal of the American Chemical Society **2004**, 126(46), 15046–15047. DOI: 10.1021/ja044996f.

[41] Kim, E.; Koo, H. Biomedical applications of copper-free click chemistry: In vitro, in vivo, and ex vivo. Chem Sci **2019**, 10(34), 7835–7851. DOI: 10.1039/c9sc03368h.

[42] Luu, T.; Gristwood, K.; Knight, J. C.; Jörg, M. Click Chemistry: Reaction Rates and Their Suitability for Biomedical Applications. Bioconjugate Chemistry **2024**, 35(6), 715-731. DOI: 10.1021/acs.bioconjchem.4c00084.

[43] Blackman, M. L.; Royzen, M.; Fox, J. M. Tetrazine ligation: Fast bioconjugation based on inverse-electron-demand Diels-Alder reactivity. J Am Chem Soc **2008**, 130(41), 13518–13519. DOI: 10.1021/ja8053805.

[44] Ehrlich, P. Collected Studies on Immunity. J. Wiley & Sons **1906**.

[45] Fu, Z.; Li, S.; Han, S.; et al., Zhang, Y. Antibody drug conjugate: the "biological missile" for targeted cancer therapy. Signal Transduction and Targeted Therapy **2022**, 7(1), 93. DOI: 10.1038/s41392-022-00947-7.

[46] Wu, M.; Huang, W.; Yang, N.; Liu, Y. Learn from antibody–drug conjugates: consideration in the future construction of peptide-drug conjugates for cancer therapy. Exp Hematol Oncol **2022**, 11(1), 93. DOI: 10.1186/s40164-022-00347-1.

[47] Adepu, S.; Ramakrishna, S. Controlled drug delivery systems: Current status and future directions. Molecules **2021**, 26(19), 5905. DOI: 10.3390/molecules26195905.

[48] Wang, M.; Liu, J.; Xia, M.; et al., Cheng, Y. Peptide-drug conjugates: A new paradigm for targeted cancer therapy. European Journal of Medicinal chemistry **2024**, 265, 116119. DOI: 10.1016/j.ejmech.2023.116119.

[49] Baah, S.; Laws, M.; Rahman, K. M. Antibody–drug conjugates—a tutorial review. Molecules **2021**, 26(10), 2943. DOI: 10.3390/molecules26102943.

[50] Lu, J.; Jiang, F.; Lu, A.; Zhang, G. Linkers having a crucial role in antibody–drug conjugates. Int J Mol Sci **2016**, 17(4), 561. DOI: 10.3390/ijms17040561.

[51] Tsuchikama, K.; Anami, Y.; Ha, S. Y. Y.; Yamazaki, C. M. Exploring the next generation of antibody–drug conjugates. Nature Reviews Clinical Oncology **2024**, 21(3), 203-223. DOI: 10.1038/s41571-023-00850-2.

[52] Conilh, L.; Sadilkova, L.; Viricel, W.; Dumontet, C. Payload diversification: a key step in the development of antibody–drug conjugates, Journal of Hematology & Oncology **2023**, 16(1), 3. DOI: 10.1186/s13045-022-01397-y.

[53] Abdolmaleki, S.; Aliabadi, A.; Khaksar, S. Riding the metal wave: A review of the latest developments in metal-based anticancer agents. Coordination Chemistry Reviews **2024**, 501, 215579. DOI: 10.1016/j.ccr.2023.215579.

[54] De Almeida, A.; Oliveira, B. L.; Correia, J. D. G.; et al., Casini, A. Emerging protein targets for metal-based pharmaceutical agents: An update. Coordination Chemistry Reviews **2013**, 257(19-20), 2689-2704. DOI: 10.1016/j.ccr.2013.01.031.

[55] Anthony, E. J.; Bolitho, E. M.; Bridgewater, H. E.; et al., Palau, M. Metallodrugs are unique: Opportunities and challenges of discovery and development. Chem Sci **2020**, 11(48), 12888–12917. DOI: 10.1039/d0sc04082g.

[56] Dörr, M.; Meggers, E. Metal complexes as structural templates for targeting proteins. Current Opinion In Chemical Biology **2014**, 19, 76-81. DOI: 10.1016/j.cbpa.2014.01.005.

[57] Zhang, C.; Xu, C.; Gao, X.; Yao, Q. Platinum-based drugs for cancer therapy and anti-tumor strategies. Theranostics **2022**, 12(5), 2115-2132. DOI: 10.7150/thno.69424.

[58] Esteban-Fernández, D.; Cañas, B.; Pizarro, I.; et al., Gómez-Gómez, M. M. SEC-ICP-MS and ESI-MS as tools to study the interaction between cisplatin and cytosolic biomolecules. Journal of Analitical Atomic Spectrometry **2007**, 22(9), 1113–1121, DOI: 10.1039/b706251f.

[59] Shahlaei, M.; Asl, S. M.; Derakhshani, A.; et al., Saboury, A. Platinum-based drugs in cancer treatment: Expanding horizons and overcoming resistance. Journal of Molecular Structure **2024**, 1301, 137366. DOI: 10.1016/j.molstruc.2023.137366.

[60] Nardon, C.; Boscutti, G.; Fregona, D. Beyond Platinums: Gold Complexes as Anticancer Agents. Anticancer Res **2014**, 34(1), 487-492.

[61] Paprocka, R.; Wiese-Szadkowska, M.; Janciauskiene, S.; et al., Helmin-Basa, A. Latest developments in metal complexes as anticancer agents. Coordination Chemistry Reviews **2022**, 452, 214307. DOI: 10.1016/j.ccr.2021.214307.

[62] Ndagi, U.; Mhlongo, N.; Soliman, M. E. Metal complexes in cancer therapy – An update from drug design perspective. Drug design, development and therapy **2017**, 11, 599-616. DOI: 10.2147/DDDT.S119488.

[63] Lu, Y. A.-O.; Ma, X.; Chang, X.; et al., Liu, W. A.-O. X. Recent development of gold(i) and gold(iii) complexes as therapeutic agents for cancer diseases. Chemical Society Reviews **2022**, 51, 5518. DOI: 10.1039/d1cs00933h.

[64] Porchia, M.; Pellei, M.; Marinelli, M.; et al., Santini, C. New insights in Au-NHCs complexes as anticancer agents. European Journal of Medicinal Chemistry **2018**, 146, 709-746. DOI: 10.1016/j.ejmech.2018.01.065.

[65] Moreno-Alcántar, G.; Picchetti, P.; Casini, A. Gold Complexes in Anticancer Therapy: From New Design Principles to Particle-Based Delivery Systems. Angewandte Chemie International Edition **2023**, 62(22), e202218000. DOI: 10.1002/anie.202218000.

[66] Casini, A.; Pöthig, A. Metals in Cancer Research: Beyond Platinum Metallodrugs. American Chemical Society **2024**, 10(2), 242-250. DOI: 10.1021/acscentsci.3c01340.

[67] Mora, M. A.-O.; Gimeno, M. A.-O.; Visbal, R. A.-O. Recent advances in gold-NHC complexes with biological properties. Chemical Society Reviews **2019**, 48(2), 447-462. DOI: 10.1039/c8cs00570b.

[68] Rieb, J. A.-O.; Dominelli, B.; Mayer, D.; et al., Kühn, F. A.-O. X. Influence of wing-tip substituents and reaction conditions on the structure, properties and cytotoxicity of Ag(i)-and Au(i)-bis(NHC) complexes. Dalton Transactions **2017**, 46(8), 2722–2735. DOI: 10.1039/c6dt04559f.

[69] Zou, T.; Lok, C. N.; Wan, P. K.; et al., Che, C. M. Anticancer metal-N-heterocyclic carbene complexes of gold, platinum and palladium. Elsevier Ltd **2018**, 43, 30-36. DOI: 10.1016/j.cbpa.2017.10.014.

[70] Baker, M. V.; Barnard Pj Fau - Berners-Price, S. J.; Berners-Price Sj Fau - Brayshaw, S. K.; et al., White, A. H. Cationic, linear Au(I) N-heterocyclic carbene complexes: Synthesis, structure

and anti-mitochondrial activity. Dalton Transactions **2006**, 30, 3708–3715. DOI: 10.1039/b602560a.

[71] Diehl, T.; Krause, M. T. S.; Ueberlein, S.; et al., Engeser, M. Synthesis of hydroxyl-functionalized N-heterocyclic carbene gold(i) complexes and peptide conjugates. Dalton Transactions **2017**, 46(9), 2988–2997. DOI: 10.1039/c6dt04834j.

[72] Niu, W.; Chen, X.; Tan, W.; Veige, A. S. N-Heterocyclic Carbene–Gold(I) Complexes Conjugated to a Leukemia-Specific DNA Aptamer for Targeted Drug Delivery. Angewandte Chemie - International Edition **2016**, 55(31), 8889–8893. DOI: 10.1002/anie.201602702.

[73] Hospital, A.; Gibard, C.; Gaulier, C.; et al., Gautier, A. Access to functionalised silver(I) and gold(I) N-heterocyclic carbenes by [2 + 3] dipolar cycloadditions. Dalton Transactions **2012**, 41(22), 6803–6812. DOI: 10.1039/c2dt30249g.

[74] Sen, S.; Perrin, M. W.; Sedgwick, A. C.; et al., Arambula, J. F. Covalent and non-covalent albumin binding of Au(i) bis-NHCs via post-synthetic amide modification. Chemical Science **2021**, 12(21), 7547–7553. DOI: 10.1039/d1sc01055g.

[75] Richter, L. F.; Marques, F.; Correia, J. D. G.; et al., Kühn, F. E. Exploiting click-chemistry: backbone post-functionalisation of homoleptic gold(i) 1,2,3-triazole-5-ylidene complexes. Dalton Transactions **2023**, 52(46), 17185–17192. DOI: 10.1039/d3dt03052k.

[76] Sheyi, R.; de la Torre, B. A.-O.; Albericio, F. A.-O. Linkers: An Assurance for Controlled Delivery of Antibody-Drug Conjugate. Pharmaceutics **2022**, 14(2), 396. DOI: 10.3390/pharmaceutics14020396.

[77] Matos, M. J.; Labão-Almeida, C.; Sayers, C.; et al., Bernardes, G. J. L. Synthesis and Biological Evaluation of Homogeneous Thiol-Linked NHC*-Au-Albumin and -Trastuzumab Bioconjugates. Chemistry - A European Journal **2018**, 24(47), 12250–12253. DOI: 10.1002/chem.201800872.

[78] Ahad, A.; H, K. S.; Del Solar, V.; et al., Contel, M. Shifting the Antibody-Drug Conjugate Paradigm: A Trastuzumab-Gold-Based Conjugate Demonstrates High Efficacy against Human Epidermal Growth Factor Receptor 2-Positive Breast Cancer Mouse Model. ACS Pharmacol Transl Sci **2023**, 6(12), 1972–1986. DOI: 10.1021/acsptsci.3c00270.

[79] Kalimuthu, K.; Lubin, B.-C.; Bazylevich, A.; et al., Firer, M. A. Gold nanoparticles stabilize peptide-drug-conjugates for sustained targeted drug delivery to cancer cells. Journal of Nanobiotechnology **2018**, 16(1), 34. DOI: 10.1186/s12951-018-0362-1.

[80] Bailey, D. L.; Humm, J. L.; Todd-Pokropek, A.; Van Aswegen, A. Nuclear Medicine Physics: A Handbook for Teachers and Students. International Atomic Energy Agency, **2015**.

[81] Massoud, T. F.; Gambhir, S. S. Molecular imaging in living subjects: Seeing fundamental biological processes in a new light. Genes & Development **2003**, 17(5), 545-580. DOI: 10.1101/gad.1047403.

[82] Rong, J.; Haider, A.; Jeppesen, T. E.; Josephson, L.; Liang, S. H. Radiochemistry for positron emission tomography. Nature Communications **2023**, 14(1), 3257. DOI: 10.1038/s41467-023-36377-4.

[83] Tolmachev, V.; Vorobyeva, A. Radionuclides in Diagnostics and Therapy of Malignant Tumors: New Development. Cancers (Basel) **2022**, 14(2), 297. DOI: 10.3390/cancers14020297.

[84] Kostelnik, T. I.; Orvig, C. Radioactive Main Group and Rare Earth Metals for Imaging and Therapy. Chemical Reviews **2019**, 119(2), 902-956. DOI: 10.1021/acs.chemrev.8b00294.

[85] Pimlott, S. L.; Sutherland, A. Molecular tracers for the PET and SPECT imaging of disease. Chemical Society Reviews **2011**, 40(1), 149-162. DOI: 10.1039/b922628c.

[86] Kassis, A. I.; Adelstein, S. J. Radiobiologic principles in radionuclide therapy. Journal of Nuclear Medicine **2005**, 46 (Suppl 1), 4S-12S.

[87] Boschi, A.; Uccelli, L.; Marvelli, L.; et al., Martini, P. Technetium-99m Radiopharmaceuticals for Ideal Myocardial Perfusion Imaging: Lost and Found Opportunities. Molecules **2022**, 27(4), 1188. DOI: 10.3390/molecules27041188.

[88] Henrich, U.; Kopka, K. Lutathera®: The first FDA-and EMA-approved radiopharmaceutical for peptide receptor radionuclide therapy. Pharmaceuticals (Basel) **2019**, 12(3), 114. DOI: 10.3390/ph12030114.

[89] Dhoundiyal, S.; Srivastava, S.; Kumar, S.; et al., Taghizadeh-Hesary, F. Radiopharmaceuticals: navigating the frontier of precision medicine and therapeutic innovation. European Journal of Medical Research **2024**, 29(1), 26. DOI: 10.1186/s40001-023-01627-0.

[90] Kręcisz, P.; Czarnecka, K.; Królicki, L.; et al., Szymański, P. Radiolabeled Peptides and Antibodies in Medicine. Bioconjug Chem **2021**, 32(1), 25-42. DOI: 10.1021/acs.bioconjchem.0c00617.

[91] Price, E. W.; Orvig, C. Matching chelators to radiometals for radiopharmaceuticals. Chemical Society Reviews **2014**, 43(1), 260-290. DOI: 10.1039/c3cs60304k.

[92] Saha, G. B. Radionuclide Generators. Fundamentals of Nuclear Pharmacy. Springer International Publishing **2018**, 77-92.

[93] Rinne, S. S.; Dahlsson Leitao, C.; Gentry, J.; et al., Orlova, A. Increase in negative charge of 68Ga/chelator complex reduces unspecific hepatic uptake but does not improve imaging properties of HER3-targeting affibody molecules. Scientific Reports **2019**, 9(1), 17710. DOI: 10.1038/s41598-019-54149-3.

[94] Meyer, J.-P.; Adumeau, P.; Lewis, J. S.; Zeglis, B. M. Click Chemistry and Radiochemistry: The First 10 Years. Bioconjugate Chemistry **2016**, 27(12), 2791-2807. DOI: 10.1021/acs.bioconjchem.6b00561.

[95] Sachin, K.; Jadhav, V. H.; Kim, E.-M.; et al., Kim, D. W. F-18 labeling protocol of peptides based on chemically orthogonal strain-promoted cycloaddition under physiologically friendly reaction conditions. Bioconjugate Chemistry **2012**, 23(8), 1680–1686. DOI: 10.1021/bc3002425.

[96] Moek, K. L.; Giesen, D.; Kok, I. C.; et al., de Vries, E. G. E. Theranostics using antibodies antibody-related therapeutics, J Nucl Med **2017**, 58 (Suppl 2), 83S-90S. DOI: 10.2967/jnumed.116.186940.

[97] Bodei, L.; Herrmann, K.; Schöder, H.; et al., Lewis, J. S. Radiotheranostics in oncology: current challenges and emerging opportunities. Nat Rev Clin Oncol **2022**, 19(8), 534-550. DOI: 10.1038/s41571-022-00652-y.

[98] Li, M. H.; Lo, S. N.; Chen, M. W.; et al., Chang, C. H. Molecular Imaging for Radiolabeling a PSMA-Targeted Long Circulating Peptide as a Theranostic Agent in Mice Bearing a Human Prostate Tumor. Journal of Medical Biological Engineering **2021**, 41(3), 360–368. DOI: 10.1007/s40846-021-00611-5.

[99] Srivastava, S. C. Paving the way to personalized medicine: Production of some promising theragnostic radionuclides at Brookhaven national laboratory. Semin Nucl Med Elsevier Inc **2012**, 42, 151-163. DOI: 10.1053/j.semnuclmed.2011.12.004.

[100] Han, Y.; Liu, D.; Li, L. PD-1/PD-L1 pathway: current researches in cancer. Am J Cancer Res. **2020**. 10(3), 727-742.

[101] Chow, S. Y.; Unciti-Broceta, A. Targeted Molecular Construct for Bioorthogonal Theranostics of PD-L1-Expressing Cancer Cells. JACS Au **2022**, 2(7), 1747–1756. DOI: 10.1021/jacsau.2c00328.

[102] Xiao, D.; Luo, L.; Li, J.; et al., Zhou, X. Development of bifunctional anti-PD-L1 antibody MMAE conjugate with cytotoxicity and immunostimulation. Bioorg Chem **2021**, 116, 105366. DOI: 10.1016/j.bioorg.2021.105366.

[103] Markham, A. Atezolizumab: First Global Approval. Drugs **2016**, 76(12), 1227–1232. DOI: 10.1007/s40265-016-0618-8.

[104] Kim, E. S. Avelumab: First Global Approval. Drugs **2017**, 77(8), 929–937. DOI: 10.1007/s40265-017-0749-6.

[105] Syed, Y. Y. Durvalumab: First Global Approval. Drugs **2017**, 77(12), 1369–1376. DOI: 10.1007/s40265-017-0782-5.

[106] Lee, H. A.-O.; Lee, S. H.; Heo, Y. A.-O. Molecular interactions of antibody drugs targeting PD-1, PD-L1, and CTLA-4 in immuno-oncology. Molecules **2019**, 24(6), 1190. DOI: 10.3390/molecules24061190.

[107] Chigoho, D. M.; Lecocq, Q.; Awad, R. M.; et al., Bridoux, J. Site-specific radiolabeling of a human pd-l1 nanobody via maleimide–cysteine chemistry. Pharmaceuticals (Basel) **2021**, 14(6), 550. DOI: 10.3390/ph14060550.

[108] Posner, Z.; Yannuzzi, I.; Prensner, J. R. Shining a light on the dark proteome: Non-canonical open reading frames and their encoded miniproteins as a new frontier in cancer biology. Protein Sci **2023**, 23(8), e4708. DOI: 10.1002/pro.4708.

[109] Stumpp, M. T.; Binz, H. K.; Amstutz, P. DARPins: A new generation of protein therapeutics. Drug Discov Today **2008**, 13(15-16), 695-701. DOI: 10.1016/j.drudis.2008.04.013.

[110] Crook, Z. R.; Nairn, N. W.; Olson, J. M. Miniproteins as a Powerful Modality in Drug Development. Trends Biochem Sci **2020**, 45(4), 332-346. DOI: 10.1016/j.tibs.2019.12.008.

[111] Quijabo-Rubio, A.; Ulge, U. Y.; Walkey, C. D.; Silva, D. A. The advent of de novo proteins for cancer immunotherapy. Current opinion In Chemical Biology **2020**. DOI: 10.1016/j.cbpa.2020.02.002.

[112] Silva, D. A.; Yu, S.; Ulge, U. Y.; et al., Baker, D. De novo design of potent and selective mimics of IL-2 and IL-15. Nature **2019**, 565(7738), 186–191. DOI: 10.1038/s41586-018-0830-7.

[113] Fda, & cder. HIGHLIGHTS OF PRESCRIBING INFORMATION **2018**. www.fda.gov/medwatch.

[114] Gil-Gil, M. J.; Mesia, C.; Rey, M.; Bruna, J. Bevacizumab for the Treatment of Glioblastoma. Clin Med Insights Oncol **2013**, 7, 123-35. DOI: 10.4137/CMO.S8503.

[115] Phetpjoung, T.; Malla, A.; Rattanapisit, K.; et al., Phoolcharoen, W. Expression of plant-produced anti-PD-L1 antibody with anoikis sensitizing activity in human lung cancer cells via., suppression on epithelial-mesenchymal transition. PLoS One **2022**, 17(11), e0274737. DOI: 10.1371/journal.pone.0274737.

[116] Sau, S.; Petrovici, A.; Alsaab, H. O.; Iyer, A. K. PDL-1 antibody drug conjugate for selective Chemo-guided immune modulation of cancer. Cancers (Basel) **2019**, 11(2). DOI: 10.3390/cancers11020232.

[117] Ibraheem, F. Q.; Maraie, N. K.; Al-Sudani, B. T.; Raauf, A. M. R. Prospective effect of linkers type on the anticancer activity of pemetrexed-monoclonal antibody (atezolizumab) conjugates. F1000Res **2024**, 12, 1197. DOI: 10.12688/f1000research.140284.1.

[118] Ščasnár, V.; van Lier, J. E. The use of SEP-PAK Sl cartridges for the preparation of gallium chloride from the citrate solution. Eur J Nucl Med **1993**, 20(3), 273–273. DOI: 10.1007/BF00170012.

[119] Mant, C.T.; Chen, Y.; Yan, Z.; et al., Hodges, R.S. HPLC analysis and purification of peptides. Methods Mol Biol **2007**, 386, 3-55. DOI: 10.1007/978-1-59745-430-8_1.

[120] D´Addio, S. M.; Bothe, J.R.; Neri, C.; et al., Templeton, A. C. New and Evolving Techniques for the Characterization of Peptide Therapeutics. J Pharm Sci **2016**, 105(10), 2989–3006. DOI: 10.1016/j.xphs.2016.06.011.

[121] LookOut ® Mycoplasma PCR Detection Kit. (n.d.). www.sigmaaldrich.com

[122] Cell Titer-Blue™ Cell Viability Assay Automated Protocol. (n.d.). Promega

[123] Raftery, M. J.; Determination of oxidative protein modifications using mass spectrometry. Redox Rep **2014**, 19(4), 140-7. DOI: 10.1179/1351000214y.0000000089.

[124] Rolland, A. D.; Prell, J. S. Approaches to Heterogeneity in Native Mass Spectrometry. Chem Rev **2022**, 122(8), 7909-7951. DOI: 10.1021/acs.chemrev.1c00696.

[125] Ezan, E.; Dubois, M.; Becher, F. Bioanalysis of recombinant proteins and antibodies by mass spectrometry. Analyst **2009**, 134(5), 825-34. DOI: 10.1039/b819706g.

[126] Zou, J.; Xia, H.; Zhang, C.; et al., Bi, F. Casp8 acts through A20 to inhibit PD-L1 expression: The mechanism and its implication in immunotherapy. Cancer Sci **2021**, 112(7), 2664–2678. DOI: 10.1111/cas.14932.

[127] Yu, L.; Wu, X.; Cheng, Z.; et al., Ferrare, N. Interaction between bevacizumab and murine VEGF-A: A reassessment. Invest Ophthalmol Vis Sci **2008**, 49(2), 522–527. DOI: 10.1167/iovs.07-1175.

A

Supplementary Material

As mentioned in Chapter 3, studies conducted with Atezolizumab were also performed with Bevacizumab (Beva) to optimize the reaction conditions. The detailed results and optimizations using Beva are explained in this chapter.

A.1 Bevacizumab

Bevacizumab (MVASI®, Amgen Inc.), a high-affinity human IgG1 monoclonal antibody was generously provided by Rita Fior´s laboratory at the Champalimaud Foundation. This antibody targets the Vascular Endothelial Growth Factor (VEGF), inhibiting angiogenesis by preventing VEGF from binding to its receptors on the surface of endothelial cells. In contrast to Atezolizumab that targets tumor receptors, bevacizumab targets the ligand the VEGF receptor.

The commercial formulation of Bevacizumab contains 25 mg/mL of antibody in a 50 mM sodium phosphate buffer at pH 6.2. The formulation also includes 60 mg/mL α, α-trehalose dihydrate and 0.4 mg/mL polysorbate 20. Bevacizumab has a molecular weight of 149.238 g/mol.

The antibody is produced using recombinant DNA technology in a CHO mammalian cell expression system [114], [115].

A.2 Synthesis of an ADC

A.2.1 Reduction of disulfide bridges´ reaction

As discussed in Section 3.4.2, reacting the antibody with TCEP is crucial for ensuring proper modification. To determine the best reaction conditions for TCEP, the antibody was treated under various temperatures and molar equivalents. The effectiveness of these conditions was confirmed by LC-MS. The data highlights the optimal conditions for TCEP treatment, ensuring efficient antibody modification while balancing the impact on subsequent reactions.

First, the reaction with TCEP was conducted at 25 °C and 37 °C to determine the optimal temperature for reduction. It was observed that at 25 °C, the antibody was not detected by ESI-MS analysis, whereas at 37 °C, the antibody detectable (**Figure 56 – A and B**). Before increasing the temperature, an additional study was performed to evaluate whether increasing the TCEP equivalents or the temperature would be more effective. Despite using 100 equivalents of TCEP at 25 ºC, antibody reduction occurred as HC was observed in the MS spectrum, but intensity of HC was low (20%).

Therefore, it was concluded that TCEP reduction should be carried out at 37 °C. At this temperature, the reduction is more effective, allowing for the thiols to be adequately free for the subsequent reactions.

A

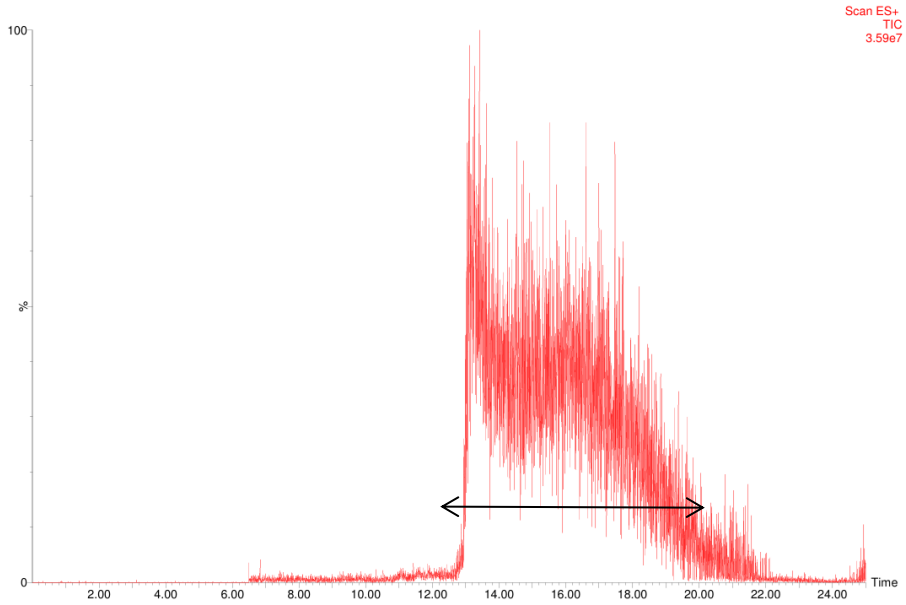

B

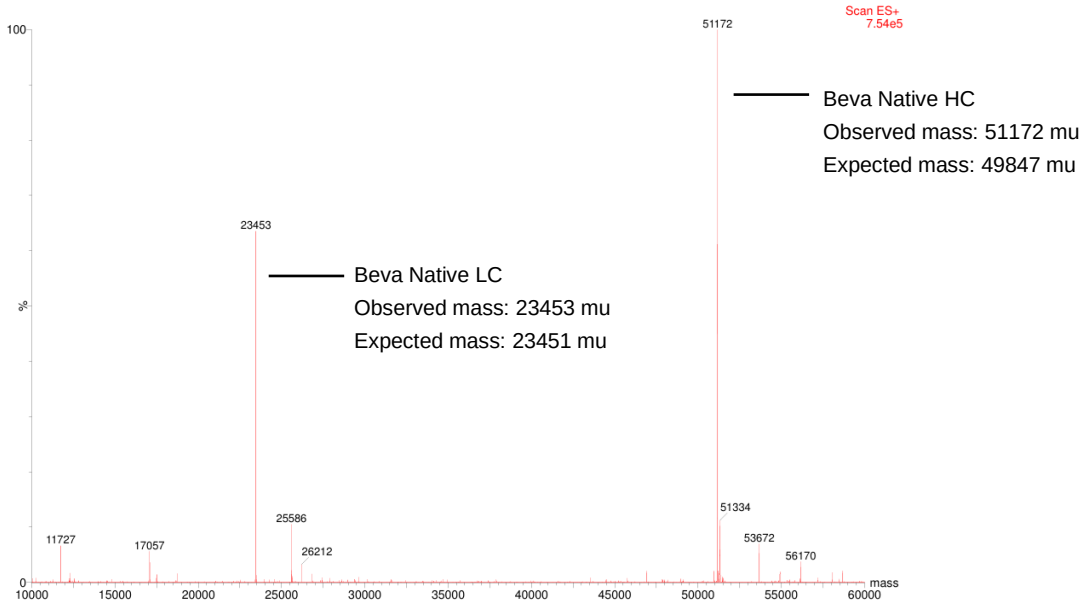

Figure 56 – ESI-MS analysis of the native antibody. A – Total ion ESI LC-MS chromatogram of the native antibody; B – Deconvoluted mass spectrum of the peak shown in A; Main peaks represent the expected molecular weight of the LC and HC, respectively of the native antibody. Sequence of Bevacizumab available at https://go.drugbank.com/drugs/DB00112 (accessed on 13-10-24)

TCEP was removed by washing the antibody with a zeba column before proceeding with the conjugation, as TCEP can react with the maleimide under certain conditions and reduce the efficiency of

the reaction. However, this step compromises the mass yield of the reduced antibody, as will be discussed in section A.2.2.

A.2.2 Conjugation with Maleimide DBCO

For the conjugation of the maleimide to the antibody several conditions were optimized, including the need to remove TCEP before the reaction, adjusting the stoichiometry, and determining the appropriate equivalents of the reagent to achieve complete conjugation.

To confirm that the modification was achieved, the antibody in its native state was characterized and compared with the conjugates form.

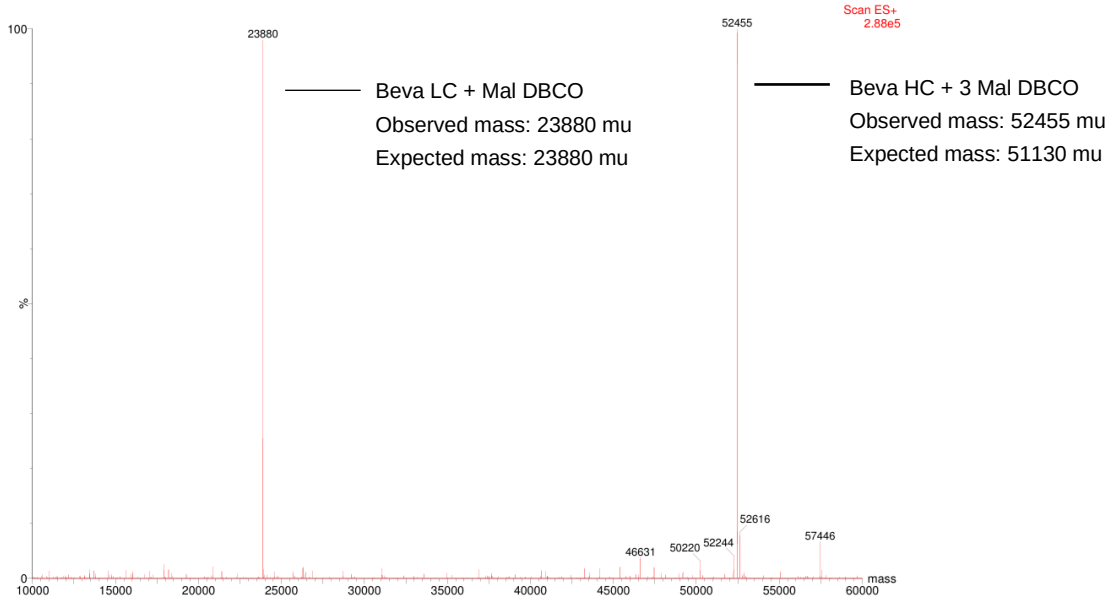

Figure 57 – Analysis of the conjugation of Mal DBCO to the antibody. A – Total ion ESI LC-MS chromatogram of the antibody conjugated with Mal DBCO; B – Deconvoluted mass spectrum of the peak shown in A; Main peaks represent the expected molecular weight of the LC and HC of the antibody conjugated to Mal DBCO (23453 Da of the LC + 427.5 Da from Mal DBCO; 51172 Da of the HC + 427.5 x 3 Da from conjugations of three Mal DBCO groups).

A comparison of the molecular weight of the native protein (**Figure 56 – B**) with the molecular weight of conjugated antibody (**Figure 57 – B**), reveals that the observed and expected masses of the LC and HC are in accordance, confirming that the conjugation was effective with complete reaction with Mal DBCO. In the deconvoluted mass spectrum of the conjugated antibody, no peaks corresponding to the molecular weight of the native antibody are observed (23453 Da for the light chain and 51172 Da for the heavy chain), demonstrating that all the native antibody was successfully modified. Importantly, the heavy chain of the modified antibody shows the presence of three Mal DBCO molecules. Despite using an excess of reagent sometimes greater than 20 equivalents, only three disulfide bridges were consistently modified on the heavy chain. The modified antibody was subsequently purified through dialysis, and its concentration was determined using the Qubit method, as described in section 2.4. Starting from

a concentration of 6.0 mg/mL of native miniprotein (200 µLs), the conjugated antibody with the DBCO handle was obtained with a concentration of 1.7 mg/mL (210 µLs) after purification.

Table 9 presents the conjugation yields obtained for different tested stoichiometries, as well as the effects of removing TCEP with a Zeba column. The results show that complete conjugation with Mal-DBCO is achieved using 20 equivalents of the reagent and a 2h reaction time at room temperature. However, further quantification of the conjugated antibody was performed (following the protocol described in section 2.4.3.2), using both 10 and 20 equivalents at room temperature and at 37 ºC to determine the conditions that minimized antibody loss, as shown in **Table 10**.

The use of Zeba columns to remove unreacted reagents was also investigated by quantifying the native and conjugated antibodies before and after Zeba column treatment. As previously observed with excipient removal, the Zeba column led to a very significative in antibody concentration.

Table 9 – Optimization of antibody conjugation with Mal-DBCO. The optimal conditions for antibody conjugation with Mal-DBCO at a temperature of 25 ºC, with a reaction time of 2 h. Under these conditions, a high modification rate (90-100%) was obtained.

Antibody concentration (uM)	**Equivalents of Mal-DBCO**	**Reaction time (h)**	**Temperature (ºC)**	**LC modification (%)**	**HC modification**		**Zeba column**
					%	**Nº**	
40	10	2	25	-	-	-	Yes
	10		37	0	56	1	
	10		25	100	80	3	No
	10		37	100	77	3	
	20		25	72	100	3	Yes
	20		37	-	-	-	
	20		25	100	100	3	No
	20		37	100	77	3	
	30		25	100	100	3	Yes
	30		37	100	100	3	
	30		25	-	-	-	No
	30		37	-	-	-	

Table 10 – Quantification of the conjugated antibody reacted under different conditions

Equivalents	**10 eqs Mal DBCO**		**20 eqs Mal DBCO**	
Temperature (ºC)	25	37	25	37
Initial concentration (mg/mL)	5.9			
Initial concentration (μM)	40			
Concentration after reaction (mg/mL)	1.67	1.04	1.75	0.852
Concentration after reaction (μM)	22.4	13.9	23.4	11.4
Protein loss	2.14	3.44	2.05	4.20

Based on the results obtained, the optimal conditions for antibody conjugation with Mal DBCO are 20 equivalents of the reagent, reacting for 2h at room temperature without using a zeba column. This approach provides the highest yield and minimizes protein loss.

The purification technique used was dialysis because it achieved a better yield of the reactions when used this method compared with Amicon.

A.2.3 Conjugation with gold complex

After successful modification with Mal DBCO, the antibody was conjugated with a gold complex.

Several conditions were optimized for the gold complex conjugation i.e. determination of appropriate reagent equivalents to achieve complete conjugation. Initially, an excess of reagent was used due to the presence of two azides in the complex, which helped prevent dimerization. However, when the reaction was tested with 72 equivalents of the reagent, the HC was not visible in the LC-MS analysis. Instead, the LC-MS analysis revealed an abundant peak corresponding to a fragment of the gold complex with 429 g/mol, likely generated due to the temperature used during the LC-MS analysis. The LC analysis also showed a modification of approximately 20%, indicating that some conjugating occurred, but not at the desired level (**Figure 58**).

Subsequent testing with 40 equivalents of the reagent showed an improvement in the yield of the LC modification, with the fragment peak disappearing from the LC-MS analysis. This result suggests that 40 equivalents provided a more effective balance between complete conjugation and minimizing undesired side reactions (**Figure 59**).

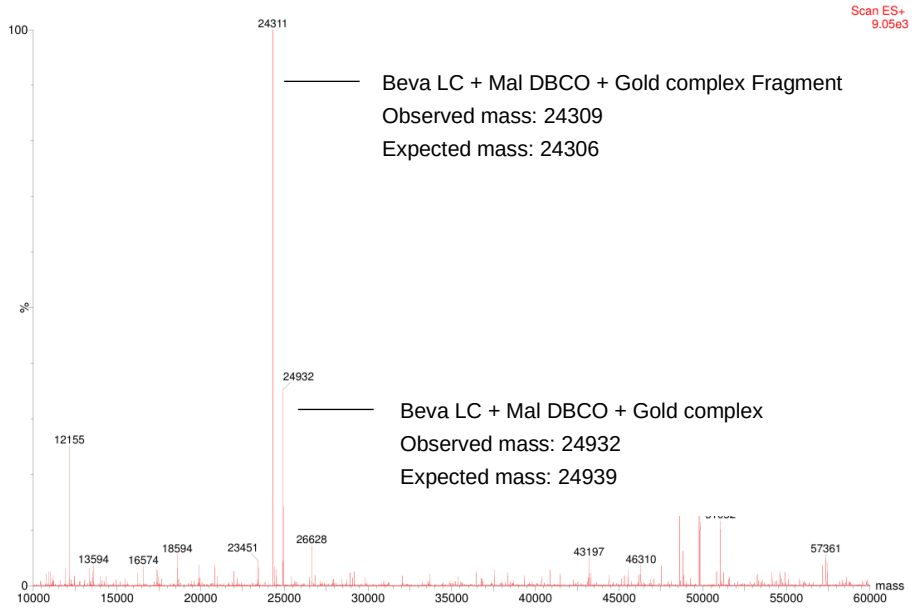

Figure 58 – ESI-MS analysis of the antibody conjugated with 72 equivalents of N_3-Gold complex. Deconvoluted mass spectrum showing conjugation of the N_3-Gold complex to the LC of "Beva DBCO" (23880 Da from Beva DBCO + 1059 Da from N_3-Gold complex). The main peak at 24311 mass units (+429 Da than Atezo Mal DBCO) was attributed to the formation of a fragment of the gold complex, likely resulting from the conditions used during the LC-MS analysis. Modification of the HC of "Beva DBCO" with the N_3-Gold complex was not observed in the ESI-MS spectrum (51130 Da from Beva DBCO + 1059 x 3 Da from N_3-Gold complex = 54306 Da).

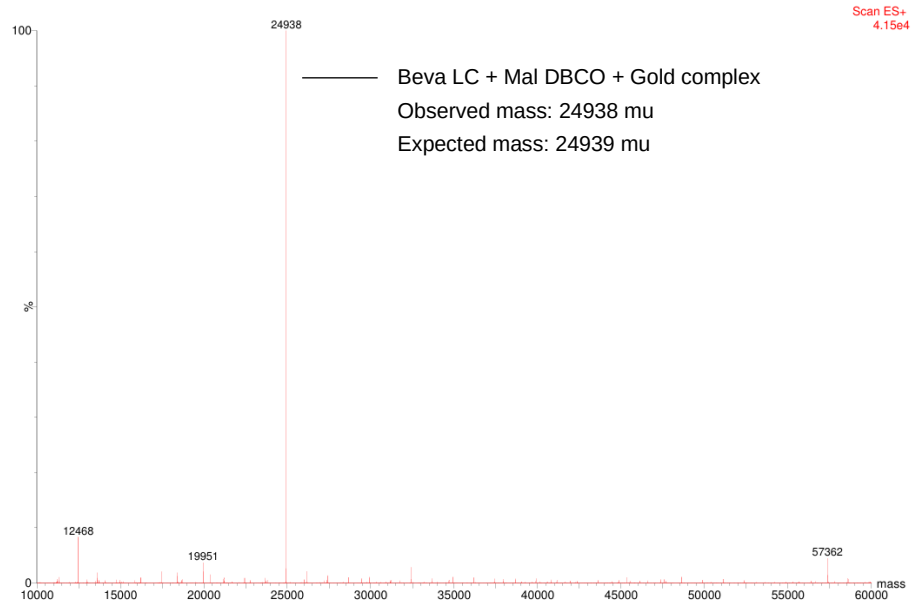

Figure 59 – ESI-MS analysis of the conjugate Beva DBCO Gold formed using 40 equivalents of N_3-Gold complex. Deconvoluted mass spectrum showing conjugation of the N_3-Gold complex to the LC of "Beva DBCO" (24880 Da from Beva DBCO + 1059 Da

from N_3-Gold complex). Modification of the HC of "Beva DBCO" with the N_3-Gold complex was not observed in the ESI-MS spectrum (51130 Da from Beva DBCO + 1059 x 3 Da from N_3-Gold complex = 54306 Da).

Overall, after reaction with 40 equivalents of the N_3-Gold complex, the light chain was fully converted as shown in **Figure 59**. However, detection of the heavy chain modified with the Gold complex (expected mass: 55630 Da), or either the modified heavy chain with DBCO (52453 Da for Beva DBCO) or the native heavy chain (51172 Da) was not observed in the ESI-MS spectrum. This could be related to the low ionization efficiency of the heavy chain after reacting with the gold complex, or potentially due to precipitation of the reacted heavy chain. The antibody modified with the N_3-Gold complex was purified, and its concentration was determined using the Qubit method, as described in section 2.4. Starting from a concentration of 1.7 mg/mL of the conjugated antibody with the DBCO handle (210 µLs), the conjugated antibody with the N_3-Gold complex was obtained with a concentration of 0.53 mg/mL (150 µLs) after purification.

A.2.4 Improve hydrophilicity of Bevacizumab

To improve the concentration of the reaction, as Atezolizumab, a PEG linker was also used. To confirm that the modification was complete using the standard conditions previously described (20 equivalents, 2 h reaction at room temperature) the native antibody (**Figure 56 – B**) was compared with the modified version (**Figure 60**).

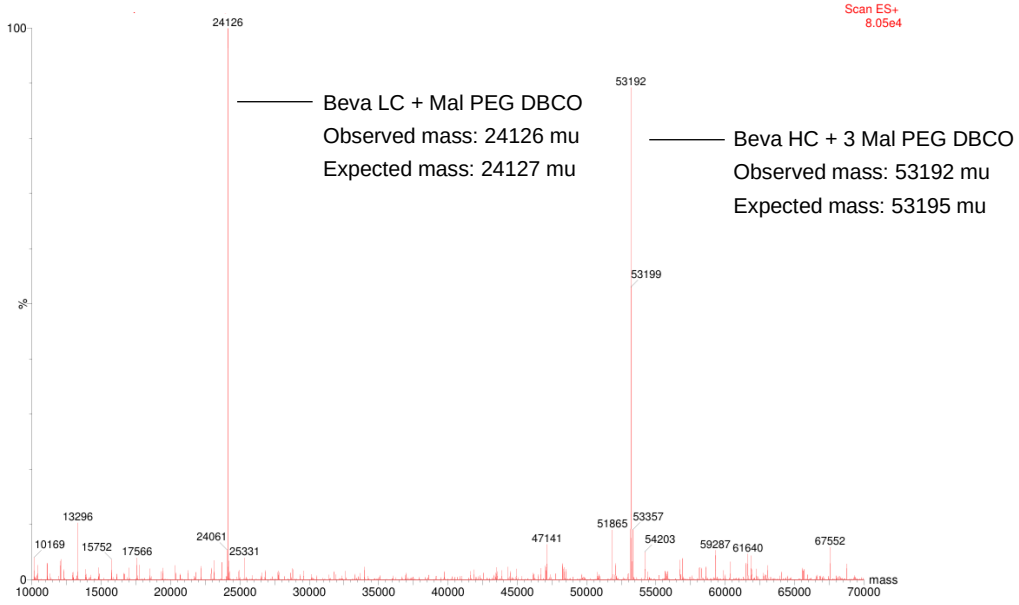

Figure 60 – ESI-MS analysis of the conjugate Beva Mal PEG DBCO. Main peaks represent the molecular weight of the LC and HC of the antibody conjugated to Mal PEG DBCO (23453 Da of the LC + 674,7 Da from Mal PEG DBCO; 51172 Da of the HC + 674,7 x 3 Da from conjugations of three Mal PEG DBCO groups).

The mass spectrum (**Figure 60 – B**) shows peaks corresponding to the antibody conjugated with Mal-PEG-DBCO. Of note, the HC was modified with three Mal PEG DBCO molecules, consistent with the results from the Mal DBCO reaction. The absence of peaks corresponding to the native antibody (23453 Da for the LC and 51172 Da for the HC) confirms that the reaction was completed.

The concentration of the antibody was determined by Qubit using the same protocol described for the miniprotein. Importantly, the concentration of the antibody conjugated with the PEG linker increased significantly, reaching 20 µM. This suggests that enhancing the hydrophilicity of the modified antibody improves the reaction yield to 50% by mass, doubling the yield observed for the Mal DBCO conjugate without the PEG linker. These results were thoroughly validated through triplicate experiments.

A.2.5 Conjugation of the Gold complex to Beva modified with Mal PEG DBCO

After switching to a more hydrophilic linker, the conjugation reactions used 20 equivalents of the gold complex as seen for Atezolizumab. LC-MS analysis confirmed that both conditions resulted in the modification to the LC of the antibody. The absence of peaks corresponding to intermediates, or the native antibody suggests that modification was both efficient and completed (**Figure 61**).

Compared to the results obtained with the Mal-DBCO linker, the hydrophilic linker significantly improved the solubility of the final product as assessed by determination of the mass yields by Qubit (Section 2.4). Starting from a concentration of 2.35 mg/mL (125 µLs) of the conjugated antibody with the maleimide PEG DBCO, the conjugated antibody with the N_3 Gold complex was obtained with a concentration of 0.7 mg/mL (180 µLs) after purification. However, the reaction of the heavy chain bearing the PEG DBCO group (53194 Da) with the gold complex (expected mass: 56371 Da) was not observed in the ESI-MS spectrum (**Figure 61**). This could be related with the low ionization efficiency of the heavy chain after reacting with the gold complex, or potentially due to precipitation of the reacted heavy chain, although this is unlikely.

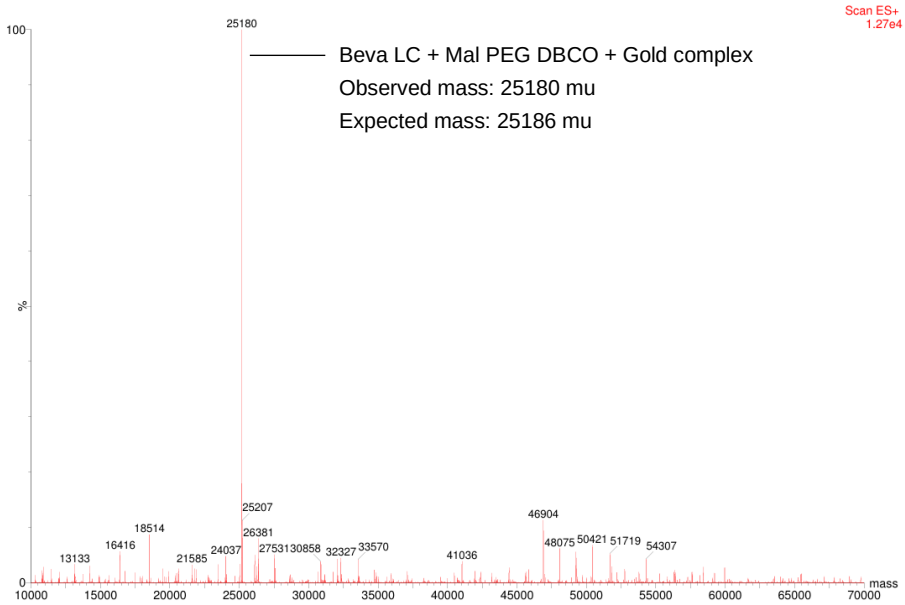

Figure 61 – ESI-MS analysis of the conjugation of the N_3-Gold complex to Beva PEG DBCO. Deconvoluted mass spectrum showing conjugation of the N_3-Gold complex to the LC of "Beva PEG DBCO" (24126 Da from Beva PEG DBCO + 1059 Da from N_3-Gold complex). Modification of the HC of "Beva PEG DBCO" with the N_3-Gold complex was not observed in the ESI-MS spectrum (53195 Da from Beva DBCO + 1059 x 3 Da from N_3-Gold complex = 56371 Da).

A.3 Radiolabeling of Beva PEG DBCO Gold

A.3.1 Conjugation with BCN-NODAGA chelator

To prepare the antibody for radiolabeling the BCN-NODAGA chelator was conjugated to the antibody for subsequent stabilization of the radioactive metal ^{67}Ga (**Figure 62**).

The reaction was carried out using 20 equivalents of the chelator at 25 ºC for 1 – 2h. It is important to note that this reaction was made with the Mal DBCO linker and wasn´t repeated with the Mal PEG DBCO. LC-MS analysis clearly showed that the starting protein was reacted i.e. Beva DBCO Gold (24939 Da) with a formation of a peak with 25531 Da (expected mass: 25532 Da) corresponding to the modification of the light chain with the NODAGA chelator (**Figure 62**). As previously observed and discussed, modification of the heavy chain of "Beva DBCO Gold" with the chelator was not observed in the ESI-MS spectrum. Purification and quantification of the concentration (0.63 mg/mL, volume 200 µLs) was followed the standard protocol.

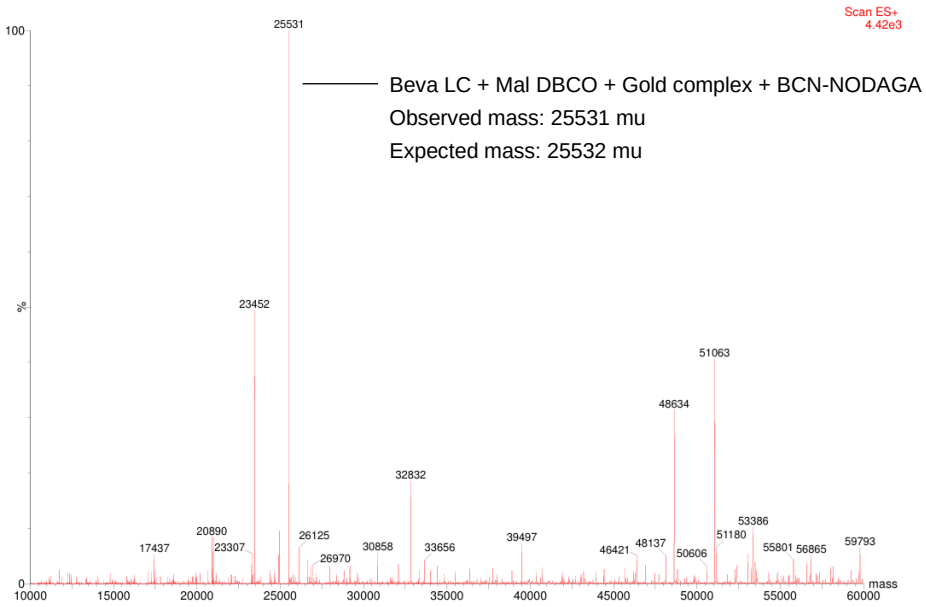

Figure 62 – ESI-MS analysis of the conjugation of BCN-NODAGA to Beva DBCO Gold. Deconvoluted mass spectrum showing conjugation of the chelator to the LC of "Beva DBCO Gold" (24939 Da from Beva DBCO Gold + 593 Da from N_3-Gold complex). The main peak at 23452 mass units was attributed to the native antibody. Modification of the HC of "Beva PEG DBCO Gold" with the chelator was not observed in the ESI-MS spectrum (54306 Da from Atezo PEG DBCO Gold + 593 x 3 Da from BCN-NODAGA = 56085 Da).

A.3.2 Labeling with gallium-67

The radiolabeling conditions for the antibody are presented in section 2.4.6. In detail, the Beva PEG DBCO Gold NODAGA conjugate (4 µM in PBS buffer, pH 6.2) was incubated with [^{67}Ga]$GaCl_3$ (in a 1:1 ratio, 20 µCi in acetate buffer pH 5.0) for 3h at 45 °C, resulting in a final concentration of 2 µM and a total volume of 40 µL. Radiolabeling yields were assessed using iTLC, as shown in **Figure 63**. Similar to the miniprotein, the labeled antibody remained at the origin, while free [^{67}Ga]$GaCl_3$ migrated in the solvent front, as expected. The highest radiochemical yield for the NODAGA-conjugated antibody was 100% after 3h at 45 °C and purification with zeba column. As a control, the same protocol was applied to label the native Bevacizumab antibody without being conjugated to NODAGA. iTLC analysis showed no significant labelling of the antibody with ^{67}Ga, which indicates that the radiometal was bound to Beva through NODAGA chelation.

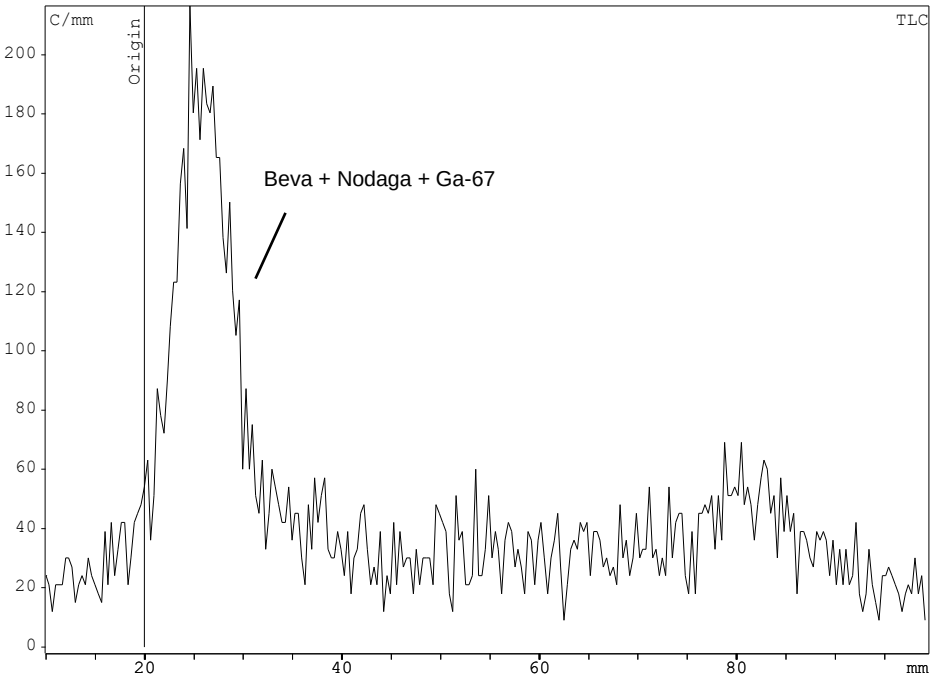

Figure 63 – iTLC-SG radiochromatogram for the radiolabeling of the NODAGA-conjugated bevacizumab with [^{67}Ga]$GaCl_3$ during 3h at 45 ºC at a final concentration of 2 μM.

A.4 Fluorescent labeling of Bevacizumab

A.4.1 Conjugation with DBCO Cy5

To enable fluorescence-based detection and imaging, the antibody was conjugated with the fluorescent dye DBCO Cy5. Conjugation of the fluorophore to the antibody Beva PEG DBCO Gold was analyzed by SDS-PAGE in-gel fluorescence.

A.4.2 In-gel Fluorescence imaging

To confirm that the antibody was fluorescent, an SDS-PAGE gel was run, followed by standard procedures for detecting the full antibody and its light and heavy chains. Fluorescence imaging was performed using an Amersham imaging system (**Figure 64**) together with Coomassie Blue staining for visible dye detection (**Figure 65**).

For the SDS-PAGE analysis, negative controls were included: well A contained the native (unmodified) antibody, while well B contained the native antibody subjected to the same reaction conditions as the conjugated antibody, but without the addition of the DBCO and gold complex. Well C contained the antibody modified with the maleimide PEG DBCO, gold complex and fluorophore dye. In-gel fluorescence imaging shows the presence of fluorescent bands corresponding to the LC, HC and full IgG as detected by SDS-PAGE that is consistent with the incorporation of Cy5 fluorophore in the antibody (**Figure 64**).

In the Coomassie Blue-stained gel (**Figure 65**), distinct bands were observed: at 25 kDa, corresponding to the LC, and at 60 kDa, corresponding to the HC. The top band at 150 kDa is assigned to

the full IgG molecule; however, we cannot rule out the possibility of a dimeric IgG, which requires further confirmation.

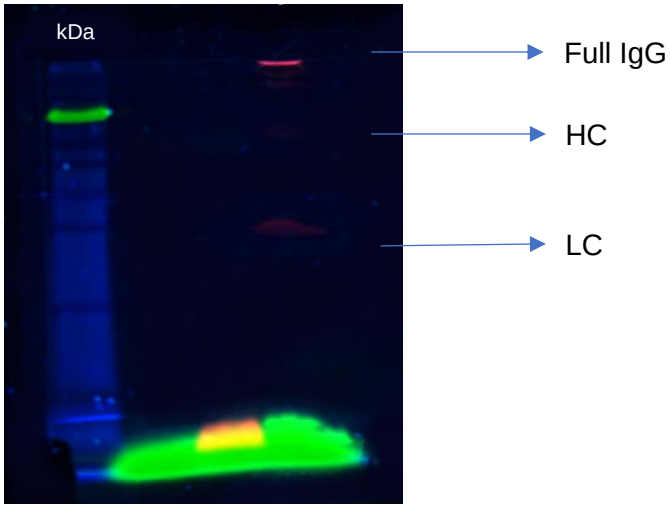

Figure 64 – The Amersham Image. The well A, B and C contain the same as the dye coomassie blue

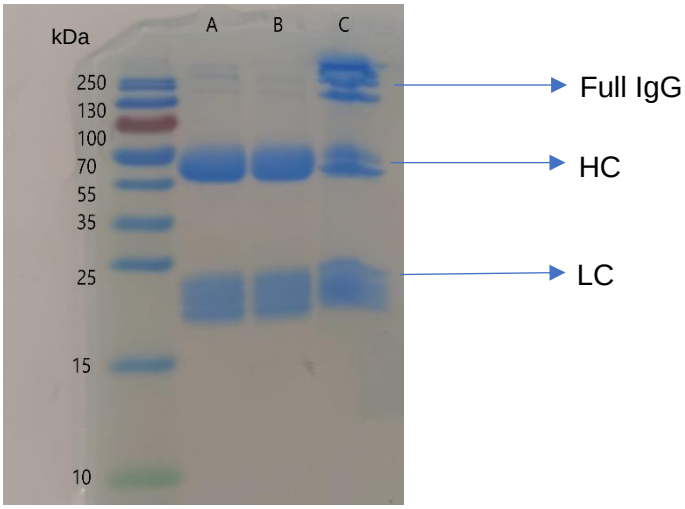

Figure 65 – The visible dye coomassie blue. Well A - native antibody; well B - Native antibody + fluorophore; Well C - Antibody modified with maleimide PEG DBCO, gold complex and fluorophore. Details can be found in section 2.7.2

A.4.3 *In vivo* imaging

After confirming the fluorescence of the antibody, we proceeded to *in vivo* studies using mice inoculated with the 4T1 tumor cell line, known for its overexpression of VEGF [127]. The aim was to determine whether the fluorescently labeled antibody accumulates in the tumor tissue.

In vivo fluorescence imaging was performed at four time points post-injection (1, 6, 24, and 48 h) after injection of ~18 nM/kg of probe, like the method used for Atezolizumab. During each imaging session, the mice were analysed for 15 seconds to capture the fluorescence signal. The **Figure 66** demonstrate that the accumulation of the labeled antibody in the tumor was highest at 48 h post-injection, with a significant fluorescence signal detected in all imaged animals injected with the probe (Mouse Green, Mouse Red and Mouse No colour) compared to the control.

The color scale used in the imaging ranged from brown to yellow, with values from $5{,}0 \times 10^{-5}$ to $2{,}0 \times 10^{-4}$ fluorescent units. The fluorescence signal showed a steady increase over time, indicating a gradual accumulation of the antibody within the tumor. This is consistent with the slow excretion and extended blood half-life of antibodies, which can range from 6 to 28 days *in vivo*. The control mouse, injected with the vehicle (PBS), displayed no autofluorescence in the tumor region across all time points, as seen in **Figure 66**.

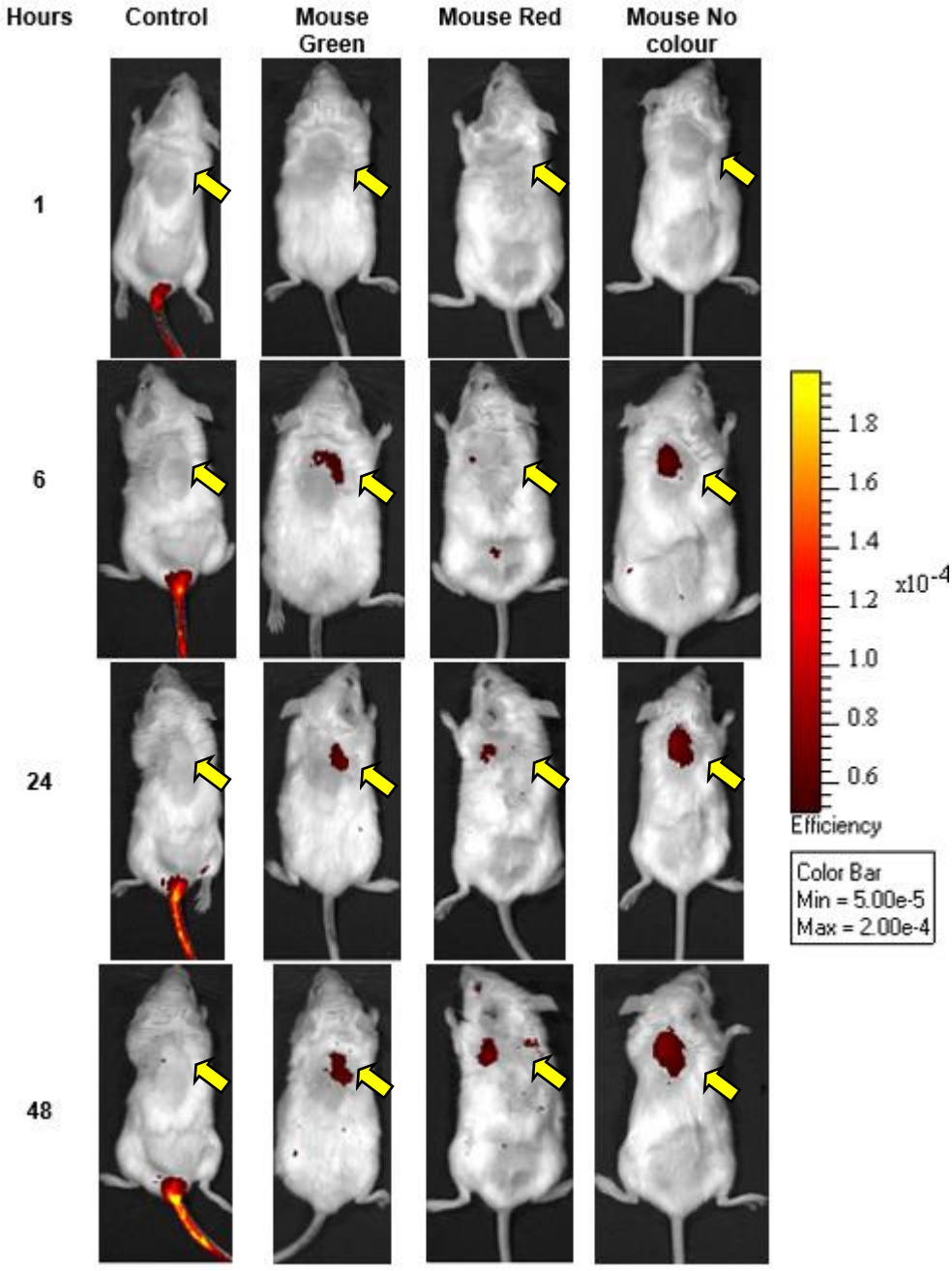

Figure 66 – Non-invasive *in vivo* imaging of Bevacizumab labeled with Cy5 in mice with 4T1 tumors (overexpressing VEGF). Fluorescence images were taken at 1, 6, 24, and 48 h post-injection (18 nM/kg). The color scale on the right indicates fluorescence intensity from brown (lowest) to yellow (highest), with values from 5.0×10^{-5} to 2.0×10^{-4}. Tumor location are marked with arrows.

The control mouse (injected with PBS) showed no fluorescence, confirming the specific accumulation of Bevacizumab in the tumor tissue.